Design of Experiment for Increased Fidelity Aeroelastic Testing

Master Thesis Report

Dharmil Baxi

Delft University of Technology

TU Delft

Design of Experiment for Increased Fidelity Aeroelastic Testing

by

Dharmil Baxi

Student Number: 5561868
Supervisor: J. Sodja
Study Duration: February 2024 - July 2025
Faculty: Faculty of Aerospace Engineering, Delft

Cover: Canadarm 2 Robotic Arm Grapples SpaceX Dragon by NASA under CC BY-NC 2.0 (Modified)
Style: TU Delft Report Style, with modifications by Daan Zwaneveld

TU Delft

Acknowledgments

This document marks the culmination of a remarkable journey undertaken during my Master's thesis from February 2024 to July 2025 at Delft University of Technology as part of the Aerospace Engineering Master's program. It is with profound gratitude and appreciation that I reflect on the experiences and learning opportunities provided to me during this period.

I sincerely thank my thesis supervisor, Jurij Sodja, for his invaluable guidance, expertise, patience, and encouragement throughout this research. His mentorship has been instrumental in helping me navigate complex topics and develop a deeper understanding of the subject.

My heartfelt thanks also go to Roderick Schildkamp for his support and constructive feedback during the literature study phase, which significantly contributed to the direction and quality of my work. I would also like to thank Mirthe Oude Alink from the internship coordination team at TU Delft for helping me navigate internship-related matters. I am further grateful to Bianca Giovanardi for her guidance and support in working with the cluster computing facilities.

I want to acknowledge Hrishika for her encouragement and support. Her simple companionship helped me persevere through the challenging stages of this journey. I am also grateful to my friends for their unwavering support; their belief in me has been a constant source of motivation. Most importantly, I owe my deepest gratitude to my family. My parents and sister have been pillars of strength, whose patience, love, and constant concern have carried me through the most challenging stages of this work. Their support has been truly immeasurable, and this achievement is as much theirs as it is mine.

Finally, I would like to thank Delft University of Technology for offering this opportunity and providing access to the necessary academic and research facilities.

This thesis represents the academic work completed over the past year and a personal learning, growth, and self-discovery journey. I look forward to building upon the foundation laid during this experience as I continue toward my professional aspirations.

Thank you all for being an integral part of this journey.

Dharmil Baxi
Delft, August 2025

Executive Summary

Accurately predicting gust loads on flexible, high-aspect-ratio aircraft remains a central challenge in aeroelastic analysis. Traditional approaches, such as linear aerodynamic solvers and simplified structural models, have long been used for gust load estimation. While effective for conventional configurations, these methods become unreliable for highly flexible aircraft, where large deformations and nonlinear aeroelastic interactions dominate. More recent methods, such as time-domain simulations coupling unsteady vortex lattice or CFD-based aerodynamics with advanced structural solvers, address these challenges but remain computationally demanding for routine design and testing.

Wind tunnel experiments play an essential role in aeroelastic validation. However, clamped models do not represent free-flight conditions and often overestimate structural loads. Recent studies have explored hybrid frameworks where numerically simulated free-flight responses are prescribed to wind tunnel models to improve realism. These proof-of-concept tests demonstrated feasibility but relied on idealized configurations that are not directly transferable to practical wind tunnel environments. The objective of this thesis is therefore:

> *To design a flexible aircraft model for wind tunnel free-flight testing, and to develop its equivalent beam representation for increased-fidelity aeroelastic testing.*

A high-aspect-ratio wing was designed with a 0.75 m span, rectangular planform, and simplified structural layout tailored for fabrication and testing in TU Delft's Open Jet Facility. The configuration balances the need for measurable aeroelastic effects with experimental feasibility.

A finite element model of the wing was developed in ANSYS to extract stiffness and inertia properties. Static analyses provided spanwise bending and torsional stiffness, while modal analyses identified natural frequencies and mode shapes. The wing was divided into four bays to capture structural variability, and sectional properties were derived for each. These data formed the basis of an equivalent four-segment beam model.

The initial beam captured overall deformation trends but underestimated bending and torsional responses. Its stiffness values were tuned to align spanwise static deflections with the finite element wing. Mass and inertia properties were distributed across the beam segments, after which modal analyses were performed. Frequency mismatches were resolved by refining rotational inertias, and the Modal Assurance Criterion analysis confirmed a strong correlation between the beam and the finite element model. The validated beam successfully replicates the detailed wing's static and dynamic behavior while increasing computational efficiency. It provides a reliable reduced-order representation suitable for use in aeroelastic simulation frameworks.

In conclusion, this thesis demonstrates that a practical wing configuration can be designed for free-flight testing and reduced to an equivalent beam model that captures its essential structural dynamic properties. This reduced-order model bridges the gap between detailed finite element representations and the requirements of real-time aeroelastic simulations, offering sufficient fidelity for gust response analysis while remaining computationally efficient for use in hybrid wind tunnel experiments.

The immediate next step is to implement this validated beam in SHARPy to perform gust response simulations. This will enable motion profiles derived from numerical simulations to be prescribed to experimental models under realistic conditions, directly supporting the development of increased-fidelity aeroelastic testing methodology.

Contents

Acknowledgments i

Executive Summary ii

List of Figures vii

List of Tables viii

Nomenclature viii

1 Introduction 1
- 1.1 Background . . . 1
- 1.2 Problem Statement . . . 1
- 1.3 Research Objectives . . . 2
- 1.4 Methodology . . . 2

2 Literature Review 4
- 2.1 Gust Modeling in Aeroelastic Analysis . . . 4
  - 2.1.1 Classification of Gusts . . . 4
  - 2.1.2 Discrete Gust Models . . . 5
  - 2.1.3 Continuous Gust Models . . . 6
- 2.2 Aeroelastic Simulation Tools and Modeling Approaches . . . 7
  - 2.2.1 MSC NASTRAN . . . 7
  - 2.2.2 SHARPy . . . 9
  - 2.2.3 CFD-FEM Coupling Tools . . . 11
  - 2.2.4 Other Frameworks . . . 13
  - 2.2.5 Comparative Summary of Frameworks . . . 14
- 2.3 Experimental Methods for Gust Response . . . 15
  - 2.3.1 Experimental Free-Flight Gust Testing . . . 16
  - 2.3.2 Hybrid Simulation Approaches . . . 16
  - 2.3.3 Benchmark Wing and Aircraft Models . . . 18
- 2.4 Research Gap . . . 20

3 Design of a Flexible Aircraft Model for Aeroelastic Testing 21
- 3.1 Model Aircraft Requirements . . . 21
  - 3.1.1 Dimensional Constraints . . . 21
  - 3.1.2 Performance Requirements . . . 22
  - 3.1.3 Modularity . . . 22
- 3.2 Flexible Aircraft Design Considerations . . . 22
  - 3.2.1 Wing . . . 22
  - 3.2.2 Overall Planform . . . 26
  - 3.2.3 Static Stability and Tail sizing . . . 27
  - 3.2.4 Propeller Effects . . . 28
- 3.3 Preliminary Design Parameters . . . 28
  - 3.3.1 Geometric and Stability Parameters . . . 29
  - 3.3.2 Mass Distribution and CG Estimation . . . 30
- 3.4 3D Model Definition . . . 30

4 Structural Modeling 32
- 4.1 Model Simplification . . . 32

4.2 Finite Element Analyses Setup . . . 33
4.2.1 Material parameters . . . 33
4.2.2 Contact Definitions and Boundary Conditions . . . 34
4.2.3 Meshing Strategy . . . 34
4.2.4 Point-Mass Allocation . . . 35
4.2.5 Derivation of Beam-Equivalent Spanwise Responses . . . 36
4.2.6 Modeling Assumptions . . . 36
4.3 Modal Analysis of Wing . . . 37
4.3.1 Modal Response and Shape Visualizations . . . 37
4.4 Global Stiffness Extraction from Linear Static FEM . . . 41
4.4.1 Stiffness Extraction Methodology . . . 41
4.4.2 Load Case Setup . . . 42
4.4.3 Global Stiffness Extraction and Results . . . 44
4.5 Section-Wise Structural Analysis . . . 47
4.5.1 Section Modeling Assumptions . . . 48
4.5.2 Section-wise Linear Static Analysis . . . 48
4.5.3 Boundary Conditions and Remote Point Setup . . . 48
4.6 Equivalent Beam Derivation . . . 53
4.6.1 1D Beam Model Definition and FEM Setup . . . 53
4.6.2 Stiffness Matching . . . 54
4.6.3 Modal Matching . . . 60

5 Conclusion **66**

References **68**

A Appendix A **72**
A.1 PSD Model Comparison Plot . . . 72
A.2 Point Mass Calculations . . . 73
A.3 Node Selection Criteria for Spanwise Deformation Extraction . . . 73
A.4 3D Wing Modal Raw Spanwise Deformation Data . . . 74
A.5 3D Wing Effective Modal Mass Data . . . 89
A.6 1D Beam Effective Modal Mass Data . . . 90
A.7 1D Beam Spanwise Modal Deformation Data . . . 91

List of Figures

1.1 Methodology and the overarching goal . . . 3

2.1 Gust directionality [3] . . . 5
2.2 Classification of gust models . . . 5
2.3 Velocity distributions of discrete gust models . . . 6
2.4 Comparison of Dryden and von Kármán PSDs . . . 7
2.5 Linear aeroelastic workflow using SOL 144 [12] . . . 8
2.6 Quasi-nonlinear aeroelastic coupling in NASTRAN [12] . . . 8
2.7 Iterative nonlinear coupling using NASTRAN modules [12] . . . 9
2.8 SHARPy's modular framework for a nonlinear, time-marching aeroelastic simulation [19] 10
2.9 *elsA* CFD-FEM solver schematic [21] . . . 12
2.10 NeoCASS aeroelastic solver [12] . . . 13
2.11 Variation in aeroelastic quantities vs angle of attack [12] . . . 14
2.12 Framework selection map with solver domain classification . . . 15
2.13 2-DOF aeroelastic model [33] . . . 16
2.14 Increased-fidelity aeroelastic testing approach [2] . . . 17
2.15 Sodja and De Breuker's aircraft model based on modified Gjerek's aeroelastic apparatus [2] . . . 17
2.16 SOLIDWORKS model of the Pazy Wing [35] . . . 18
2.17 QT1 aircraft platform 3-view [28] . . . 19
2.18 NLR 5 DoF free-free aeroelastic model [38] . . . 19

3.1 Schematic of Open Jet Facility [41] . . . 22
3.2 Effect of wing sweep and AR on wing-alone pitch up . . . 25
3.3 Distribution of coefficient of lift along the wing span for various taper ratios . . . 26
3.4 Aircraft in level flight [51] . . . 28
3.5 Schematic overview of the scaled model aircraft . . . 29
3.6 Detailed views of the 3D wing assembly . . . 31

4.1 Simplified 3D wing isometric view . . . 33
4.2 Fixed support boundary condition at the wing root . . . 34
4.3 3D wing mesh . . . 35
4.4 Placement of modeled point masses on the wing structure . . . 36
4.5 Visualization of the `BeamNodes`, `spar_LE`, and `spar_TE` named selections on the 3D wing model . . . 36
4.6 3D wing modal analysis . . . 37
4.7 Spanwise deformations (u_x, u_z, θ_y) of the first five mode shapes of the 3D wing . . . 39
4.8 3D visualization of the global deformation fields for the first five modes . . . 40
4.9 Primary translational deformation u_z due to load case M_x . . . 43
4.10 Torsion deformation due to load case M_y . . . 43
4.11 Primary translational deformation u_x due to load case M_z . . . 44
4.12 Spanwise deformations (u_z, u_x, θ_y) due to unit moment loads . . . 45
4.13 Wing deformation under unit moment M_x . . . 46
4.14 Wing deformation under unit moment M_y . . . 46
4.15 Wing deformation under unit moment M_z . . . 46
4.16 Spanwise segmentation of the simplified wing model into four structural sections . . . 47
4.17 Spanwise divided 3D FEM wing as four sections 1 through 4 . . . 48
4.18 Bay 4 deformation under unit moment M_x . . . 49
4.19 Bay 4 deformation under unit moment M_y . . . 50

4.20 Bay 4 deformation under unit moment M_z 50
4.21 Linear static structural analysis for Bay 1 51
4.22 Linear static structural analysis for Bay 2 51
4.23 Linear static structural analysis for Bay 3 52
4.24 Linear static structural analysis for Bay 4 52
4.25 Spanwise segmentation of the 1D beam model into four sections 53
4.26 1D beam spanwise deformations 55
4.27 Quadratic fit to FEM-derived torsional constant $J(y)$ 57
4.28 Spanwise vertical displacement comparison 58
4.29 Spanwise horizontal displacement comparison 59
4.30 Spanwise twist comparison 59
4.31 Point masses along the 1D beam span 61
4.32 3D wing vs 1D beam MAC matrix heatmap 64
4.33 Orthogonal MAC matrices 64
4.34 1D beam modal spanwise deformation profile visualization for each mode 65

A.1 ANSYS-obtained effective modal mass data for modes 1-5 for all six DOFs 89
A.2 ANSYS-obtained effective modal mass data of 1D beam for modes 1-5 for all six DOFs 90

List of Tables

2.1 Summary of MSC NASTRAN capabilities for aeroelastic simulations . . . 9
2.2 Examples of CFD and FEM Solvers Used in Various Tools . . . 12
2.3 Qualitative comparison of aeroelastic modeling frameworks . . . 15

3.1 Comparison of wing placement configurations . . . 23
3.2 Impact of wing aspect ratio . . . 23
3.3 General effects of wing sweep angle . . . 24
3.4 Impact of wing sweep type . . . 25
3.5 Comparison of FW trade-offs . . . 27
3.6 Comparison of BWB trade-offs . . . 27
3.7 Scaled model aircraft parameters . . . 29
3.8 Estimated mass budget and location of components . . . 30

4.1 Overview of the removed features and their justification . . . 33
4.2 Material properties assigned and used in the FEM simulations . . . 34
4.3 Overview of point-mass allocation in the FEM model . . . 35
4.4 First five natural frequencies of the 3D wing system . . . 38
4.5 Classification of modes based on dominant effective mass contribution . . . 38
4.6 Rotations under unit moments about global axes . . . 41
4.7 Modeling options to reduce coupling and their trade-offs . . . 42
4.8 Linear static response of 3D wing to unit moment loads about principal axes . . . 44
4.9 Sensitivity of extracted stiffness values to remote point behavior and face selection . . . 45
4.10 Node and element counts for each FEM section model . . . 48
4.11 Sensitivity of section 4 stiffness to remote point behavior and face selection . . . 49
4.12 Extracted rotations and stiffness values per section using linear static unit moment loads 53
4.13 Spanwise segmented cross-sectional properties derived from stiffness-matching of FEM results . . . 54
4.14 Comparison of tip deformation results under unit moment loading: 3D FEM wing vs. segmented beam . . . 56
4.15 Global scaling factors applied to sectional properties . . . 57
4.16 Optimized cross-sectional properties for each beam segment . . . 57
4.17 Comparison of tip deformation results using optimized cross-sectional properties . . . 58
4.18 Mass properties of the 1D beam model . . . 60
4.19 Initial 1D beam modal frequencies . . . 61
4.20 Comparison of inertia tensor of 3D wing and 1D beam . . . 61
4.21 Initial 1D beam modal frequencies . . . 63
4.22 DOF participation for 1D beam modes . . . 63

A.1 Wing raw spanwise deformation dataset for mode 1 . . . 77
A.2 Wing raw spanwise deformation dataset for mode 2 . . . 80
A.3 Wing raw spanwise deformation dataset for mode 3 . . . 83
A.4 Wing raw spanwise deformation dataset for mode 4 . . . 85
A.5 Wing raw spanwise deformation dataset for mode 5 . . . 88
A.6 Beam raw spanwise modal deformation dataset for mode 1 . . . 93
A.7 Beam raw spanwise modal deformation dataset for mode 2 . . . 96
A.8 Beam raw spanwise modal deformation dataset for mode 3 . . . 99
A.9 Beam raw spanwise modal deformation dataset for mode 4 . . . 102
A.10 Beam raw spanwise modal deformation dataset for mode 5 . . . 105

Nomenclature

Abbreviations

Abbreviation	Definition
1D	One-Dimensional
3D	Three-Dimensional
AC	Aerodynamic Center
AIC	Aerodynamic Influence Coefficient matrix
BWB	Blended Wing Body
CFD	Computational Fluid Dynamics
CG	Center of Gravity
DLM	Doublet-Lattice Method
DOF	Degree(s) Of Freedom
EASA	European Union Aviation Safety Agency
FAA	Federal Aviation Administration
FEM	Finite Element Method
FSI	Fluid Structure Interactions
FW	Flying Wing
GEBT	Geometrically Exact Beam Theory
HALE	High Altitude Long Endurance
MAC	Modal Assurance Criteria
MPC	Multi-Point Constraint
OJF	Open Jet facility
PSD	Power Spectral Density
ROM	Reduced Order Model
SHARPy	Simulation of High-Aspect Ratio Planforms
TAW	Tube and Wing
UAV	Unmanned Aerial Vehicle
VLM	Vortex Lattice Method
UVLM	Unsteady Vortex Lattice Method

1

Introduction

1.1. Background

In pursuing sustainable aviation and reduced carbon emissions, the aerospace industry has adopted a key strategy: minimizing structural weight. This shift has led to the evolution of aircraft designs, ultimately increasing efficiency and cost-effectiveness by incorporating increased wingspans and higher aspect ratios. These adaptations enhance aerodynamic performance by improving lift-to-drag ratios. However, they also lead to more flexible structures, raising concerns about aeroelastic effects that may compromise stability and control.

Greater structural flexibility intensifies the coupling between flight and structural dynamics, presenting challenges in flight handling, ride quality, and overall safety. Consequently, aeroelastic analyses have become increasingly important in addressing flutter, divergence, and gust response. These concerns are further amplified in emerging configurations such as high-aspect-ratio Unmanned Aerial Vehicles (UAVs), solar-powered platforms, and advanced transport concepts that have pushed the limits of traditional analytical methods, which often operate at lower dynamic pressures and exhibit pronounced structural flexibility.

Among the aeroelastic concerns, the accurate prediction and analysis of gust loads has emerged as a critical area of focus. Flexible aircraft are particularly vulnerable to atmospheric disturbances, which can trigger complex unsteady responses and dynamic load amplification. As a result, reliable gust modeling is essential for optimizing structural performance and meeting certification standards. Regulatory bodies such as the European Union Aviation Safety Agency (EASA) and the Federal Aviation Administration (FAA) have responded to this need by enforcing stricter requirements for aeroelastic stability and dynamic load prediction under discrete and continuous gust conditions.

1.2. Problem Statement

Accurately predicting gust loads on flexible aircraft remains a key challenge in modern aeroelastic analysis. Historically, gust response analysis has often begun by estimating aerodynamic loads using the Doublet Lattice Method (DLM). While effective for conventional aircraft, this approach struggles with highly flexible configurations due to their pronounced structural deformations and changing aerodynamic properties. Gusts induce transient, dynamic loads that impose substantial stresses on aircraft structures such as wings and tailplanes, leading to complex structural responses that extend beyond the scope of traditional rigid-body or linear analyses. Modern approaches increasingly rely on high-fidelity, time-domain aeroelastic simulations that account for nonlinear structural behavior and non-planar aerodynamics to address these complexities. These methods are especially relevant when dealing with large deformations and flow phenomena such as separation or shock motion, conditions under which linear assumptions become insufficient. A well-documented example of the risks associated with inadequate modeling is the Helios mishap [1], which highlights the need for accurate dynamic load prediction in highly flexible aircraft.

1.3. Research Objectives

As flexible, high-aspect-ratio aircraft become increasingly prominent in modern design, so does the need for test environments that can accurately reproduce their dynamic aeroelastic behavior. Wind tunnel experiments remain indispensable for validation and control development, particularly when supported by numerical models that can replicate free-flight conditions. Within aircraft certification and experimental validation, there is growing interest in simulation-driven workflows that bridge the gap between computational predictions and physical testing.

Sodja and De Breuker [2] introduced a hybrid methodology to enhance the fidelity of aeroelastic wind tunnel testing. Their framework integrates measured aerodynamic loads into a simulation to estimate aircraft motion, which is then used to control the motion of the physical model. To demonstrate the feasibility of this concept, they tested a simplified feedforward approach in which the free-flight aeroelastic response was simulated in advance and prescribed to the wind tunnel model as a motion profile. This proof-of-concept demonstrated the method's potential, but it was based on an idealized aircraft configuration with a very high aspect ratio and extremely low flight speed. While suitable for demonstrating the principle, such a setup is not directly transferable to practical wind tunnel environments, where geometric, speed, and control constraints must be considered.

In this context, the present thesis aims to contribute by delivering a feasible design and a validated numerical model of a flexible, high-aspect-ratio aircraft, tailored for testing in TU Delft's Open Jet Facility. Beyond experimental feasibility, this model provides numerical support for aeroelastic studies that refine motion profiles and control strategies for increased-fidelity testing. Accordingly, the formal objective of this thesis is framed as follows:

To design a flexible aircraft model for wind tunnel free-flight testing, and to develop its equivalent beam representation for increased-fidelity aeroelastic testing.

This equivalent beam representation provides a simplified structural model of the aircraft wing, which will serve as the basis for aeroelastic investigations in the increased-fidelity testing framework. To achieve this objective, the following three sub-questions are addressed:

1. What level of fidelity is required for a flexible aircraft model to exhibit aeroelastic effects while being suitable for free-flight wind tunnel testing?
2. How can the structural dynamic properties of the aircraft be represented by an equivalent beam model that reflects its main stiffness and inertia properties?
3. How can the equivalent beam model be validated to ensure it reproduces the main structural characteristics of the aircraft?

Answering these questions provides a validated structural representation of the flexible aircraft, which supports the broader goal of enabling aeroelastic gust simulations and motion-profile-driven experimental testing.

1.4. Methodology

This thesis applies numerical techniques to develop and validate an equivalent beam representation of a flexible model aircraft. The approach combines conceptual design, detailed finite element modeling, and structural reduction techniques to ensure that the resulting beam model captures the essential dynamic behavior of the aircraft while remaining computationally efficient. The workflow is divided into three phases, each building on the previous one to address the research sub-questions systematically. Figure 1.1 provides an overview of the adopted method.

Phase 1: Model aircraft design

In the first phase, a physical aircraft model is developed by defining the main wind tunnel requirements, drawing on literature for design considerations, and selecting initial parameters. The aim is to produce a model that shows meaningful aeroelastic effects while feasible for wind tunnel experimentation. This process results in a detailed three-dimensional wing model that is the basis for subsequent structural analysis.

Phase 2: Structural modeling

The flexible wing's detailed finite element model is developed in ANSYS R2 2023 in the second phase. Static analyses evaluate deformation and extract stiffness properties, while modal analyses capture the wing's dynamic properties. Sensitivity studies are included to confirm the consistency of the linear static deformation results. The extracted properties form the basis for an equivalent beam model that reflects the main structural properties of the finite element wing while reducing complexity.

Phase 3: Derivation of an equivalent beam model

The final phase focuses on validating the equivalent beam model against the finite element wing. Static deformation tests and modal analyses are carried out to assess how well the beam reproduces the wing's bending, torsional, and coupled responses. This validation ensures that the simplified beam retains the fidelity required for aeroelastic analysis while remaining computationally efficient.

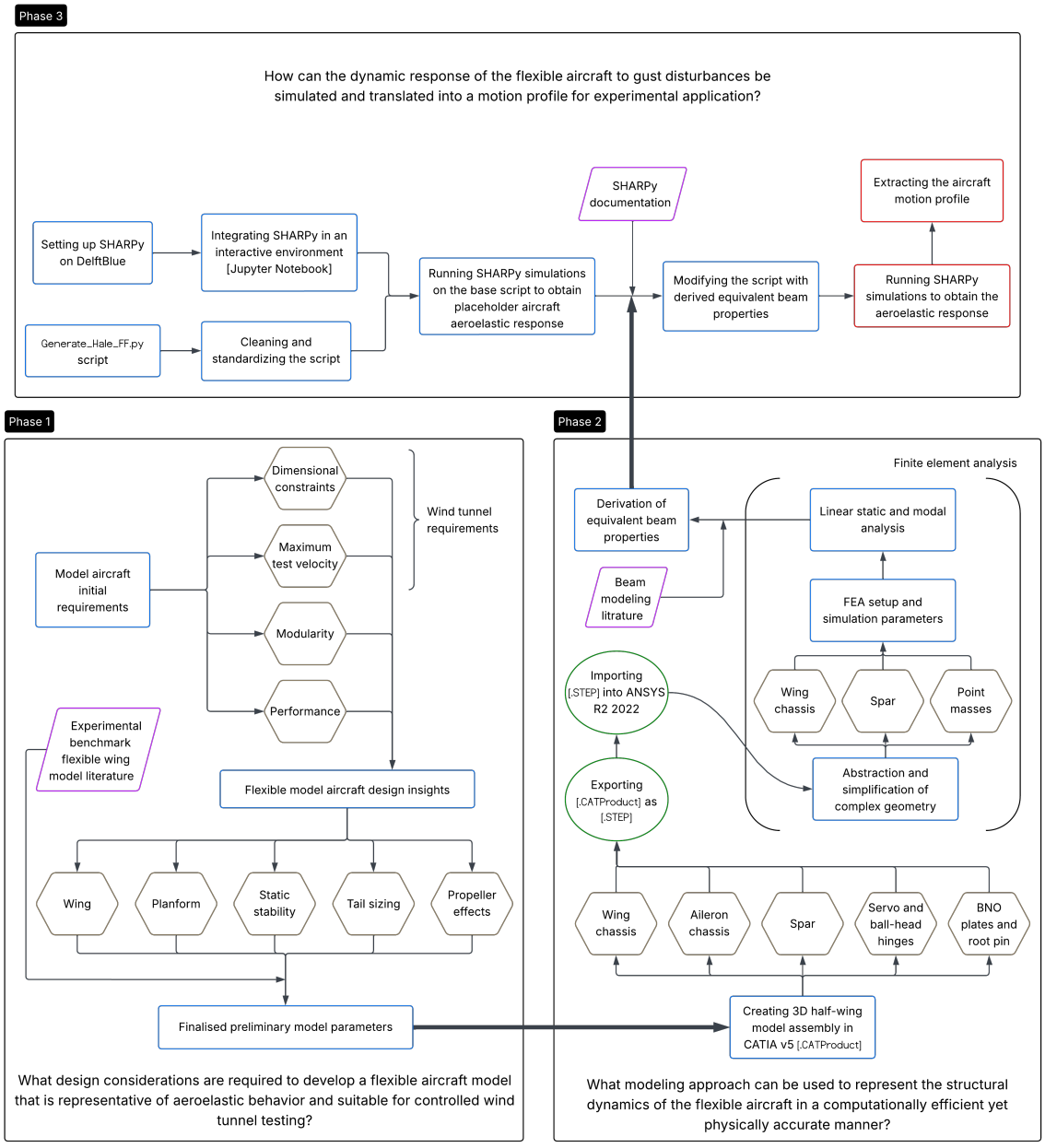

Figure 1.1: Methodology and the overarching goal

2

Literature Review

This chapter reviews the state of the art in modeling and simulating the aeroelastic response of flexible aircraft structures under gust disturbances. Modern aircraft adopt higher aspect ratios and lighter materials to improve aerodynamic efficiency, making them increasingly sensitive to unsteady aerodynamic loading and aeroelastic coupling. The chapter reviews gust modeling approaches, including discrete and continuous representations, to provide a comprehensive background for this thesis. A comparison of major aeroelastic frameworks, from classical modal-based tools to nonlinear time-domain platforms, is provided, followed by an overview of hybrid coupling approaches. Experimental methods are also examined, categorizing key techniques into free-flight, hybrid simulation, and benchmark model studies. Finally, the chapter outlines a focused research gap, motivating the development of a validated equivalent beam model as an initial step toward the broader goal of increased-fidelity aeroelastic testing of flexible aircraft.

2.1. Gust Modeling in Aeroelastic Analysis

Understanding the influence of atmospheric gusts on aircraft structures is a fundamental aspect of aeroelastic analysis. Gust-induced loads can cause unsteady aerodynamic forces, triggering complex structural responses that significantly affect flight stability and fatigue life, particularly in flexible aircraft. Accurate modeling of these disturbances is crucial for predicting transient load distributions and evaluating structural stability under operational conditions [3]. Developing and applying gust models is essential for simulating realistic environments and ensuring compliance with regulatory standards. This section reviews the theoretical foundations and practical implementations of gust modeling approaches used in industry and research.

2.1.1. Classification of Gusts

Gusts are typically classified according to their direction relative to the aircraft's flight path. *Vertical gusts* act perpendicular to the trajectory and dominate the aeroelastic response because of their direct influence on lift. *Longitudinal gusts*, aligned with the flight direction, primarily affect drag and acceleration. *Lateral gusts*, oriented side-to-side, influence yaw stability and sideslip behavior. Figure 2.1 illustrates these directional types.

In addition to directionality, gusts can also be distinguished by their temporal characteristics. *Discrete gusts* are deterministic profiles representing isolated disturbances widely used in certification analysis. By contrast, *Continuous gusts* represent atmospheric turbulence modeled statistically over time. This classification is summarized in Figure 2.2.

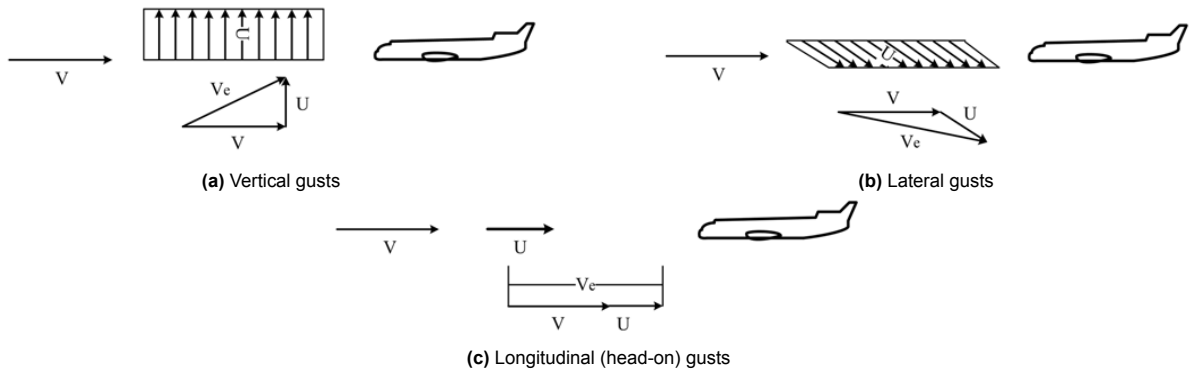

(a) Vertical gusts

(b) Lateral gusts

(c) Longitudinal (head-on) gusts

Figure 2.1: Gust directionality [3]

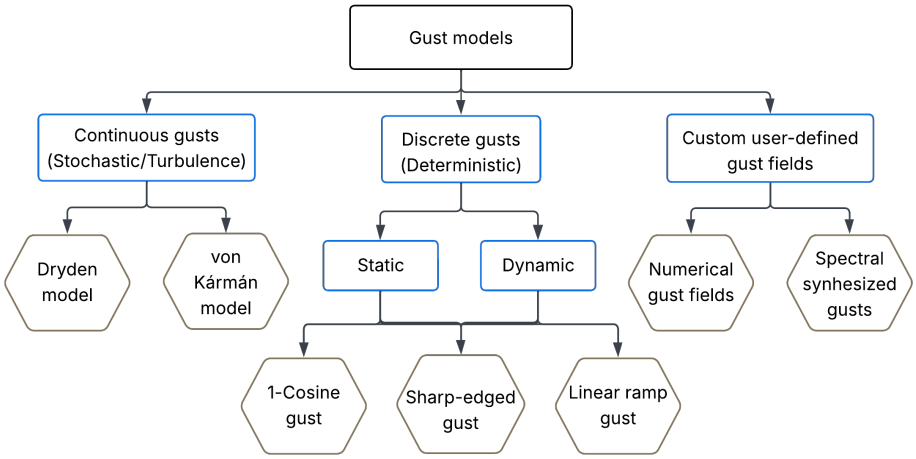

Figure 2.2: Classification of gust models

2.1.2. Discrete Gust Models

Discrete gusts are favored for certification and design due to their simplicity and repeatability. The most common profiles include:

1-Cosine Gust

Widely adopted in CS-25 [4] and FAR-25 [5], the 1-cosine gust simulates a smooth gust profile that increases and decreases in velocity following a cosine function. It is defined as:

$$\begin{aligned} u_g(x) &= \frac{U_{ds}}{2}\left[1 - \cos\left(\frac{\pi x}{H}\right)\right] = \sin^2\left(\frac{\pi x}{2H}\right) \qquad \text{for } 0 < x < 2H \\ u_g(x) &= 0 \qquad\qquad\qquad\qquad\qquad\qquad\qquad\qquad\qquad\qquad\quad \text{otherwise} \end{aligned} \tag{2.1}$$

Where $u_g(x)$ is the gust-induced velocity at a distance x along the flight path, U_{ds} is the design (peak) gust velocity, H is the gust gradient distance or half-length, and π is the mathematical constant pi arising from the periodic nature of the cosine function.

Sharp-Edged Gust

This step input models an instantaneous change in velocity, mainly for theoretical and control analyses [3].

$$u_g(x) = \begin{cases} U_{ds}, & x \geq 0 \\ 0, & x < 0 \end{cases} \tag{2.2}$$

Linear-Ramp Gust

Models a gradual gust encounter with linear rise, useful for comparing aircraft response variability [3].

$$u_g(x) = \begin{cases} \frac{U_{ds}}{H} \cdot x, & 0 \leq x \leq H \\ U_{ds}, & x > H \\ 0, & x < 0 \end{cases} \tag{2.3}$$

These profiles are typically applied at the aircraft's aerodynamic center or center of gravity. Figure 2.3 shows velocity distributions.

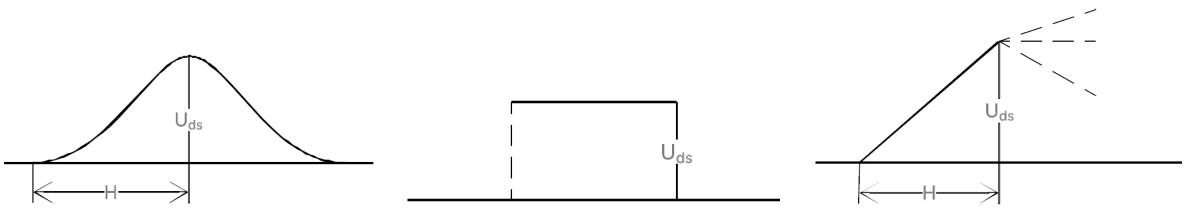

(a) 1-Cosine **(b)** Sharp-edged **(c)** Linear-ramp

Figure 2.3: Velocity distributions of discrete gust models

Dynamic gust loading involves inertial forces due to elastic-mode accelerations. Governing equations typically involve time-marching structural and aerodynamic coupling, accounting for modal response and load integration [3]. While the gust gradient may seem arbitrary in static load prediction, it significantly influences dynamic response [6].

2.1.3. Continuous Gust Models

Continuous turbulence models define atmospheric disturbances in the frequency domain via their Power Spectral Density (PSD). However, these spectra can generate time histories using shaping filters or frequency-domain (Fourier) synthesis methods. These models are vital in evaluating system responses over long periods and are commonly used in flight control design and flutter clearance [3, 7, 8]. The most common models are:

Dryden Model

Well-suited for control analysis due to rational transfer functions [9].

$$\Phi_w(\omega) = \frac{2\sigma_w^2 L_w}{\pi V} \cdot \frac{1 + 3\left(\frac{L_w\omega}{V}\right)^2}{\left[1 + \left(\frac{L_w\omega}{V}\right)^2\right]^2} \tag{2.4}$$

$$\Phi_u(\omega) = \frac{2\sigma_u^2 L_u}{\pi V} \cdot \frac{1}{1 + \left(\frac{L_u\omega}{V}\right)^2} \tag{2.5}$$

von Kármán Model

Preferred in certification due to superior agreement with flight data and theoretical behavior [10]:

$$\Phi_u(\omega) = \frac{2\sigma_u^2 L_u}{\pi V} \cdot \left[1 + \left(\frac{1.339 L_u\omega}{V}\right)^2\right]^{-5/6} \tag{2.6}$$

$$\Phi_w(\omega) = \frac{2\sigma_w^2 L_w}{\pi V} \cdot \left[1 + \left(\frac{1.339 L_w\omega}{V}\right)^2\right]^{-11/6} \tag{2.7}$$

Where $\Phi_w(\omega)$ and $\Phi_u(\omega)$ are the PSDs of the vertical (w) and longitudinal (u) gust velocity components, respectively. The terms σ_w^2 and σ_u^2 represent the turbulence intensities (variances) in the vertical and longitudinal directions, L_w and L_u are the corresponding turbulence scale lengths, V is the mean airspeed of the aircraft, and ω is the angular frequency of the gust.

Figure 2.4 compares the PSDs of both models. Source code and settings used to generate the curves are detailed in Appendix A.1.

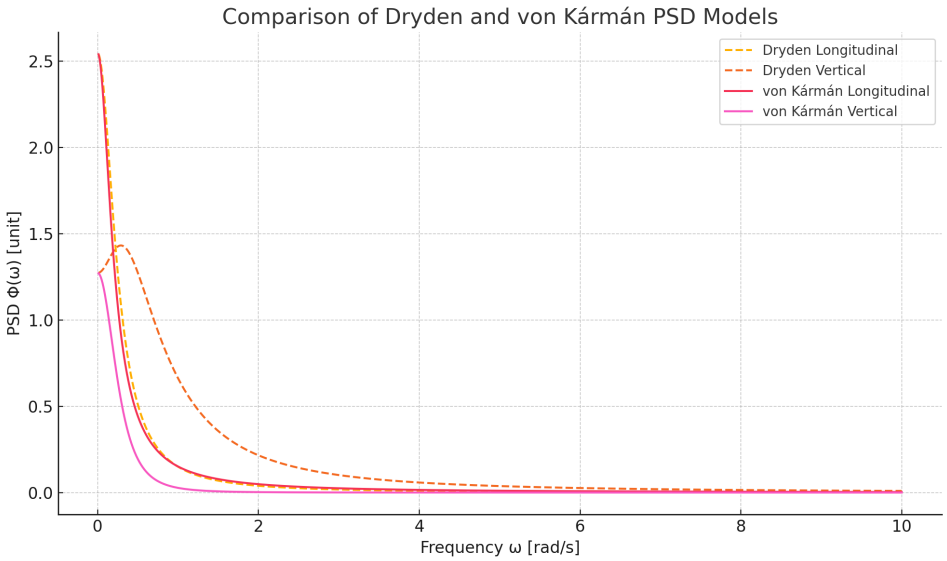

Figure 2.4: Comparison of Dryden and von Kármán PSDs

While continuous models offer more realistic representations, discrete gusts remain central to certification. Flight data recorders show that extreme gusts often appear as isolated events [3, 11]. As such, both approaches remain essential under EASA and FAA guidelines [4, 5].

2.2. Aeroelastic Simulations Tools and Modeling Approaches

Aeroelastic simulations integrate aerodynamic and structural solvers to capture the coupled response of flexible aircraft to external disturbances such as gusts. The choice of simulation tool strongly depends on the required fidelity, computational cost, and the specific nature of the study, whether it's certification, design optimization, or advanced research. Over the years, several computational frameworks have emerged, each implementing different numerical methods and offering varied capabilities. This section reviews three significant categories of such tools: industrial solvers based on modal Finite Element Method - Doublet Lattice Method (FEM–DLM) coupling, research-oriented time-domain frameworks using Unsteady Vortex Lattice Method (UVLM) and Geometrically Exact Beam Theory (GEBT) models, and high-fidelity Computational Fluid Dynamics CFD–FEM approaches used in state-of-the-art simulations.

2.2.1. MSC NASTRAN

NASTRAN (NASA Structural Analysis) is a widely used, industry-standard finite element solver with robust linear and nonlinear structural analysis capabilities. For aeroelastic applications, it implements DLM in its frequency-domain solvers, notably SOL 144 (static trim), SOL 145 (flutter), and SOL 146 (gust response). These modules rely on reduced-order modal representations of structural dynamics, enabling computational efficiency for certification-level analyses. A typical NASTRAN aeroelastic workflow involves:

- Modal analysis (SOL 103) to extract natural frequencies and mode shapes,
- Modal truncation to retain dominant flexible modes,
- Generation of Aerodynamic Influence Coefficient matrix (AIC) via DLM,

- Formulation of the coupled aeroelastic system in the frequency domain,
- Optional inclusion of rigid-body modes and control surface effects.

Governing Equations

1. The aeroelastic system is typically written as:

$$\left[-\omega^2 \mathbf{M} + i\omega \mathbf{C}_a(\omega) + \mathbf{K} + \mathbf{K}_a(\omega)\right] \mathbf{q} = \mathbf{F}_{\text{ext}}(\omega) \tag{2.8}$$

   Where $\mathbf{M}$ and $\mathbf{K}$ are the structural mass and stiffness matrices, and $\mathbf{C}_a(\omega)$, $\mathbf{K}_a(\omega)$ are the aerodynamic damping and stiffness matrices derived from DLM. The reduced frequency is defined as $k = \omega b / U_\infty$.

2. Aerodynamic forces are computed via:

$$\mathbf{F}_{\text{aero}}(\omega) = \mathbf{Q}(\omega)\, \mathbf{q}(\omega) \tag{2.9}$$

   where $\mathbf{Q}(\omega)$ is the AIC matrix.

Linear Analysis (SOL 144 and SOL 146)

Linear analysis in NASTRAN using DLM assumes small perturbations, incompressible and inviscid flow, planar lifting surfaces, and enforces the downwash condition at the three-quarter chord point. In linear trim (SOL 144), the lifting surface is modeled using a panel grid with quarter-chord vortex placement and aerodynamic loads updated from trim parameters. Gust profiles such as the 1-cosine shape are introduced via the `GUST` card.

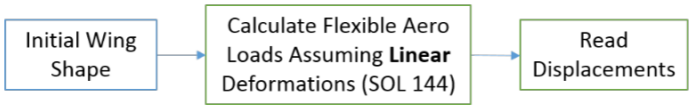

Figure 2.5: Linear aeroelastic workflow using SOL 144 [12]

These modules are suited for:

- Flutter boundary predictions,
- Gust load factor estimations,
- Modal stability and control surface analysis,
- Integration with control systems in state-space form.

Quasi-Nonlinear Coupling

A quasi-nonlinear workflow couples SOL 144 (DLM) with SOL 106 (nonlinear static) to overcome linear limitations. Aerodynamic loads are applied to a deformed structural mesh without feedback iteration.

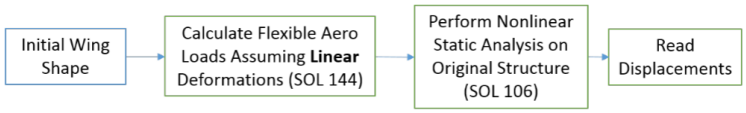

Figure 2.6: Quasi-nonlinear aeroelastic coupling in NASTRAN [12]

Fully Nonlinear Iterative Coupling

A nonlinear iterative process is employed for strongly flexible wings or large deformations, such as high-altitude-long-endurance (HALE) aircraft. Aerodynamic loads from SOL 144 are computed on a rigid mesh and iteratively updated based on nonlinear displacements computed by SOL 106.

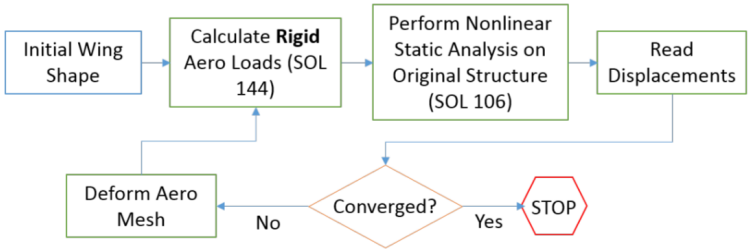

Figure 2.7: Iterative nonlinear coupling using NASTRAN modules [12]

Each iteration updates the aerodynamic mesh orientation to reflect the deformed wing geometry. Although this approach enables better accuracy for large-deflection scenarios, it is not natively supported in NASTRAN and is typically orchestrated via MATLAB or Python scripts. Limitations include:

- No unsteady aerodynamic modeling (DLM remains steady/harmonic),
- High computational expense due to external iteration.

Overall, MSC NASTRAN remains a validated and widely adopted platform for linear aeroelastic analysis using modal FEM and DLM. Its frequency-domain solvers (SOL 144, 145, 146) provide efficient workflows for regulatory compliance. However, for strongly nonlinear or time-domain scenarios, such as gusts acting on highly flexible configurations, its native capabilities are limited. Table 2.1 presents an overview of the strengths and limitations of MSC NASTRAN's aeroelastic capability.

Advantages	**Limitations**
Industry-grade reliability and validation	Frequency-domain only; no direct time-domain solver
Efficient for linear flutter and gust certification	Assumes linear structural and aerodynamic behavior
Supports quasi-nonlinear workflows via external coupling	Requires scripting for fully nonlinear workflows
Integrated modal and control system analysis	Lacks wake roll-up, unsteady aerodynamic modeling

Table 2.1: Summary of MSC NASTRAN capabilities for aeroelastic simulations

2.2.2. SHARPy

SHARPy (Simulation of High-Aspect-Ratio Planforms) is a versatile, open-source, Python-based aeroelastic solver developed at Imperial College London [13]. It couples UVLM with GEBT, enabling fully nonlinear, time-domain simulations of flexible aircraft structures. SHARPy supports both linear and nonlinear simulations, and its modular architecture makes it suitable for a wide range of aeroelastic applications, including flutter, gust loads, free-flight, and control system integration [2, 14–18].

Modular Solver Architecture

SHARPy is built around a modular solver framework, illustrated in Figure 2.8, where the analysis flow is defined in a case file using a sequence of solver modules. Each solver handles a specific simulation aspect, allowing users to construct tailored workflows. Common modules include:

- `BeamLoader` – Loads structural definitions (GEBT-based composite beams)
- `AerogridLoader` – Sets up aerodynamic grids for UVLM
- `AerogridUnsteady` – Computes unsteady aerodynamic loads using UVLM (bound and wake vortex rings)
- `StructuralDynamicCoupledStep` – Solves the nonlinear, coupled aeroelastic problem
- `Modal`, `LinearAssembler`, `StabilityDerivatives` – For linearization, modal reduction, and control

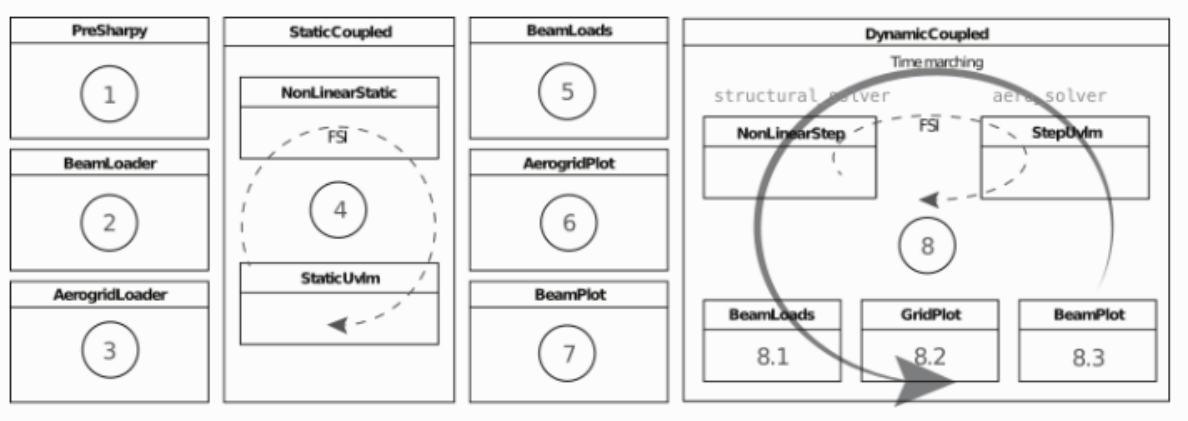

Figure 2.8: SHARPy's modular framework for a nonlinear, time-marching aeroelastic simulation [19]

Case File Configuration

SHARPy simulations are configured using a main `.sharpy` configuration file in combination with several structured `.h5` files. Each file defines a specific subsystem of the simulation. This modular setup allows easy swapping of structural, aerodynamic, or multibody definitions.

```
[SHARPy]
flow = ['BeamLoader', 'ArogridLoader'
        'AerogridUnsteady', 'StructuralDynamicCoupledStep']
```

The key `.h5` input files include:

- `.fem.h5`: Defines the structural model using GEBT and contains:
  - Node and element definitions
  - Local stiffness and mass matrices
  - Boundary conditions and lumped masses
  - Beam orientations and element connectivity
- `.aero.h5`: Describes the aerodynamic surface grid for UVLM. It includes:
  - Panel mesh (aligned with FEM grid)
  - Airfoil sections and elastic axis locations
  - Lifting and non-lifting surface tags
  - Twist, sweep, and chord distributions
- `.mb.h5`: Specifies multibody configurations, used to:
  - Define multiple interconnected bodies
  - Introduce joints, hinges, and relative motions
  - Set parent-child topologies
- `.nonlifting_body.h5`: Optional file for modeling fuselages or other bluff bodies without lift. It specifies:
  - Axis geometry (circular or elliptical)
  - Offsets and scaling factors
- `.dyn.h5`: Provides time-varying external loads or motion profiles:
  - Forces and moments applied at specific nodes
  - Rigid-body motion states (position, velocity)
  - Gust inputs or prescribed trajectories
- `.lininput.h5`(Optional): Contains input data for linearization routines (e.g., to generate state-space models).
- `.rom.h5`(Optional): Stores parameters for reduced-order models (ROMs), used for fast control-oriented simulations.

Together with the solver sequence defined in the `.sharpy` file, these inputs enable complex, customizable, and nonlinear coupled aeroelastic simulations in SHARPy.

Governing Equations and Coupling

SHARPy solves the coupled nonlinear aeroelastic equations using a time-domain formulation. GEBT equations govern the structural dynamics, while aerodynamic forces are computed using UVLM:

$$\mathbf{M}\ddot{\mathbf{q}} + \mathbf{C}(\mathbf{q}, \dot{\mathbf{q}}) + \mathbf{K}(\mathbf{q}) = \mathbf{f}_{\text{aero}}(t) \tag{2.10}$$

$$\mathbf{f}_{\text{aero}}(t) = \text{UVLM}(\mathbf{q}, \dot{\mathbf{q}}, t) \tag{2.11}$$

The coupled equations are solved iteratively at each time step, ensuring accurate load-displacement compatibility between structural and aerodynamic domains.

Simulation Capabilities

SHARPy enables a wide range of aeroelastic analyses:

- Time-domain simulation of gust, maneuver, and free-flight responses,
- Nonlinear trim analysis for steady deformed flight conditions,
- Generation of linearized state-space models for control design and frequency analysis,
- Multibody configurations with hinges, constraints, and actuators,
- External control system integration using a transmission control protocol interface.

A unique strength of SHARPy is its ability to simulate free-flight conditions by dynamically coupling rigid-body motion with structural and aerodynamic solvers. This enables analysis of complex aeroelastic interactions involving pitch–plunge–bending coupling, nonlinear trim, and transient gust responses. Gusts are introduced as velocity perturbation fields superimposed on the freestream and can be defined using standard profiles (e.g., 1-cosine, step, sine) in either body-fixed or inertial frames. Arbitrary gust shapes are also supported, facilitating detailed studies of gust response and mitigation strategies [2].

State-Space Linearization

SHARPy can generate linear state-space models of the form:

$$\dot{\mathbf{x}} = \mathbf{A}\mathbf{x} + \mathbf{B}\mathbf{u}, \quad \mathbf{y} = \mathbf{C}\mathbf{x} + \mathbf{D}\mathbf{u} \tag{2.12}$$

where $\mathbf{x}$ includes structural and aerodynamic states. These models enable control design, flutter prediction, and gust analysis in the frequency domain.

Summary and Applications

SHARPy stands out due to its:

- Fully nonlinear, time-resolved aeroelastic simulation capability
- Compatibility with experimental test data and motion prescription
- Open-source and extensible design, supporting custom solver development
- Relevance to gust load alleviation, flexible aircraft, and flight control

These features make SHARPy particularly suitable for academic and research applications where flexibility, nonlinearity, and free-flight dynamics must be captured with high fidelity.

2.2.3. CFD-FEM Coupling Tools

The use of coupled CFD-FEM frameworks represents the current high-fidelity frontier of aeroelastic modeling, particularly for nonlinear, time-domain simulations involving large structural deformations and complex unsteady flows [20]. These tools are often employed when lower-order methods (e.g., DLM, UVLM) cannot capture critical fluid-structure interaction (FSI) phenomena, such as shock waves, flow separation, or boundary layer effects in gust-loaded or maneuvering conditions.

Framework Overview

CFD-FEM coupling typically integrates:

- A Navier–Stokes-based CFD solver (e.g., FUN3D, TAU, SU2, or elsA),
- With a nonlinear FEM-based structural solver (e.g., ANSYS, NASTRAN SOL 400, ABAQUS).

These simulations are performed in the time domain, with the flow and structure solvers exchanging data such as surface pressure and deformation iteratively at each timestep. An example from ONERA's framework, *elsA*, is shown in Figure 2.9, which illustrates the CFD–FEM coupling process showing mesh deformation and data exchange between solvers.

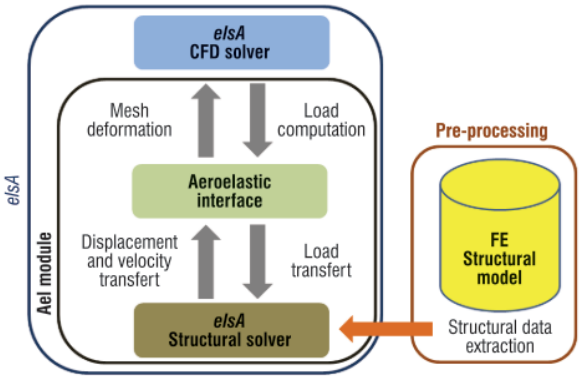

Figure 2.9: *elsA* CFD-FEM solver schematic [21]

Coupling Strategies

The coupling can be realized through:

- Loose (weak) coupling where data is exchanged once per timestep; faster but potentially unstable for strong FSI.
- Strong coupling where sub-iterations per timestep ensure convergence of the fluid-structure system; more stable but computationally expensive.

The second-order differential equation governs the structural dynamics:

$$\mathbf{M}\ddot{\mathbf{u}} + \mathbf{C}\dot{\mathbf{u}} + \mathbf{K}\mathbf{u} = \mathbf{F}_{\text{aero}}(t) \tag{2.13}$$

where $\mathbf{F}_{aero}$ is updated from CFD at each timestep.

Gust Response and Nonlinear Effects

CFD-FEM tools can directly model 1-cosine discrete gusts, atmospheric turbulence (e.g., von Kármán models), and shock-induced unsteady behavior [22]. They inherently resolve:

- Flow separation and shock–boundary layer interaction,
- Transonic flutter,
- Buffeting due to wake interference.

However, they are generally prohibitively expensive for routine design tasks or broad parametric studies. The active research areas include mesh deformation (via ALE or overset grids), convergence criteria, and the coupled solver's stability.

Example Tools and Applications

Tool	CFD Solver	FEM Solver	Notes
FUN3D	FUN3D	NASTRAN / Abaqus	NASA's high-fidelity suite; used in transonic aeroelastic benchmarks
elsA	ONERA elsA	Samcef / ZEbuLoN	Applied in European gust response studies [21]
TAU	DLR TAU	Carat / Samcef	Used in DLR's flow-excited wing flutter studies
SU2	SU2	CalculiX / Code_Aster	Open-source toolchain [22]

Table 2.2: Examples of CFD and FEM Solvers Used in Various Tools

Limitations

- Complex setup: Requires meshing, deformation tracking, and coupling interface coding.
- Scalability: Not suited for optimization or real-time simulation without surrogate models.

Use cases

Despite limitations, CFD-FEM tools are critical in:

- Certification-level gust load prediction,
- Validating ROM-based models,
- Capturing flow–structure interaction where other models fail.

2.2.4. Other Frameworks

This subsection presents alternative aeroelastic modeling frameworks explored in the literature, focusing on their applicability to nonlinear static analyses of highly flexible wings. These methods include NeoCASS, intrinsic beam formulations, continuous shape-function ROMs, and rigid multibody dynamics. Their common goal is accurately capturing large structural deformations and their interaction with unsteady aerodynamics under static or slowly varying loading.

NeoCASS

NeoCASS, developed at Politecnico di Milano, is an open-source conceptual design suite integrating structural sizing and aeroelastic modeling. It combines a geometrically nonlinear beam formulation with iterative coupling to uncorrected Vortex Lattice Method (VLM) or strip theory aerodynamics. The solver computes aerodynamic loads on an initially undeformed mesh and applies them incrementally within a nonlinear structural loop. Key process steps involve:

- Incremental application of aerodynamic loads.
- Nonlinear structural solution with updated stiffness and internal forces.
- Infinite plate spline deformation and aerodynamic loop restart.
- Convergence achieved via displacement-based criteria with damping.

Figure 2.10 illustrates the iterative process adopted in NeoCASS for static aeroelastic analysis [12].

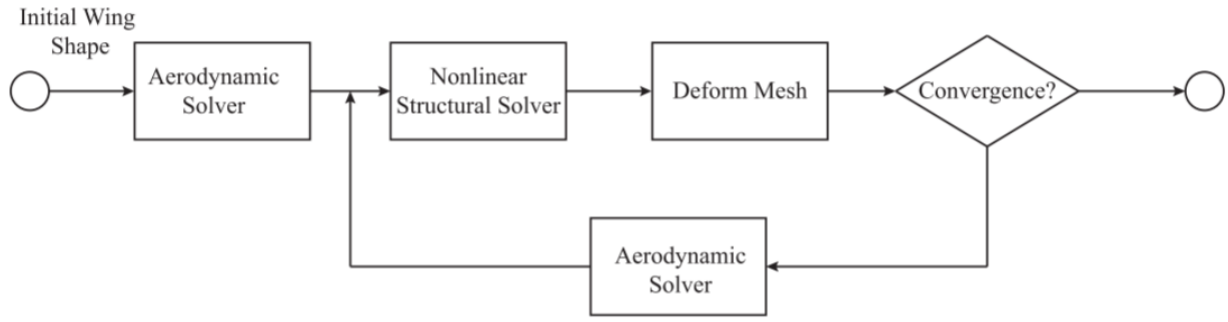

Figure 2.10: NeoCASS aeroelastic solver [12]

Intrinsic Beam Models

The intrinsic beam method simplifies the governing nonlinear equations by directly modeling intrinsic quantities (e.g., curvature, twist, stretch). A finite-element discretization allows a solution in complex geometries. Standard VLM-based aerodynamics are applied in the body-fixed frame. Multiple reference frames (inertial, local beam, aerodynamic, and inflow) are defined to facilitate coordinate transformation and load application. The governing equations use a rotation matrix:

$$[C^{GB}(s)] = [e_x(s)\, e_y(s)\, e_z(s)] \tag{2.14}$$

Lift and gravity vectors are projected via the inflow frame:

$$U_G = \begin{bmatrix} \cos(\alpha) \\ 0 \\ \sin(\alpha) \end{bmatrix} U_\infty, \quad g_G = \begin{bmatrix} g\sin(\alpha) \\ 0 \\ -g\cos(\alpha) \end{bmatrix}$$

Continuous Shape Function ROMs

This approach expresses wing deflections using weighted shape functions, enabling reduced-order modeling of nonlinear structural dynamics. It is computationally efficient and suitable for rapid analysis. The strain energy is expressed via a stiffness potential, with virtual work principles used to incorporate external forces and aerodynamic loading via VLM:

$$F_I(s) = \rho U_\infty \Gamma(s)$$

Where $\Gamma(s)$ is the circulation generated along the quarter-chord.

Rigid Multibody Dynamics

Implemented in LMS Virtual.Lab Motion, this method discretizes the wing into rigid bodies connected via six degrees of freedom (DOF) beam force elements. Equations of motion form a nonlinear differential algebraic equation system, solved using backward differentiation formulas. Aerodynamic loads are modeled using strip theory, applied directly at aerodynamic centers:

$$\alpha_B(s) = \sin^{-1}\left(\frac{e_Z(s)\cdot U_G}{\|U_G\|}\right), \quad L(s) = \frac{1}{2}\rho U_\infty c C_{L,\alpha}(s)\alpha_B(s)$$

This finite segment method captures large deformations while retaining numerical efficiency [23–26].

Comparative Analysis

A detailed comparative study by Howcroft et al. [12] evaluated each framework under tip load, static angle-of-attack sweeps, and aeroelastic load tracking. Results are presented in Figure 2.11, showing strong agreement between NeoCASS, intrinsic beam, and continuous ROM models. The multibody method also showed good agreement but diverged due to strip theory aerodynamics.

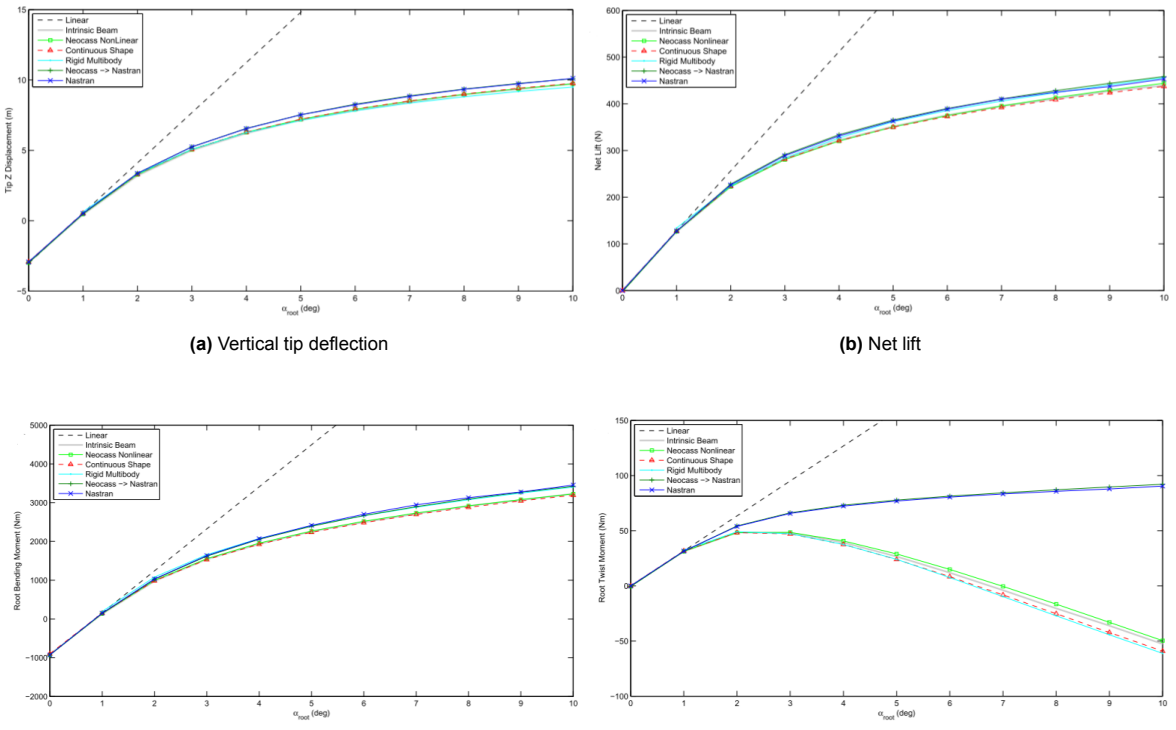

(a) Vertical tip deflection

(b) Net lift

(c) Root bending moment

(d) Root twist

Figure 2.11: Variation in aeroelastic quantities vs angle of attack [12]

2.2.5. Comparative Summary of Frameworks

Aeroelastic modeling frameworks span a broad spectrum regarding fidelity, computational cost, and applicability. Table 2.3 provides a qualitative comparison of the frameworks discussed in this section across key modeling features.

Framework	Solver Domain	Structure Model	Aero Model	Nonlinear Effects	Gust Capable	Computational Cost
MSC NASTRAN	Frequency	Linear / Quasi-nonlinear	DLM	Limited / Iterative	✓(linear gust)	Low–Moderate
SHARPy	Time	GEBT (nonlinear beam)	UVLM	Full geometric	✓	Moderate
CFD-FEM	Time	Nonlinear FEM	RANS / Navier-Stokes	Full geometric	✓	Very High
NeoCASS	Static Iterative	Nonlinear beam (ROM)	Strip / VLM	Geometric nonlinearities	✓(static gust)	Low–Moderate
Intrinsic Beam	Static / Dynamic	Geometrically exact beam	VLM	Full geometric	✓	Low–Moderate
Cont. Shape ROM	Static	Shape function ROM	VLM	Moderate–High	✓	Very Low
Rigid Multibody	Time (DAE)	Rigid segments + springs	Strip Theory	Large rigid motion only	✓(via Strip)	Low

Table 2.3: Qualitative comparison of aeroelastic modeling frameworks

Figure 2.12 offers a conceptual map for selecting a suitable framework depending on structural flexibility, desired fidelity, and computational constraints.

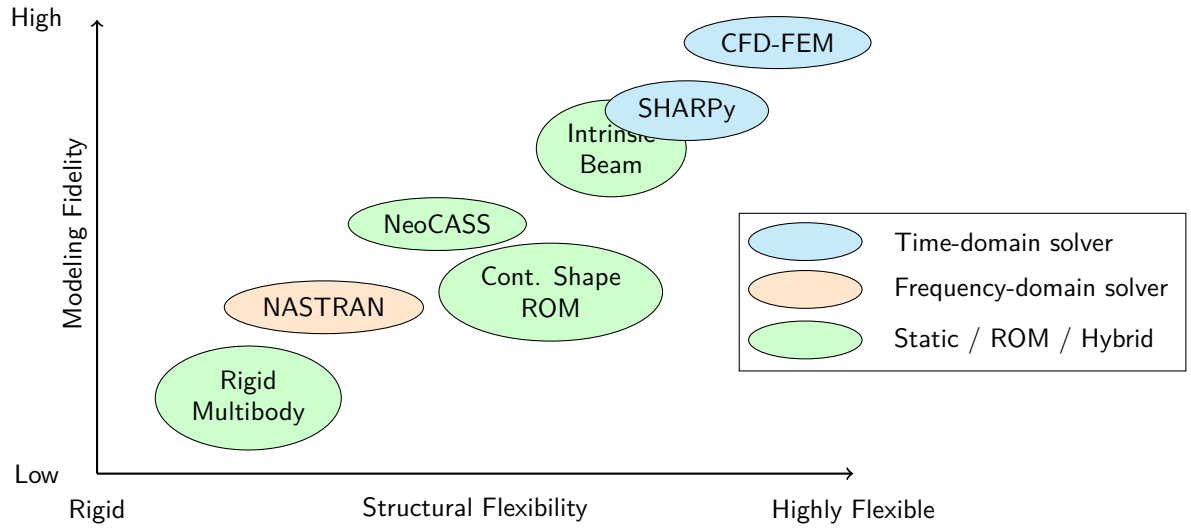

Figure 2.12: Framework selection map with solver domain classification

Discussion

Lower-order frameworks like MSC NASTRAN and NeoCASS remain valuable for preliminary design, certification studies, or systems with moderate flexibility. SHARPy and intrinsic beam approaches offer significant nonlinear modeling capability at a relatively modest cost. CFD-FEM coupling is reserved for high-fidelity investigations requiring detailed flow resolution, such as transonic flutter or shock-boundary-layer interaction. Continuous ROMs provide a computationally efficient way to include large deflection behavior for rapid evaluation. At the same time, rigid multibody frameworks are best suited for subsystem-level control analysis and simplified aeroelastic loads. Ultimately, the selection of an appropriate framework depends on:

- The degree of structural flexibility.
- The required fidelity of aerodynamic modeling.
- Available computational resources.
- Target application: design, control, certification, or research.

2.3. Experimental Methods for Gust Response

Experimental investigations play a crucial role in aeroelastic research by validating simulation models, revealing complex FSIs, and supporting the development of ROMs. Various techniques have been explored for gust response testing, including differing boundary conditions, gust generation methods, and the structural flexibility of the tested configuration. Unlike purely computational approaches, physical testing captures real-world nonlinearities, structural damping, actuator effects, and manufacturing imperfections. This section highlights selected experimental categories most relevant to the present numerical modeling approach: free-flight testing, hybrid methods involving real-time actuation or feedback, and benchmark aircraft models. These studies provide context for the simulation framework's design choices and boundary conditions.

2.3.1. Experimental Free-Flight Gust Testing

Several free-flight experiments have been conducted to study the aeroelastic response of flexible aircraft to gusts. Relevant platforms include the TU-Flex demonstrator with variable wing flexibility [27], the QT1 UAV with onboard strain sensors and model correlation using ASWING and NASTRAN [28], and the NLR 5-DOF free-free aircraft model used for gust load prediction [29]. Additional subscale aircraft have also been tested in controlled wind tunnel environments using embedded control and motion tracking systems [30–32].

2.3.2. Hybrid Simulation Approaches

Hybrid aeroelastic testing approaches combine numerical simulations with physical experiments to more accurately replicate flight conditions in a controlled environment. These methods are particularly relevant for flexible aircraft, where rigid-body motion and structural deformation are strongly coupled, and conventional clamped wind tunnel boundary conditions may not reproduce the actual aeroelastic behavior observed in free flight.

Gjerek et al. [33] developed a stiffness-adjustable aeroelastic test rig with automated impulse response characterization. Based on a 2-DOF aeroelastic section, shown in Figure 2.13, the system was controlled via LabVIEW and MATLAB to experimentally map static and dynamic stability boundaries. This versatile test bench would later serve as a platform for increased-fidelity hybrid testing.

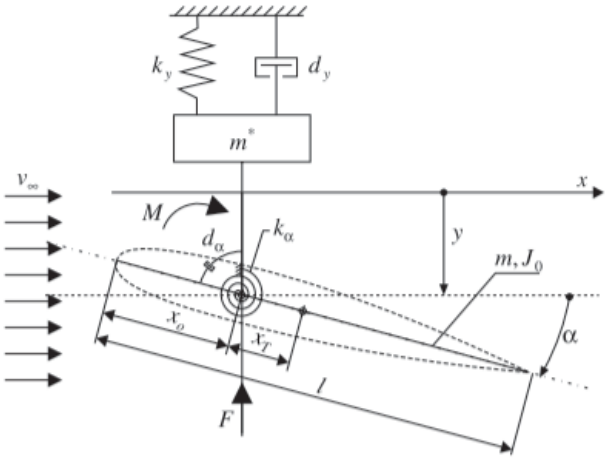

Figure 2.13: 2-DOF aeroelastic model [33]

Sodja and De Breuker [2] introduced a hybrid framework to increase wind tunnel experiments' fidelity for flexible aircraft configurations. Their methodology integrates the measured aerodynamic loads from a wind tunnel setup into a simulation environment that predicts the aircraft's free-flight motion. This motion is then used to control the movement of the wind tunnel model, thereby emulating realistic boundary conditions and flight dynamics. In addition to the feedback-based approach, Sodja and De Breuker proposed a simplified feedforward implementation. In this method, the free-flight response of the aircraft is first simulated using a high-fidelity aeroelastic solver, and the resulting motion profile is prescribed directly to the physical model in the wind tunnel. This eliminates the need for real-time feedback while still achieving high correlation with actual flight conditions, especially under gust excitation or when nonlinear aerodynamic effects are present. To validate this concept, the authors used SHARPy to simulate the free-flight response of a flexible HALE-type aircraft subjected to 1-Cosine vertical gusts. They then replicated the resulting heave-pitch motion in a wind tunnel using a modified version of Gjerek's aeroelastic apparatus [33], now equipped with actuators, illustrated in Figure 2.15. The study demonstrated strong agreement between the numerical and physical responses, confirming that the prescribed motion profile could reproduce free-flight dynamics with significantly greater fidelity than conventional clamped tests.

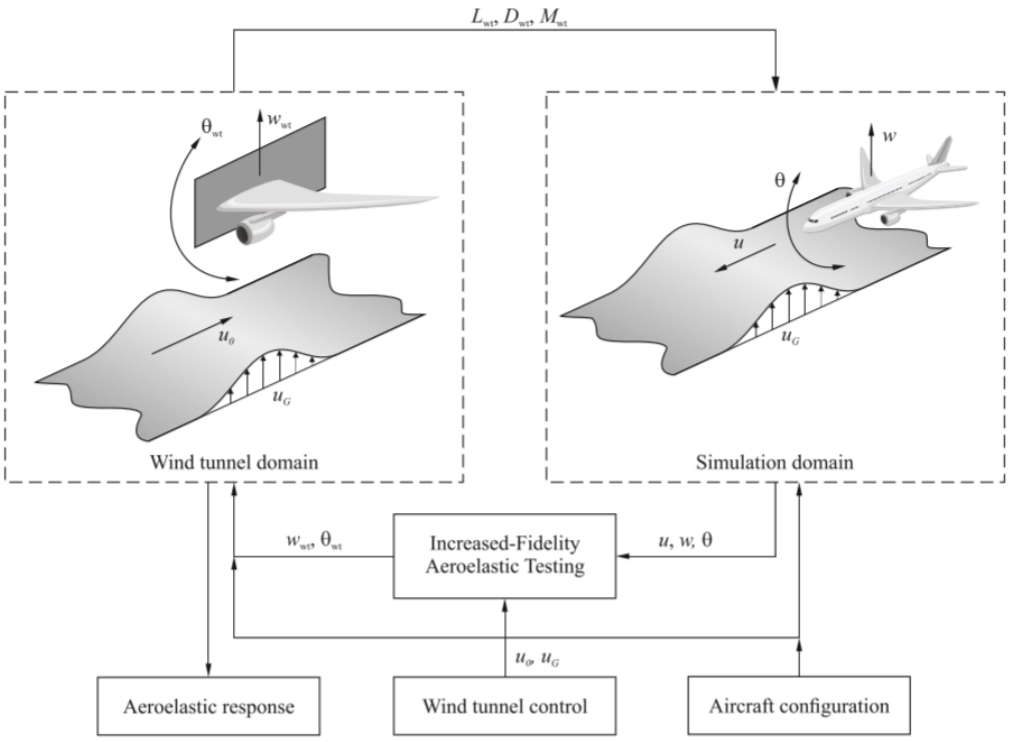

Figure 2.14: Increased-fidelity aeroelastic testing approach [2]

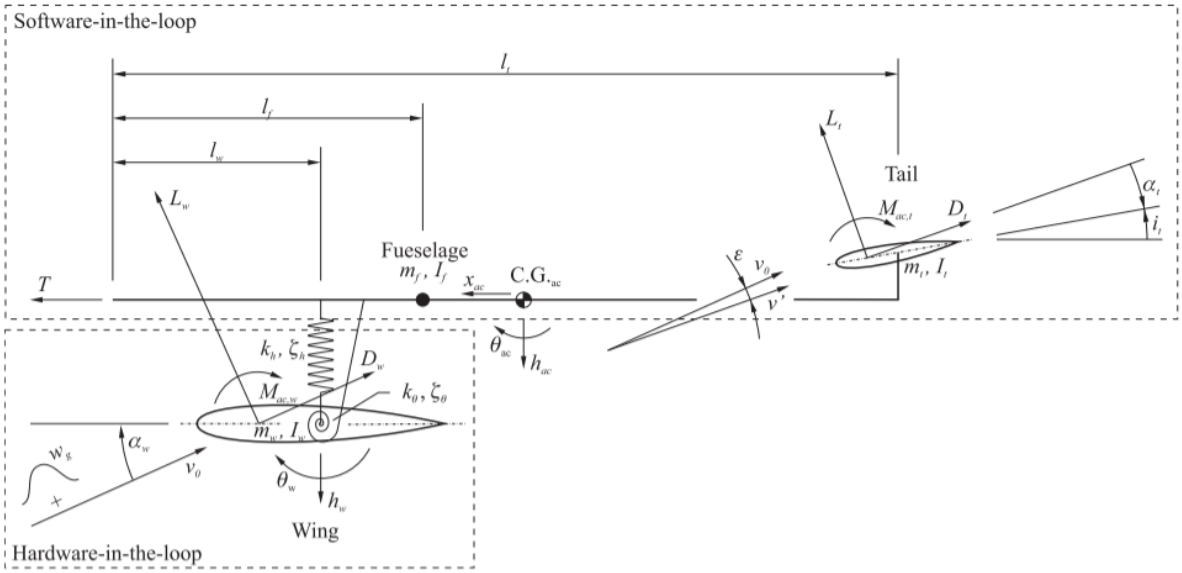

Figure 2.15: Sodja and De Breuker's aircraft model based on modified Gjerek's aeroelastic apparatus [2]

Other hybrid testing methodologies have also been developed to bridge simulation and experiment. Meng et al. [34] introduced a strain-based sensing framework for capturing structural deformations in a flexible wing subjected to gusts. A motion profile was extracted from experimental data and compared against nonlinear time-domain simulations using a strain-based beam model, showing strong amplitude and frequency response correlations. While at ONERA, Huvelin et al. [21] implemented a hybrid aeroelastic testing setup by combining a CFD-FEM simulation environment with wind tunnel testing of a scaled model. Their work integrated high-fidelity fluid simulations (URANS) with structural models to validate gust responses of an aeroelastic airfoil and complete aircraft using numerical and experimental data.

2.3.3. Benchmark Wing and Aircraft Models

A wide range of benchmark wings and flexible aircraft models have been developed to study nonlinear aeroelastic effects, gust response, and flight dynamics in experimental and numerical contexts. These models often feature high aspect ratio wings, tailored stiffness distributions, and carefully controlled boundary conditions, offering valuable insight into aeroelastic behavior under realistic loading environments. While the current thesis focuses solely on numerical simulations, the aircraft models reviewed here inspired the selection of representative geometric, structural, and material parameters during wing design. These benchmark aircraft and wing models provided rich case studies on structural design trade-offs, gust response dynamics, and simulation validation. As such, they indirectly informed the development and abstraction of the flexible wing model used in this thesis.

ONERA Aeroelastic Model Designed to replicate a 2-DOF aeroelastic system based on the OAT15A airfoil, this wind tunnel test model was developed to validate gust response using CFD-FEM simulations physically. It validated flow separation, pressure distribution, and time-domain response under controlled gust excitations [21].

Pazy Wing (Israel Aerospace Research Center) Designed for large, nonlinear deformations, the Pazy Wing features a NACA0018 airfoil with an aluminum spar, nylon-12 chassis, and polyester film skin. It was fabricated to study geometrically nonlinear deflections under wind tunnel conditions, with dual FE models in ANSYS and MSC NASTRAN. Experimental tests revealed limit-cycle oscillations and significant tip deformations, making this a canonical reference for high-flexibility designs [35].

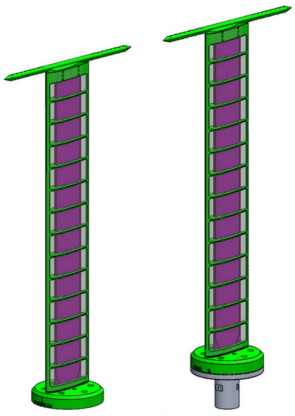

Figure 2.16: SOLIDWORKS model of the Pazy Wing [35]

Delft-Pazy Wing (TU Delft) A nearly identical version of the Pazy Wing developed at TU Delft, this model features slightly different material combinations and instrumentation layout. The primary difference from the benchmark Pazy wing lies in the reduced thickness of the aluminum spar plate in the Delft Pazy variant, which is 1.5 mm compared to 2.25 mm in the original design. This modification aims to achieve comparable large deformations at a lower wind tunnel speed. It is tailored for hybrid experimental setups involving SHARPy-driven motion and increased-fidelity aeroelastic testing. The Delf-Pazy Wing features a similar assembly of aluminium spar, nylon-12 chassis, and polyester film

skin. The design preserves the same fundamental geometry but allows integration with a rigid test rig or actuator platforms [36].

QT1 Aircraft (Bras et al.) The QT1 is a flexible, high aspect ratio UAV developed as part of a broader effort to assess in-flight aeroelastic behavior. The platform was equipped with strain sensors and subjected to ground vibration and flight testing. Structural models in ASWING and MSC NASTRAN were iteratively updated based on flight data to improve correlation with observed deformations and mode shapes. The study demonstrated the importance of in-flight measurements for validating numerical models and improving aeroelastic prediction accuracy [28]. Figure 2.17 presents a 3-view representation of the final design.

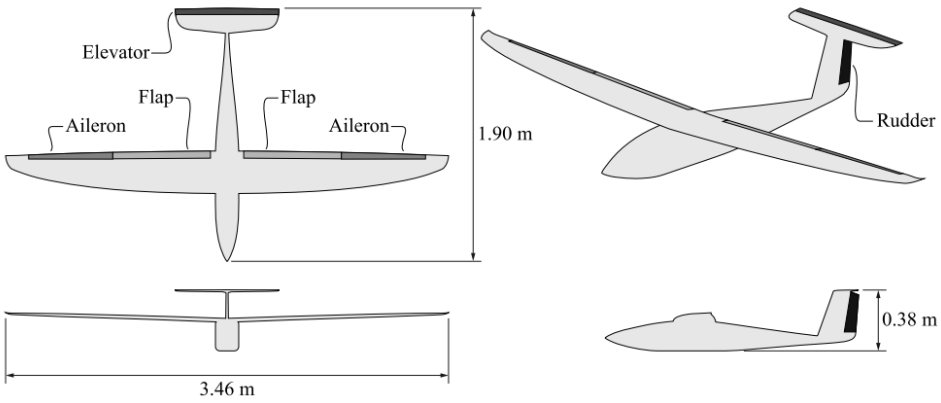

Figure 2.17: QT1 aircraft platform 3-view [28]

TU-Flex (DLR / TU Berlin) A modular demonstrator UAV to collect data on coupled flight and structural dynamics. TU-Flex was used in wind tunnel and simulation environments, featuring interchangeable wings with different flexibility classes (Flexible Aircraft and Very Flexible Aircraft). Gust response studies confirmed clear distinctions in dynamic behavior across the two configurations under controlled excitations [27].

HIRENASD Developed by DLR, the High REynolds Number Aero-Structural Dynamics (HIRENASD) model represents a transport aircraft wing with a supercritical airfoil. It was used extensively in CFD-FEM coupling studies and was a benchmark for transonic gust response and high-fidelity simulation validation. Its high stiffness-to-weight ratio and realistic aerodynamic layout offer a solid testbed for gust load prediction [37].

NLR 5-DOF Free-Free Model A conceptual aeroelastic testbed developed at NLR featuring two rigid-body and three flexible modes, illustrated in Figure 2.18, has been used to study load prediction under vertical gusts in free-flight simulations. The model captures key inertial and structural effects relevant to low-frequency aeroelastic modes and serves as a validation platform for reduced-order models [29].

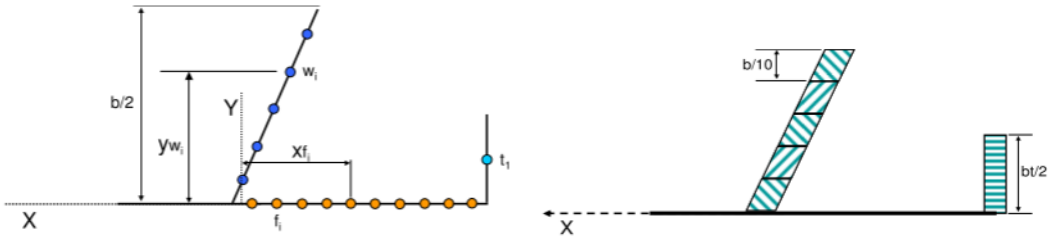

(a) Structural elements **(b)** Aerodynamic elements

Figure 2.18: NLR 5 DoF free-free aeroelastic model [38]

HALE Wing Models (Tang & Dowell; Patil & Hodges) These high-altitude, long-endurance wing structures were designed with slender planforms and low torsional stiffness. Tang's model employed balsa covering and steel spar flanges, while Patil and Hodges incorporated gravitational forces and extensive structural deflection modeling. These models were pivotal in validating nonlinear gust responses and rigid-body-like mode interactions [39, 40].

2.4. Research Gap

The literature reviewed in this chapter highlights significant progress in both computational and experimental methods for aeroelastic gust response analysis. Aerodynamic modeling techniques range from efficient, linearized solvers like DLM to high-fidelity CFD approaches. Structural solvers span from linear FEM-based representations to geometrically exact nonlinear beam formulations. Moreover, numerous aeroelastic frameworks, such as SHARPy, MSC NASTRAN, and NeoCASS, have enabled coupled simulations, each offering a trade-off between fidelity, computational cost, and applicability to nonlinear behavior.

Although experimental investigations of aeroelastic behavior using cantilevered wing models in wind tunnels are well-established, gust response testing under free-flight conditions remains limited. This is primarily because clamped or fixed boundary conditions do not accurately reflect the free-flight state of an aircraft wing, often resulting in overestimated root bending moments and tip deflections. A notable solution includes developing flight-test models to emulate free-flight conditions; however, replicating realistic free-flight dynamics within a wind tunnel presents a substantial challenge. Recent efforts have focused on developing flight-test models and hybrid simulation frameworks to bridge this gap.

Experimental studies have provided valuable insights into aeroelastic response, covering free-flight setups, hybrid simulation techniques, and benchmark model testing under realistic gust excitations. These efforts have been critical in validating computational models, capturing nonlinear structural effects, and exploring novel testing methodologies such as the feedforward framework by Sodja and De Breuker [2].

The work of Sodja and De Breuker [2] has demonstrated the feasibility of prescribing simulated free-flight responses to a wind-tunnel model, laying the foundation for increased-fidelity aeroelastic testing. Their proof-of-concept provided valuable insight into the potential of this approach, but relied on an idealized aircraft with a very high aspect ratio and extremely low flight speed. While effective for demonstrating the principle, such a configuration is not well-suited for practical wind tunnel testing, where size, speed, and control constraints must be considered.

Within this context, there remains a need for a dedicated aircraft model that is both experimentally feasible and capable of capturing representative aeroelastic effects. In particular, a structural model that combines sufficient fidelity with computational efficiency would enable real-time deployment in hybrid testing frameworks. This thesis contributes in that direction by delivering the design of a flexible aircraft model tailored for free-flight testing in TU Delft's Open Jet Facility. It also develops and validates its equivalent beam representation based on finite element analysis. The reduced-order beam model retains the structural fidelity required for aeroelastic simulations while remaining lightweight enough for integration into increased-fidelity testing workflows.

3

Design of a Flexible Aircraft Model for Aeroelastic Testing

Developing a flexible model aircraft is an essential step toward implementing the increased-fidelity aeroelastic test methodology proposed by Sodja and De Breuker [2]. This methodology relies on replicating the free-flight response of a flexible-wing aircraft using a motion platform in a wind tunnel environment. Before such a platform can be realized in hardware and software, it is essential first to characterize the motion envelope of a free-flying, gust-excited aircraft. To that end, a scaled flexible model is being developed specifically for free-flight aeroelastic wind tunnel testing. These flight tests will be conducted in the same wind tunnel intended for eventual platform integration, and the recorded dynamic response will serve multiple purposes:

- To define the range of motion that the motion platform must reproduce,
- To provide reference data for validating the numerical digital twin and control algorithms,
- To serve as an experimental testbed for future integration of sensors and morphing wing technologies.

The design of the model aircraft is a critical step in ensuring meaningful aeroelastic behavior during free-flight testing. The process is driven by initial requirements that balance geometric scaling, performance, and functionality to provide sufficient structural flexibility and gust sensitivity. Insights from literature on benchmark aircraft models, structural modeling approaches, and wind tunnel best practices inform the preliminary design choices. Key design parameters, including span, chord, stiffness, and mass estimates, are defined to capture the key coupled deformation modes, such as bending–torsion interactions, that characterize the aeroelastic response of flexible wings. These considerations form the basis for the later chapters' structural modeling and equivalent beam development.

3.1. Model Aircraft Requirements

An initial set of requirements was established to define the geometric, performance, and functional characteristics of the model aircraft, reflecting the physical constraints of the wind tunnel environment and outlining the design space within which it must operate effectively.

3.1.1. Dimensional Constraints

The experiments will be conducted in the Open Jet Facility (OJF) at Delft University of Technology, a low-subsonic, closed-circuit wind tunnel capable of generating flow speeds up to 35 m/s in a controlled environment. To ensure safe free-flight operation, the model must fit within the OJF's 2.85 m × 2.85 m octagonal test section. This constraint ensures that the model fits well within the test section, with enough clearance to avoid wall interference and boundary layer effects at the edges of the flow stream [41].

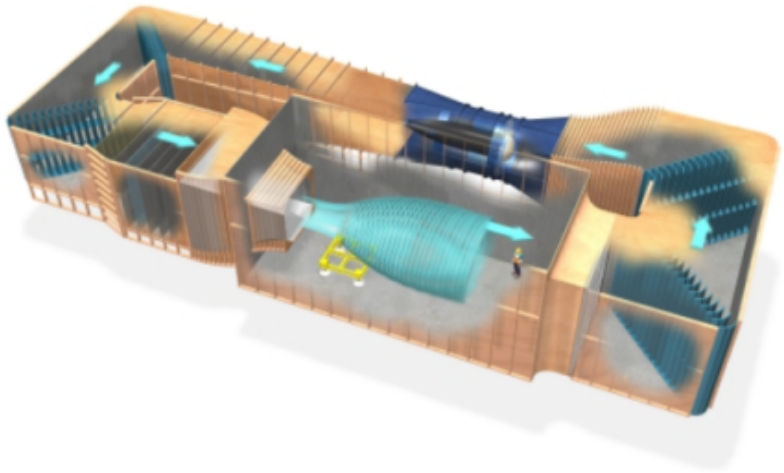

Figure 3.1: Schematic of Open Jet Facility [41]

3.1.2. Performance Requirements

As the aircraft is designed solely for free-flight testing within a wind tunnel environment, conventional performance parameters such as take-off, climb, or cruise are outside the scope of this study. Instead, the model emphasizes dynamic behavior, stability, and structural responsiveness to gust excitation. Furthermore, the aircraft must be capable of sustained flight at the freestream velocities achievable within the OJF, ensuring compatibility between aerodynamic performance and experimental conditions.

The maximum test speed is set at $V_{\text{max}} = 25$ m/s, which corresponds to the flow limit of the OJF when the gust generator is in operation. This upper bound defines the maximum aerodynamic excitation and structural response expected during gust experiments [42].

The stall speed is constrained to $V_s \leq 15$ m/s, based on preliminary estimates that balance mass budget, wing planform, and the aerodynamic characteristics of a NACA0018 airfoil, similar to the Delft-Pazy Wing [36]. This ensures the model operates within a practical angle-of-attack range and avoids post-stall behavior during wind tunnel tests. These performance limits provide clear operational boundaries for guiding the design process.

3.1.3. Modularity

The model must support modularity to facilitate rapid iteration and testing of different structural configurations. Specifically, it should allow exchangeable wing sections and adjustable center of gravity (CG) positions. This flexibility enables the evaluation of various stiffness distributions and stability characteristics while simplifying component replacement in the event of damage.

3.2. Flexible Aircraft Design Considerations

This section presents key insights from a focused literature review on individual design parameters relevant to the intended application of the flexible model aircraft. Many of these parameters, including planform, airfoil, and overall configuration, are selected in a heuristic manner guided by precedent studies rather than through performance optimization. The design prioritizes aeroelastic behavior over aerodynamic efficiency, intending to produce a model that reliably exhibits significant structural flexibility and gust sensitivity under wind tunnel conditions.

3.2.1. Wing

Configuration

The configuration of an aircraft refers to how its lifting surfaces are arranged relative to the fuselage. Low-, mid-, and high-wing configurations are the three main types of arrangements for a monoplane. The vertical positioning of the wing affects interference drag and longitudinal stability [43], as summa-

rized in Table 3.1. High-wing and mid-wing configurations are often preferred for their favorable stability characteristics. Since the scaled model is intended solely for free-flight testing inside the wind tunnel, conventional take-off and landing operations are not required. As a result, landing gear integration is unnecessary, and the associated drawbacks of high-wing configurations in accommodating gear placement can be disregarded. A high-wing layout also provides practical benefits, such as simplifying the adjustment of the wing's fore–aft position relative to the fuselage and enabling modular swapping of wing elements for testing. A high-wing configuration is therefore considered advantageous due to its inherent stability and ease of experimental integration.

	High Wing	**Mid Wing**	**Low Wing**
Interference Drag	average	low	high
Longitudinal Stability	stable	neutral	unstable
Landing Gear Integration	more difficult	moderate	easier

Table 3.1: Comparison of wing placement configurations

Airfoil

Airfoil selection significantly impacts aerodynamic performance, structural integration, and stall characteristics [44]. A review of prior studies suggests that symmetric, thick airfoils are often used in aeroelastic testing for their predictable stall behavior and space for internal systems. Among candidate airfoils, the NACA 0018 has demonstrated favorable nonlinear aeroelastic characteristics in flexible wing studies, particularly at high aspect ratios [45, 46]. It has also been used successfully in prior experimental studies such as the Delft-Pazy wing [36]. Based on these findings, the NACA 0018 could be a viable candidate airfoil for this model.

Angle of attack and Stall speed

The angle of attack (α) is the angle between the airfoil chord line and the freestream airflow. During steady flight, the lift generated is approximately linear with α until the stall angle is approached. To maintain predictable behavior, literature recommends that the trim α remain within the linear portion of the lift curve.

The stall speed, representing the minimum speed at which sufficient lift is generated to counteract weight [44], is given by:

$$V_s = \sqrt{\frac{2W}{\rho S_w C_{L_{max}}}} \tag{3.1}$$

where W is the weight of the aircraft, ρ is the density of air, S_w is the wing planform area and $C_{L,max}$ is the maximum coefficient of lift. This expression provides a useful constraint during preliminary sizing.

Aspect Ratio

The aspect ratio (AR) is a fundamental parameter influencing induced drag, structural characteristics, and gust sensitivity [44], and is calculated as:

$$AR = \frac{b^2}{S_w} \tag{3.2}$$

For a given wing planform area, the higher the AR, the more slender the wing. Table 3.2 below evaluates the impact of AR on various parameters [43].

	Large AR	**small AR**
Induced Drag C_{di}	small	large
Lift to Drag ratio L/D	large	smalll
Lift curve slope $C_{L,\alpha}$	large	small
Wing mass m_w	large	small
Span (constant wing area S$_w$) b	large	small

Table 3.2: Impact of wing aspect ratio

A higher AR reduces induced drag and increases aerodynamic efficiency, but it also amplifies gust response by making the wing more sensitive to changes in α. This behavior can be quantified using the following relations:

$$C_{di} = \frac{C_L^2}{\pi AR e} \tag{3.3}$$

$$\frac{L}{D}_{max} = K_{LD}\sqrt{\frac{AR}{S_{wet}/S_{ref}}} \tag{3.4}$$

$$C_{L,\alpha} = \frac{dC_L}{d\alpha} \tag{3.5}$$

where C_L is the coefficient of lift, L/D_{max} is the maximum lift to drag ratio, and e is the Oswald efficiency factor, which accounts for deviations from the ideal elliptical lift distribution (with $e = 1$ for a perfect ellipse, and $e < 1$ in practical cases). K_{LD} is an empirical constant used in Raymer's approximation [44] for estimating maximum lift-to-drag ratio in high-AR aircraft (typically $K_{LD} = 13$). The terms S_{ref} and S_{wet} are the reference and wetted areas, respectively, with S_{ref}/S_{wet} being constant. AR also influences the stalling angle such that low-AR wings will stall at a higher α than a high-AR wing due to reduced effective α at the wing tips [44].

It is observed that smaller wing loading results in more pronounced responses to vertical gusts, which can be expressed by the change in load factor (n) to angle of attack, given by [43]:

$$n_\alpha = \frac{dn}{d\alpha} = \frac{1}{m_w g}\frac{dL}{d\alpha} = \frac{\frac{1}{2}\rho V^2 C_{L,\alpha}}{g\frac{m_w}{S_{wet}}} \tag{3.6}$$

where g is acceleration due to gravity and V is the freestream velocity. These formulations suggest that a higher AR may enhance the model's sensitivity to gust-induced deformations, making it a favorable design feature.

Wing Sweep

Wing sweep is the angle between the quarter-chord line and a line perpendicular to the aircraft's longitudinal axis. It affects stall behavior, pitch-up moment, and aerodynamic efficiency. While sweep is beneficial at high subsonic or transonic speeds, it is generally not advantageous for low-speed flight. The table 3.3 below summarizes the effect of wing sweep angle (Λ) on various parameters given by [43], and Table 3.4 compares the effect of different types of wing sweep [43, 44].

		Large sweep	Small sweep
Critical Mach number		large	small
Maximum coefficient of lift	C_{Lmax}	small	large
Lift curve slope	$C_{L,\alpha}$	small	large
Flight in turbulent air		smooth	bumpy
Required angle of rotation		large	small
Wing mass	m_w	large	small

Table 3.3: General effects of wing sweep angle

	Forward sweep	No sweep	Aft Sweep
Risk of tip stall	none	none	large
Risk of pitch up	minor	none	large
Maximum lift coefficient C_{Lmax}	small	large	very small
Risk of one sided stall	minor	very minor	large
Risk of divergent wing deflection	yes	no	no
Wing mass m_w	very large	small	large
Longitudinal stability	unstable	neutral	stable

Table 3.4: Impact of wing sweep type

Figure 3.2 describes the stability boundaries to avoid pitch-up for various quarter-chord sweep and AR combinations of a wing, given by [44]. These values may limit the allowable AR to less than the estimated one. Given the target flight regime and the aim to elicit a clear gust response, a straight (zero-sweep) wing appears most appropriate.

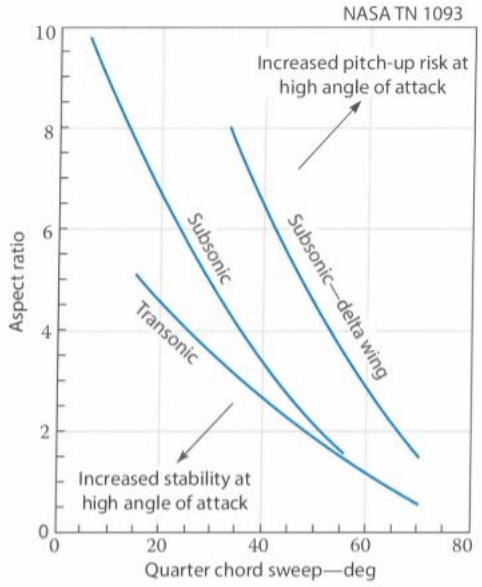

Figure 3.2: Effect of wing sweep and AR on wing-alone pitch up

Taper Ratio

Taper ratio (λ) of an aircraft wing is defined as the ratio between the wing tip chord (c_t) and the root chord (c_r) [44], written as:

$$\lambda = \frac{c_t}{c_r} \tag{3.7}$$

It controls the spanwise lift distribution and can influence stall behavior [43]. The flow separation from the wing first occurs when the distribution of lift coefficient (η) reaches its maximum along the span, which can be approximated by [43] as:

$$\text{Only for } \Lambda = 0, \quad C_{L,max} \text{ occurs at:} \quad \eta = \frac{y}{(b/2)} = 1 - \lambda \tag{3.8}$$

Where y is the distance along the span. Figure 3.3 from [43] shows the distribution of the lift coefficient along the wing span for various taper ratios for a non-swept wing with an aspect ratio of 10 and a coefficient of lift equal to 1.

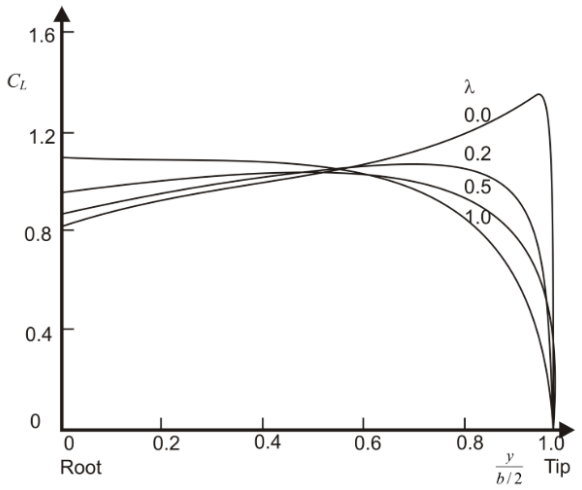

Figure 3.3: Distribution of coefficient of lift along the wing span for various taper ratios

A taper ratio below 0.2 may increase the risk of tip stall, as shown in Figure 3.3. A moderate taper ratio ($\lambda > 0.2$) is suggested to balance aerodynamic efficiency and stall control. Accordingly, a rectangular wing with $\lambda = 1$ is considered advantageous, as it provides geometric simplicity and stall characteristics that tend to develop more evenly along the span, making it suitable for wind tunnel free-flight testing.

Wing Twist

Wing twist (geometric twist) adjusts the local angle of attack along the span to improve stall progression and lift distribution [44]. However, excessive twist reduces efficiency outside its design point. Historical data recommend a twist ϵ_t of approximately $-3°$ to delay tip stall without degrading off-design performance. Since cruise optimization is not a significant concern, and to further reduce model complexity, minimal or no twist could be considered acceptable for this application.

3.2.2. Overall Planform

An appropriate planform layout is essential for capturing meaningful aeroelastic responses under gust excitation. Among the wide range of available configurations, only a few are compatible with the goals of modularity, ease of testing, and a pronounced aeroelastic response. Since conventional performance criteria such as take-off, climb, or cruise efficiency are not critical, the selection focuses on structural simplicity and configurability. Standard layout configurations considered in the literature include the Flying wing (FW), Blended wing body (BWB), and the conventional Tube and wing (TAW). Tables 3.5 and 3.6 list the significant trade-offs of FW and BWB configurations compared to the conventional TAW layout.

Advantages	Disadvantages
In cases of relatively low Mach numbers and high altitude flight, the FW outperforms TAW [47]	Requires larger engines [47]
Shows a better aerodynamic response than TAW [48]	Low-AR and the L/D is insensitive to it's AR [47]
FW has very low wing loading [48][49], less than half of TAW [48]	Only TAW configurations are capable of achieving high L/D values as a result of very high-AR, which leads to the reduction of C_{di} as a primary effect [47]
Despite its larger wing, the FW has significantly less S_{wet} than TAW due to the absence of a fuselage, tail, and nacelles, which also reduces empty weight and parasite drag [49]	Its uncommon wing architecture may imply manufacturing and maintenance problems [48]
Low wing loading in the FW, consequently, efficient trailing edge flaps lead to low-speed flights at a high α [49]	Issue of stability and controllability of the aircraft without an empennage [49]
	Slats need to be applied to the outboard wing to increase the V_s and to avoid uncontrollable pitch up during gusts or maneuvers [49]

Table 3.5: Comparison of FW trade-offs

Advantages	Disadvantages
Aerodynamically, BWB is a more promising alternative for conventional layout since it can achieve 20-24% gain in $L/$D, making it a high lift configuration due to its lifting body [49][50]	Low-AR [49]
The low wing loading gives BWB a better high-altitude buffet margin [49]	Given the same load volume, weight, and cruise Mach number as TAW and FW, the aircraft becomes inherently pitch-unstable when trim drag is minimized [49]
Increasing span is very effective from an aerodynamics point of view, which makes high-AR possible [49]	The low wing loading makes BWB more sensitive to gusts [49]
	The integrated structure makes the BWB significantly more complex than TAW [49]
	A greater span demands a higher thickness ratio and advanced composites to limit bending loads, but these materials may produce wings too rigid for meaningful gust response [49].

Table 3.6: Comparison of BWB trade-offs

Given these trade-offs, a conventional tube-and-wing layout appears to be a suitable candidate for this application. Its inherent stability, modular design potential, and compatibility with existing analysis tools support this recommendation [44].

3.2.3. Static Stability and Tail sizing

Longitudinal static stability depends on the location of the aircraft's CG relative to the neutral point, the aft-most position of the CG at which the aircraft remains neutrally stable in pitch. The horizontal tailplane generates restorative moments to counter pitch disturbances and maintain trim. This relationship is described by:

$$M = L_w x_g - (l_t - x_g) L_t \tag{3.9}$$

where M is the net pitching moment, x_g is the distance from the wing aerodynamic center (AC) to the CG, L_w is the lift force produced by the wing, L_t is the lift force produced by the horizontal tail, and l_t is the distance from the wing AC to the tail AC. The CG should be positioned ahead of the neutral point to ensure a positive static margin, defined as the distance between the CG and neutral point normalized

by the mean aerodynamic chord (c). Additionally, horizontal tails with lower aspect ratios tend to stall later than the wing, preserving pitch control authority during post-stall conditions. These considerations motivate the use of a horizontal tail with moderate surface area and sufficient moment arm to achieve stable trim. Figure 3.4 illustrates a statically trimmed aircraft in level flight.

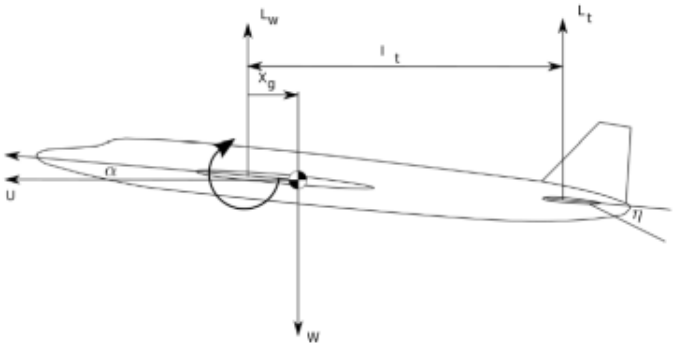

Figure 3.4: Aircraft in level flight [51]

Raymer [44] further recommends selecting the tail moment arm such that the horizontal and vertical tail volumes meet minimum effectiveness criteria, such as maintaining horizontal tail volume coefficient (V_h) in the range $\approx 0.5 - 1.0$ and vertical tail volume coefficient (V_v) in the range $\approx 0.02 - 0.05$, that help to ensure sufficient pitch and yaw stability control authority. These are defined as:

$$V_h = \frac{l_h S_h}{c S_w}, \quad V_v = \frac{l_v S_v}{b S_w} \tag{3.10}$$

where l_h and l_v denote the distances from the CG to the ACs of the horizontal and vertical tails, respectively, and S_h and S_v are their corresponding planform areas.

3.2.4. Propeller Effects

Inclusion of a propeller introduces additional aerodynamic and inertial complexities, such as slipstream-induced lift variation and gyroscopic torques [52]. These effects are particularly relevant in the context of a flexible-wing platform. Literature indicates that these interactions are non-negligible and may degrade the accuracy of rigid-body approximations. However, they can be challenging to predict, as seen in [53].

Recent work by [54] provides a framework for examining the interactions between lifting surfaces and propellers and the impact of propeller aerodynamics and inertial effects on the response of highly flexible aircraft. Semi-analytical methods and experimental data, such as motor revolutions-per-minute, can estimate propeller-induced forces and moments [55, 56]. Based on these findings, employing an electric propeller is a practical choice for simplicity, with slipstream and inertial effects accounted for through analytical or empirical corrections. The thrust required can be expressed using [44]:

$$T = D = \frac{1}{2}\rho V^2 C_D S_w \tag{3.11}$$

here, T is the thrust required and C_D coefficient of drag.

3.3. Preliminary Design Parameters

Based on the design objectives and considerations discussed in the preceding sections, this section finalizes the preliminary configuration of the flexible aircraft model. The goal is to achieve a statically stable, modular platform that exhibits pronounced aeroelastic response under gust excitation during wind tunnel free-flight tests.

To this end, the aircraft model follows a conventional tube-and-wing configuration. Its primary structure consists of a carbon fiber tube frame, onto which the batteries, propulsion and control electronics, and

all lifting surfaces are mounted. This provides a lightweight yet rigid baseline while supporting modular component integration.

3.3.1. Geometric and Stability Parameters

Table 3.7 presents the selected geometric parameters for the wing, horizontal, and vertical tail. These values were derived using methods from Raymer [44], with adaptations suited to the specific aeroelastic objectives of this flexible model.

Parameter	Wing		Horizontal tail		Vertical tail		Unit
Span	b	1500	b_h	500	b_v	200	mm
Root chord	c	200	$c_{r,h}$	150	$c_{r,v}$	150	mm
Aspect Ratio	AR	7.5	AR_h	5	AR_v	2	–
Sweep	Λ	0	Λ_h	16.7	Λ_v	20.6	deg
Taper ratio	λ	1	λ_h	0.5	λ_v	0.5	–
Tail arm	–	–	l_h	750	l_v	800	mm
Tail volume coefficient	–	–	V_h	0.7	V_v	0.04	–

Table 3.7: Scaled model aircraft parameters

The wing has a span of 1500 mm and a chord of 200 mm, giving an aspect ratio of 7.5, which increases gust sensitivity while remaining structurally feasible. A NACA 0018 airfoil is used, with prior studies showing suitable nonlinear aeroelastic behavior. The expected operating range is between angles of attack of about $2°$–$6°$ at speeds of 15–25 m/s. The wing has no sweep or taper, simplifying construction and avoiding pitch-up or unexpected stall effects. The horizontal and vertical tails provide volume coefficients of 0.7 and 0.04, consistent with standard design guidelines, ensuring trim control and yaw stability in gusts. Both tails have moderate sweep and taper to balance aerodynamic effectiveness with simple construction and predictable behavior.

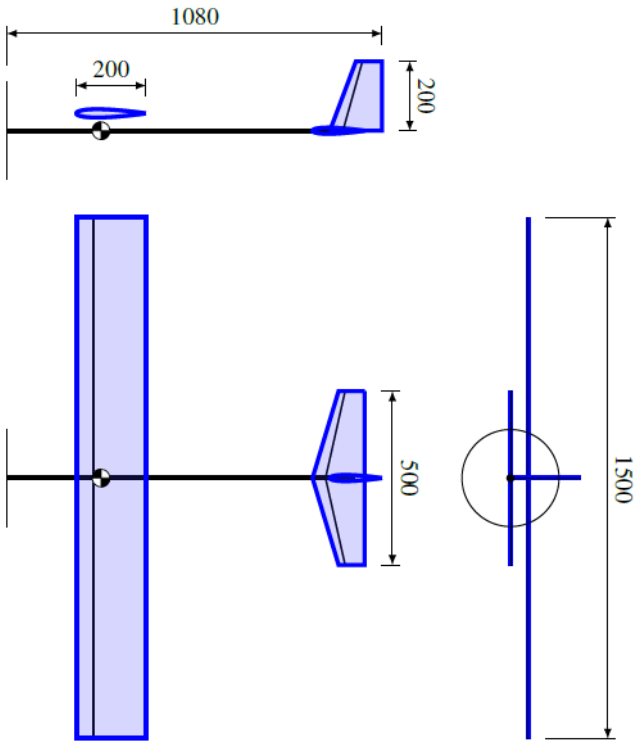

Figure 3.5: Schematic overview of the scaled model aircraft

3.3.2. Mass Distribution and CG Estimation

Table 3.8 summarizes the component-level mass budget and longitudinal positions. These values were used to compute the initial center of gravity, located at $x_{\text{CG}} = 271$ mm from the nose. The battery pack and wing mount are longitudinally adjustable, enabling targeted shifts in CG to explore stability effects or emulate different configurations.

Component	**Mass** (kg)	**Location** (mm)	**Notes**
Motor + prop	0.12	27	T-Motor AS2814, APC 11×5.5 prop
Batteries	0.451	400	5Ah, for motor
	0.063	400	For electronics
Servos	0.016	250	Wing
	0.016	1000	Tail
Microcontroller	0.036	200	BeagleBone Blue
ESC	0.043	200	YEP ESC 40A
Wing	2.0	250	
Horizontal tail	0.01	1000	
Vertical tail	0.05	1050	

Table 3.8: Estimated mass budget and location of components

This modular internal layout facilitates future experimentation with different wing stiffnesses, such as using the Delft-Pazy wing or tailored composite variants, without requiring fuselage redesign. The preliminary design presented in this section defines the baseline configuration for the model aircraft, integrating aerodynamic, stability, and modularity considerations. These parameters are inputs to the next part, where the structural model is developed.

3.4. 3D Model Definition

The 3D model of the aircraft's half-wing was created in CATIA V5 using the 3DExperience platform. It consists of several geometrically detailed components that collectively form the wing's structural and aerodynamic architecture, which include the wing chassis, spar, and aileron, along with auxiliary parts for actuation and instrumentation. Figure 3.6c provides a complete overview of all components.

The model is oriented in a global Cartesian coordinate system, with the origin $(0, 0, 0)$ located at the center of the root face of the spar. The X-axis is aligned with the chordwise direction, the Y-axis spans outward along the semi-span from root to tip, and the Z-axis points vertically upward, normal to the wing surface as seen in Figure 3.6b. This coordinate system is adopted consistently throughout the structural modeling process.

The wing features a rectangular planform with a half-span of 0.75 m and a constant chord of 0.2 m. A continuous metallic spar runs spanwise from root to tip and is the primary load-carrying element, as depicted in Figure 3.6a. The assembly comprises two distinct materials: a metallic spar and a three-dimensional (3D) printed thermoplastic chassis. Material assignments and their mechanical properties are detailed in the following chapter. Figure 3.6 presents multiple views of the half-wing assembly, including top, cross-sectional, and exploded perspectives, with each subcomponent color-coded for visual clarity.

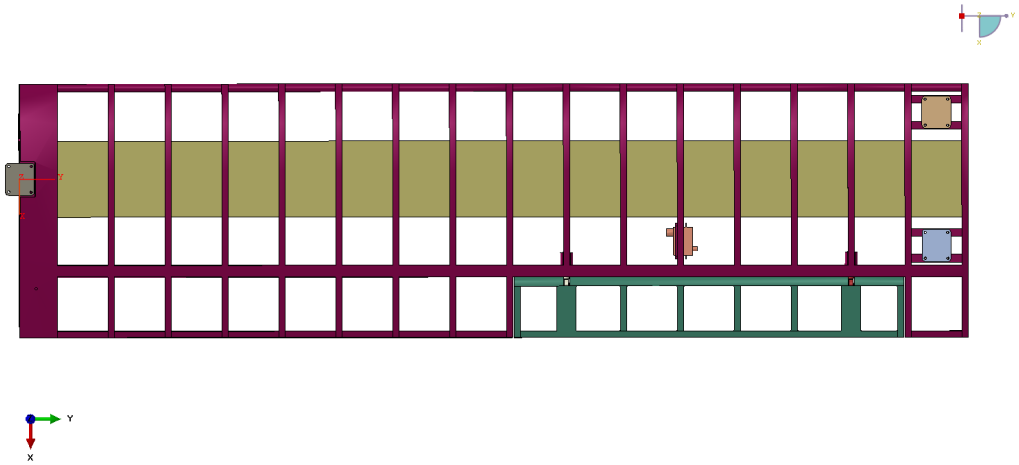

(a) Top view of the wing assembly

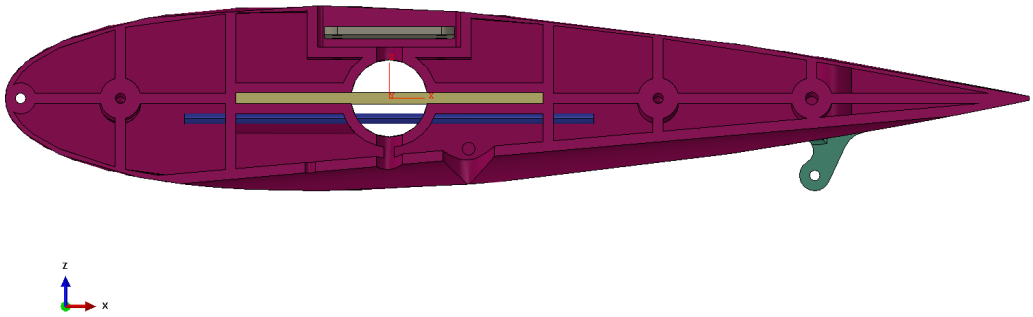

(b) Cross-sectional view at the root showing spar placement

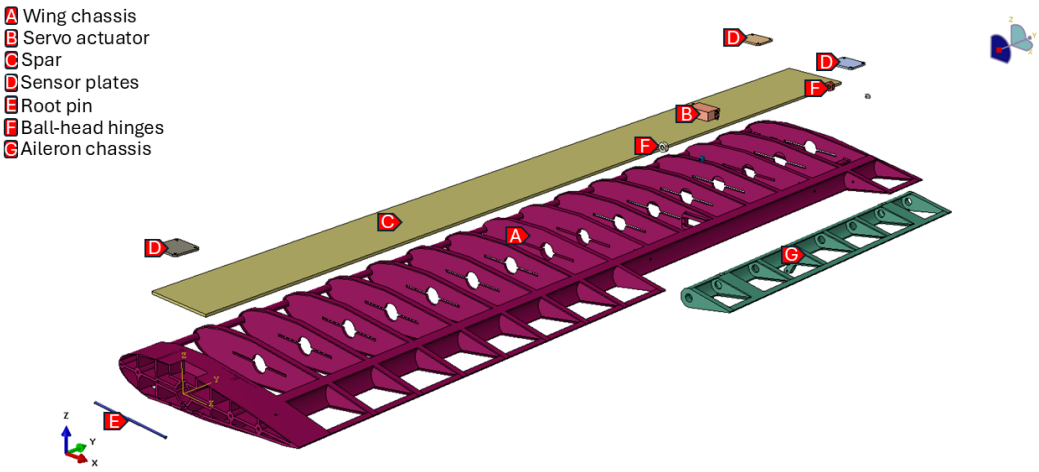

(c) Exploded view of the halfspan

Figure 3.6: Detailed views of the 3D wing assembly

4

Structural Modeling

The hybrid testing methodology introduced by Sodja and De Breuker [2] employs free-flight wind tunnel tests of a flexible, scaled aircraft as a validation step. This allows a direct comparison between the full free-flight response of the aircraft and the response of a wing mounted on a motion platform driven by numerically prescribed profiles. Within this context, the present chapter focuses on developing the aircraft's digital twin from a structural perspective.

The chapter begins with the finite element model developed in ANSYS R2 2023, where linear static and modal analyses are performed to characterize the wing's deformation behavior and natural frequencies. Sensitivity studies are included to confirm the reliability of the extracted stiffness properties. These results are then used to construct a reduced-order equivalent beam model that reflects the main structural properties of the 3D wing while being computationally efficient and directly compatible with SHARPy's beam formulation. Finally, the correspondence between the finite element results and the reduced beam model is assessed, establishing confidence in the simplified representation as the basis for subsequent aeroelastic studies.

4.1. Model Simplification

The original aircraft half-wing was designed as a full assembly in CATIA V5. The assembly included numerous functional components that produced a high level of detail, as seen in Figure 3.6c. While these details are essential for manufacturing and mechanical design, they pose significant challenges for structural finite element modeling due to mesh generation difficulties and the minimal contribution of many features to global stiffness.

To facilitate efficient and stable FEM simulation, the 3D model was imported into ANSYS SpaceClaim 2023 R2. The non-structural features were systematically removed, retaining only the primary load-carrying elements critical to global stiffness representation. The simplified model consists solely of the wing chassis and internal spar, as shown in Figure 4.1.

Importantly, all major internal ribs and web structures were retained. These features are crucial in distributing shear and bending loads and significantly affect torsional and out-of-plane stiffness. Their inclusion ensures that the simplified model retains the necessary structural fidelity for linear static and modal analyses.

Table 4.1 overviews the removed features, their engineering rationale, and the modeling treatment applied. This abstraction significantly improved mesh quality, reduced element count, and eliminated artificial stress concentrations, establishing a simplified yet dynamically representative model composed of the wing chassis and spar.

Removed Feature	Reason for Removal	Treatment If Needed	Location
Servo actuator	Not a structural load path; meshing it adds complexity	Modeled as a point mass	On a rib, close to aileron
Sensor plates	Small and localized stiffness; unnecessary in global response analysis	Modeled as point masses	Near tip, inside chassis
Holes, fillets, slots	Cause local stress raisers and poor mesh quality	Removed	Throughout structure
Aileron	Not needed unless hinge moments are modeled	Modeled as point masses	Trailing edge
Hinges	Small, nonlinear contacts, not load-bearing	Removed	Wing-aileron web
Root pin	No contribution to stiffness since the root dominates	Removed	Root cavity, below spar

Table 4.1: Overview of the removed features and their justification

These components either contributed negligibly to stiffness or were more effectively modeled as concentrated masses in subsequent dynamic analyses. This strategy preserved their inertial effects without burdening the mesh with excessive geometric complexity.

This simplification yielded a reduced yet representative model composed of the wing chassis and internal spar. With the simplified geometry established, the next step involves defining the numerical model setup and boundary conditions required for static and modal analysis.

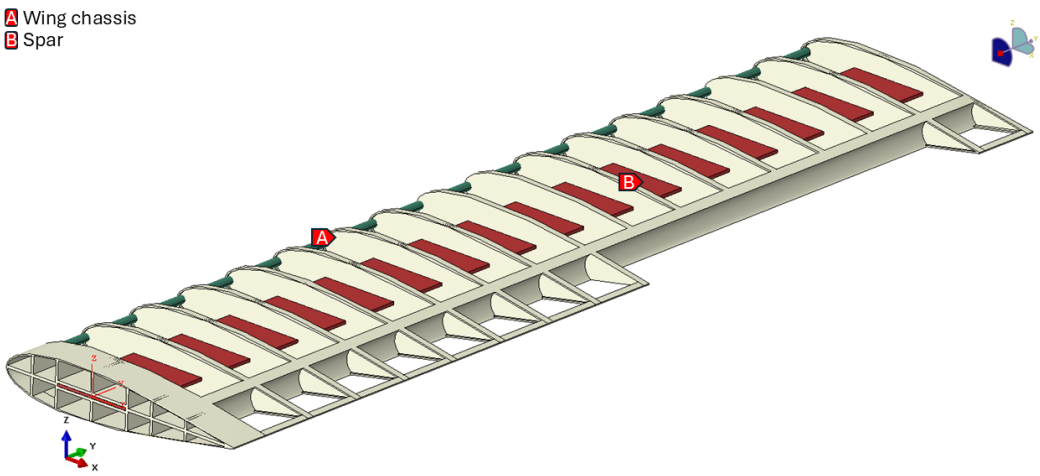

Figure 4.1: Simplified 3D wing isometric view

4.2. Finite Element Analyses Setup

With the 3D wing geometry finalized, the finite element model was constructed in ANSYS Workbench 2023 R2. This section describes the finite element modeling approach to analyze the simplified wing structure. The key aspects covered are material property assignment, element types, meshing strategy, boundary conditions, applied loads, the simulation parameters, and the core assumptions used in linear static and modal analyses.

4.2.1. Material parameters

The two components retained, the spar and the half-wing chassis, were given specific material properties corresponding to the materials intended for their fabrication. Aligned with the manufacturing approach adopted for the Delft-Pazy wing, the wing chassis is modeled using 3D-printed Nylon 12, while aluminum (7075-T6) is used for the internal spar. The material parameters used in the FEM simulations are summarized in Table 4.2, with values obtained from relevant literature sources [35, 57, 58]. These properties ensure that the structural model accurately represents both stiffness and mass contributions.

Material Parameters	Unit	Aluminum 7075-T6	Nylon 12 3D Printed
Density	Kg/m^3	2795	930
Young's modulus	Pa	7.1e+10	1.7e+9
Poisson's Ratio		0.33	0.394
Bulk Modulus	Pa	6.9608e+10	2.673e+9
Shear Modulus	Pa	2.6692e+10	6.0976e+8
Compressive Yield Strength	Pa	4.68e+8	4.8e+7
Tensile Ultimate Strength	Pa	5.3e+8	5.1e+7
Tensile Yield Strength	Pa	4.68e+8	4.8e+7
Part		Spar	Wing chassis

Table 4.2: Material properties assigned and used in the FEM simulations

4.2.2. Contact Definitions and Boundary Conditions

To simulate the interaction between the wing spar and the surrounding chassis, a `Bonded Contact` interface was defined, which enforces a no-separation and no-slip condition between the two surfaces, effectively constraining them to deform together without relative motion. While such perfectly bonded conditions do not precisely represent physical interactions due to surface roughness, play, or adhesive imperfections, they serve as a practical approximation in finite element analysis commonly used to model welded joints, adhesive layers, or tightly fastened connections [59]. In this case, the bonded contact approximates the integrated behavior of the spar embedded within the 3D-printed wing structure, while also allowing the problem to remain linear since the contact area does not change during loading, and small imperfections (gaps or penetrations) are ignored.

The wing was modeled as a cantilever beam by applying a `Fixed Support` boundary condition to the entire root face of the structure, including both the spar and the wing chassis root faces as seen in Figure 4.2. This constraint fixes all translational and rotational degrees of freedom, replicating a rigid mounting of the wing at the root. This `Fixed Support` boundary condition was utilized for static and modal analyses.

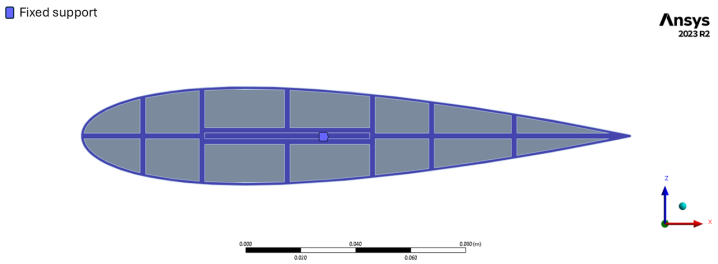

Figure 4.2: Fixed support boundary condition at the wing root

4.2.3. Meshing Strategy

The finite element model of the simplified wing structure employed second-order solid elements to capture 3D deformation, curvature, and stress fields accurately. ANSYS Mechanical automatically generated two element types during meshing: `SOLID186` and `SOLID187`.

- `SOLID186` is a 20-node hexahedral (or prism) element with three translational DOFs per node. It offers quadratic displacement behavior and is ideal for structured regions with regular geometry. The rectangular aluminum spar, being prismatic, was meshed using 1,800 `SOLID186` elements due to its regular shape.
- `SOLID187` is a 10-node quadratic tetrahedral element with three translational DOFs per node. It is optimized for automatically meshing irregular, curved, or complex geometries. The wing chassis, which includes internal webs, rounded edges, and stiffening structures, was meshed using 54,573 `SOLID187` elements.

Both element types are compatible with large deformation physics, bonded contact interfaces, and modal analysis, making them suitable for this phase's static and dynamic evaluations. The default element size was 5 mm, balancing fidelity with computational efficiency. The final mesh of the abstracted wing consisted of 56373 solid elements and 125827 nodes, with the majority being quadratic tetrahedral elements `SOLID187`. Figure 4.3 below depicts the meshed bodies.

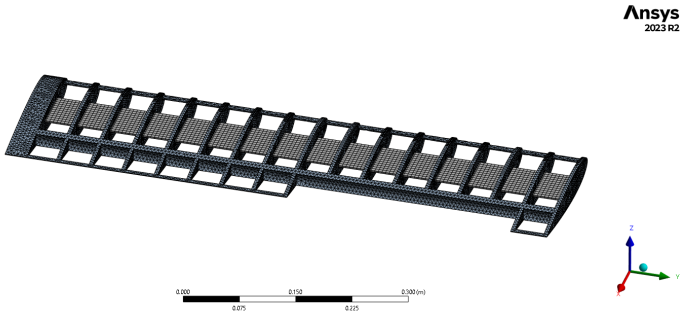

(a) Meshed wing

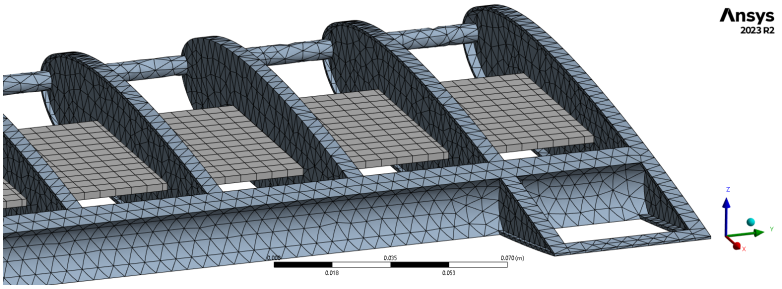

(b) Zoomed-in image of the wing mesh

Figure 4.3: 3D wing mesh

4.2.4. Point-Mass Allocation

To preserve the inertial effects of abstracted components, point masses were introduced in the FEM model, represented by `MASS21` elements. The calculations for mass distributions and CG coordinates are in the Appendix A.2. These represent non-structural elements excluded from the mesh while ensuring realistic mass distribution and dynamic response. Table 4.3 summarizes the implementation of the servo actuator, aileron, and sensor plates as point masses.

Component	Scoping / Location	**Mass** [kg]	Attachment / Behavior
Servo	Single node at rib (CG position)	0.008	Direct, rigid
Aileron	Six nodes (one per rib thickness center) with remote points at CGs	6 × 0.00367	Remote, deformable (MPC) with all 6 DOFs active
Sensor plates	Two nodes per plate (one per rib face) with remote points at CGs	2 × 0.00183	Remote, deformable (MPC) with all 6 DOFs active

Table 4.3: Overview of point-mass allocation in the FEM model

Figure 4.4 shows the placement of point masses on the wing. The modeling distinguishes between rigid and deformable attachments: the servo actuator is rigidly connected, avoiding artificial compliance similar to RBE2 elements, while the aileron and sensor plates are attached through deformable remote points, analogous to RBE3 behavior, to preserve local flexibility without over-constraining the structure. Multiple Point Constraint (MPC) coupling was used between the remote point and the selected node set, ensuring a linear formulation. This setup consistently represents inertial effects in static and modal analyses.

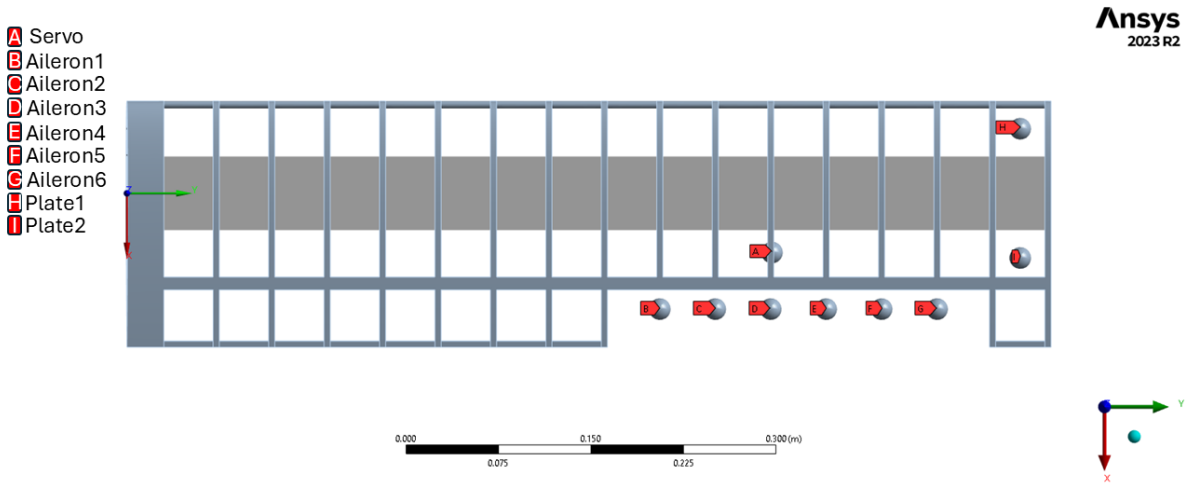

Figure 4.4: Placement of modeled point masses on the wing structure

4.2.5. Derivation of Beam-Equivalent Spanwise Responses

To enable spanwise translational deformation analysis in static and modal simulations, a set of nodes was identified along the elastic axis of the wing spar. Since the solid spar model contains no interior nodes, direct extraction along the spar centerline was not feasible. Instead, an equivalent line of nodes (`BeamNodes`) was defined on the spar surface to approximate displacements along the elastic axis.

For torsional analysis, two additional node sets were created at the leading and trailing edges of the spar (`spar_LE` and `spar_TE`), providing a consistent basis to calculate twist along the span. These definitions ensured that the spanwise locations were aligned with the global Y-axis from root to tip, with uniform spacing and free of irregular mesh artifacts.

These node sets were consistently used across static simulations to derive spanwise stiffness distributions and modal analyses to extract displacement and twist mode shapes. The resulting spanwise resolution of 5 mm would enable high-fidelity comparisons with the equivalent beam model. The detailed conditions and methodology for node identification are provided in Appendix A.3. Figure 4.5 illustrates the location of these node sets on the 3D wing model.

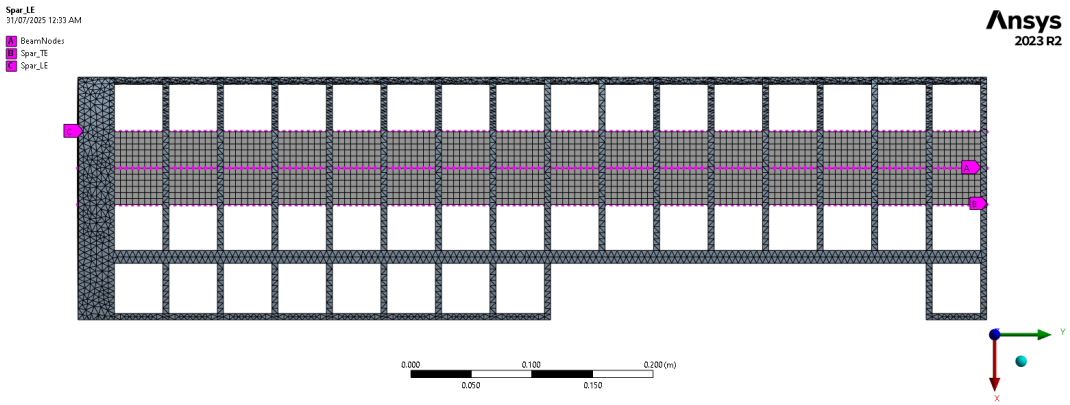

Figure 4.5: Visualization of the `BeamNodes`, `spar_LE`, and `spar_TE` named selections on the 3D wing model

4.2.6. Modeling Assumptions

The structural finite element simulations conducted in ANSYS for static stiffness extraction and modal analysis were based on standard assumptions that simplify material behavior and structural response.

All materials were modeled using linear elastic constitutive laws, assuming a direct proportionality between stress and strain within the elastic range. This governed the force–displacement relationship under unit moment loading in static simulations. At the same time, modal analysis ensured that natural frequencies and mode shapes were extracted from a constant stiffness matrix.

The aluminum spar and the Nylon12 chassis were treated as isotropic materials with constant values for Young's modulus and Poisson's ratio. Although Nylon12 can exhibit mild anisotropy depending on the 3D-printing orientation, this effect was neglected to maintain consistency with beam theory simplifications and to reduce modeling complexity.

All simulations were conducted under the small deformation assumption, meaning that strains and rotations were considered sufficiently small such that geometric nonlinearities were not included. This assumption validates the unit moment loading applied in static tests and the infinitesimal displacements assumed in eigenvalue-based modal analysis.

The wing structure was represented as a merged solid consisting of the Nylon12 chassis and the embedded aluminum spar, with perfect bonding at the interface. No interfacial compliance, slippage, or delamination was modeled, allowing the structure to behave as a unified volume during static and dynamic analyses.

4.3. Modal Analysis of Wing

A modal analysis of the 3D wing was conducted to determine its undamped natural frequencies and mode shapes, providing the reference structural dynamics for constructing and validating the equivalent beam model. The simulation setup, including material definitions, meshing, contacts, point masses, and cantilevered boundary conditions, was identical to that described in Section 4.2, using eigenvalue extraction. Figure 4.6 illustrates the modal analysis simulation setup.

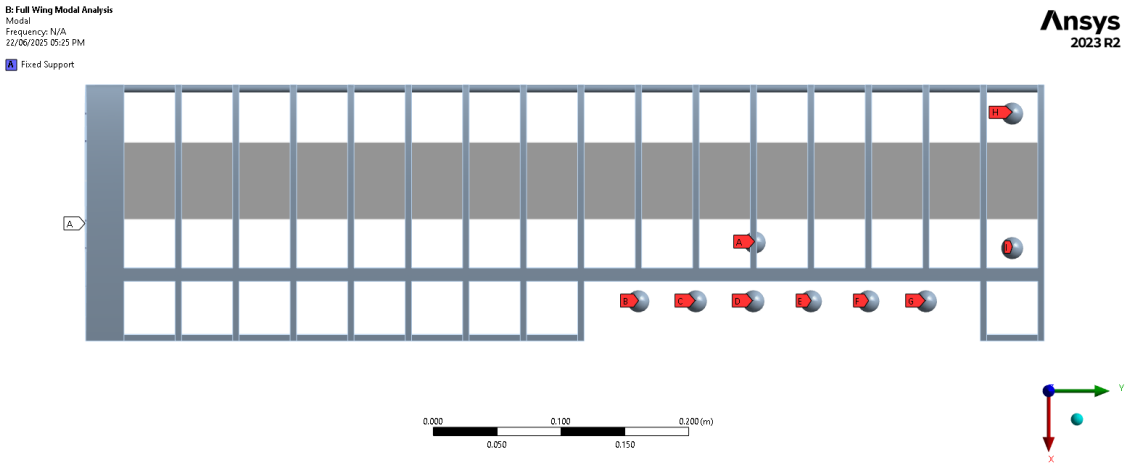

Figure 4.6: 3D wing modal analysis

In addition to the natural frequencies, the wing's global mass and inertia properties were extracted from the `Solution Information` summary, including the total mass, center of mass location, and full 3×3 rotational inertia tensor about the center of gravity. ANSYS also provided the modal effective mass for each mode in all six degrees of freedom. The mode shape data were further post-processed to extract spanwise displacement and twist distributions along the elastic axis, enabling direct comparison with the equivalent beam model.

4.3.1. Modal Response and Shape Visualizations

Table 4.4 summarizes the 3D wing structure's first five natural frequencies from the lowest in increasing order.

Mode Number	Frequency [Hz]
1	4.24
2	21.98
3	35.84
4	59.59
5	63.14

Table 4.4: First five natural frequencies of the 3D wing system

To characterize the deformation patterns of each mode, the translational and torsional deformation components were extracted along the span. Specifically, u_x denotes the in-plane displacement, u_z the vertical displacement, and θ_y the twist. The angular displacement or twist was estimated using the small-angle approximation as the difference in vertical displacement between the leading and trailing edge nodes along the span:

$$tan(\theta_y(y)) \approx \theta_y(y) = \frac{u_z^{LE}(y) - u_z^{TE}(y)}{\Delta x} \quad \text{with} \quad \Delta x = 0.060\,\text{m} \tag{4.1}$$

where Δx is the constant chordwise distance between sampling nodes at each spanwise location. u_z^{LE} and u_z^{TE} are the leading and trailing edge vertical displacements respectively. Spanwise displacement datasets for each mode are provided in Appendix A.4, Tables A.1–A.5.

To interpret the deformation data consistently across modes, the effective modal mass values reported by ANSYS were used to identify the dominant deformation direction and scale the relative amplitudes of the displacement components. Due to the modal analysis's mathematical nature, the deformations' absolute values are not physically meaningful since the shape vectors are determined only up to a scalar constant. The magnitude of u_x, u_z, or θ_y in any mode shape has no real-world amplitude interpretation. However, each deformation component's relative shape along the span carries physical meaning. Each deformation component was multiplied by its effective modal mass ratio m_{eff}/m_w, ensuring that the plotted amplitudes reflected the true relative participation of u_x, u_z, and θ_y in each mode. The corresponding effective modal mass data are provided in Appendix A.5.

For instance, in Mode 1, the effective mass contributions are concentrated in the Z direction, with negligible participation in X and $ROTY$:

$$X : \frac{m_{\text{eff}}}{m_w} \approx 0.00\% \quad Z : \frac{m_{\text{eff}}}{m_w} \approx 61.62\% \quad ROTY : \frac{m_{\text{eff}}}{m_w} \approx 0.43\% \tag{4.2}$$

This confirms that Mode 1 corresponds to the first out-of-plane bending shape. Repeating this procedure for the first five modes yields the classification summarized in Table 4.5, highlighting each case's dominant direction of deformation.

Mode Number	Z[%]	X[%]	ROTY[%]	Mode Type
1	**61.622**	0.000	0.428	Out-of-plane Bending
2	**15.006**	0.000	0.088	2^{nd} Bending
3	0.007	0.012	**0.132**	Torsion
4	**5.325**	0.013	0.034	3^{rd} Bending
5	0.001	**61.235**	0.000	In-plane bending

Table 4.5: Classification of modes based on dominant effective mass contribution

As an example of the scaling, the factors applied to Mode 1 were:

$$\gamma_X = \frac{m_{\text{eff},X}}{m_w} = \frac{0.733106E-09}{0.58870} = 1.245E-09 \tag{4.3}$$

$$\gamma_Z = \frac{m_{\text{eff},Z}}{m_w} = \frac{0.362771}{0.58870} = 0.6162 \tag{4.4}$$

$$\gamma_{ROTY} = \frac{m_{\text{eff},ROTY}}{m_w} = \frac{0.251933E-02}{0.58870} = 4.279E-03 \tag{4.5}$$

The same procedure was applied to modes 1–5, and the resulting deformations along the span are visualized in Figure 4.7. Additionally, the scaled DOFs of each mode were used to assemble the modal vectors.

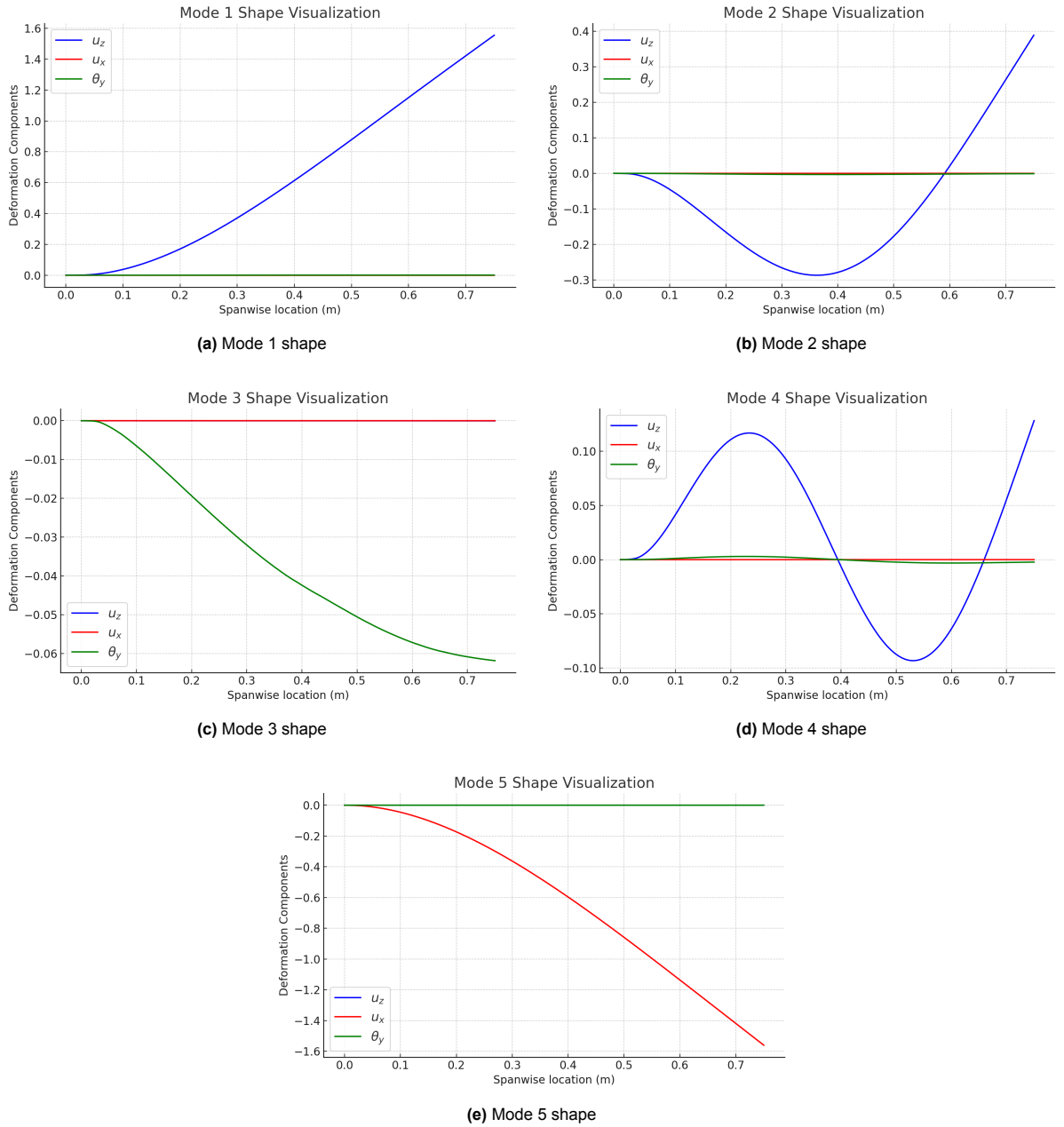

(a) Mode 1 shape

(b) Mode 2 shape

(c) Mode 3 shape

(d) Mode 4 shape

(e) Mode 5 shape

Figure 4.7: Spanwise deformations (u_x, u_z, θ_y) of the first five mode shapes of the 3D wing

The corresponding mode shapes are illustrated in Figure 4.8, highlighting the global deformation fields and directions of motion for each frequency.

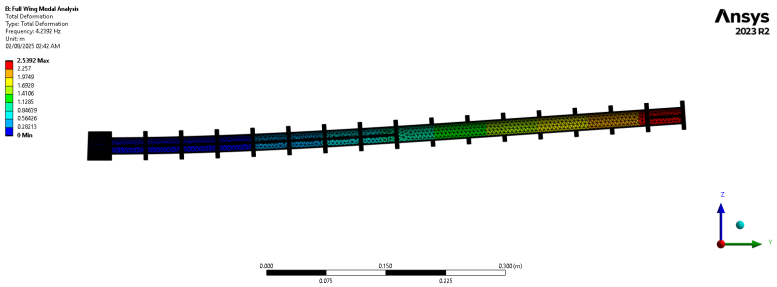

(a) Mode 1

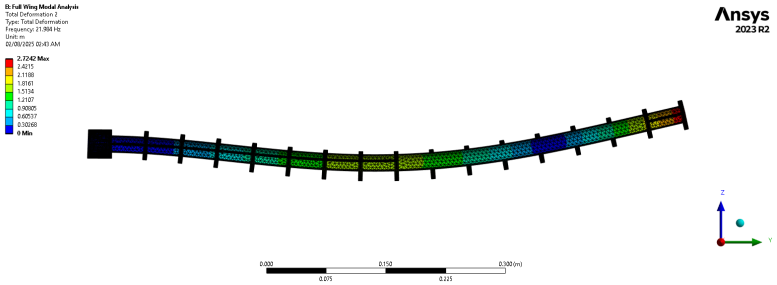

(b) Mode 2

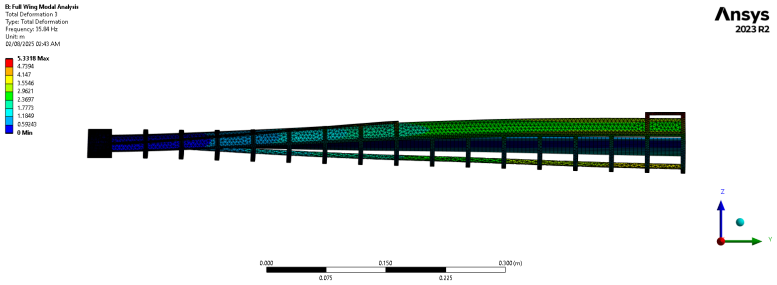

(c) Mode 3

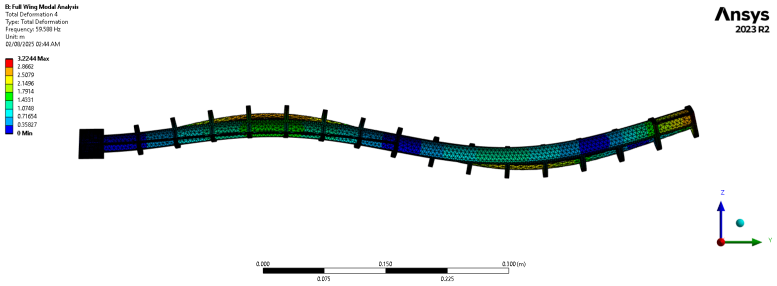

(d) Mode 4

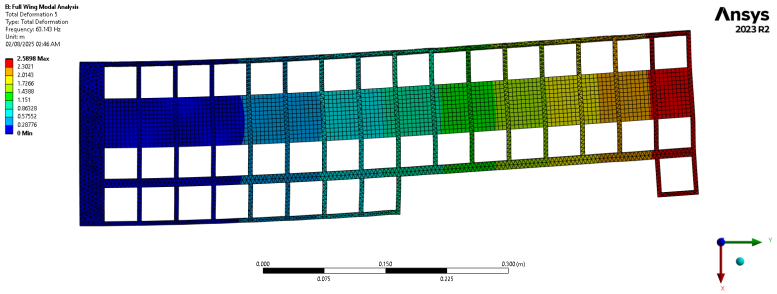

(e) Mode 5

Figure 4.8: 3D visualization of the global deformation fields for the first five modes

4.4. Global Stiffness Extraction from Linear Static FEM

To extract the stiffness properties of the 3D wing structure, a set of linear static simulations was conducted under prescribed unit moment loads. This analysis provides a basis for determining the wing's global bending and torsional stiffness, which is essential for constructing an equivalent one-dimensional beam model in later stages. The same simulation model setup described earlier in Section 4.2 is retained here.

4.4.1. Stiffness Extraction Methodology

The estimation of sectional stiffness properties from a FEM model can be carried out using the methodology proposed by Elsayed et al. [60]. In essence, the method is based on applying unit loads at the tip of a beam-like structure and measuring the corresponding displacements or rotations in a static linear FEM environment. By doing so, the flexural and torsional stiffnesses can be back-calculated directly from the load–deflection relationship, without the need for complex postprocessing of stresses or strain energy. The advantage of this approach is that it yields the effective, global stiffness values of the structure, which are directly compatible with one-dimensional beam formulations used in SHARPy.

Elsayed's method introduces two variants. In the first, known as the *principal axis approach*, the applied loads are aligned with the structure's principal bending and torsional directions. This leads to a decoupled formulation where each stiffness term is obtained independently from the corresponding load–rotation response. In the second, more general *off-axis approach*, unit loads are applied in arbitrary directions, and the resulting coupled response is resolved through a stiffness matrix formulation. While the latter allows treatment of asymmetrical or misaligned structures with significant coupling terms, the principal axis method is preferred when the structural axes are well aligned with the global coordinate system and coupling effects are negligible.

In applying this method to the present wing, several assumptions are introduced. The wing is treated as a slender beam, so that its deformation can be described by classical beam theory. The principal axes of bending and torsion are assumed to coincide with the global axes of the FEM model, allowing the response to be uncoupled. Loads are applied as concentrated moments at the tip of the wing, rather than as distributed forces, so the total span length (L) enters explicitly in the stiffness formulation. Furthermore, deformations are restricted to the linear elastic regime, and angular rotations are assumed small enough that $\tan\theta \approx \theta$. Finally, any local compliance effects at the tip face are either negligible or modeled using a `Remote Point` with deformable behavior. In this setup, the `Remote Point` acts as a reference node that averages the motion of all nodes on the face, so that the measured rotations correspond to the global beam deformation rather than small local warping of the tip surface.

Although these considerations suggest that the principal axis formulation may be appropriate, a validation test was performed to confirm that the wing's structural axes are sufficiently aligned with the global coordinate system. The FEM model setup described in Section 4.2 was retained. A `Remote Point` was created at the centroid of the spar tip face at $(0, 0.75, 0)$ m and linked to the surface with `Deformable` behavior, thereby ensuring physically representative global rotation of the wing tip without artificially over-constraining the section. Unit bending moments M_x, M_y, and M_z were individually applied at this point to induce deformation. The resulting rotations were tabulated in Table 4.6 below. The cross-terms are reported as a percentage of the dominant rotation in each case.

Load case	θ_x [rad]	θ_y [rad]	θ_z [rad]
M_x	$\mathbf{6.56 \times 10^{-2}}$	2.69×10^{-3} (4.10%)	1.08×10^{-6} (0.0016%)
M_y	3.2985×10^{-3} (5.40%)	$\mathbf{6.107 \times 10^{-2}}$	6.1829×10^{-6} (0.010%)
M_z	1.0785×10^{-6} (0.463%)	6.0812×10^{-8} (0.026%)	$\mathbf{2.333 \times 10^{-4}}$

Table 4.6: Rotations under unit moments about global axes

These results show that each global moment induces a response almost entirely in its intended axis, with cross-terms below about 5%, which confirms that the structural axes are sufficiently aligned with the global coordinate system for stiffness extraction with only minor flap–torsion leakage attributable

to structural eccentricities such as spar offset, uneven material distribution, tip mass eccentricities, or slight meshing imperfections.

A set of modeling options was also considered to minimize coupling effects, and their trade-offs are summarized in Table 4.7. Although these adjustments could further isolate principal axis behavior, the current model was deemed sufficiently representative of the actual wing while maintaining acceptable decoupling.

Option	Effect	Trade-off
Use simpler, symmetric geometry (e.g., spar-only)	Reduces structural coupling; yields cleaner, axis-aligned bending	Less representative of the actual wing structure
Apply moment directly to spar tip face only	Isolates bending in primary load path; minimizes influence of other structures	Ignores interaction with chassis and full tip surface
Run modal analysis instead of static bending	Identifies natural principal directions of deformation; no applied load assumptions	Requires eigenmode interpretation and doesn't yield EI or GJ directly
Avoid rigid Remote Points	Allows natural, distributed rotation across the tip face	Requires careful postprocessing and proper scoping

Table 4.7: Modeling options to reduce coupling and their trade-offs

Based on this validation, it was concluded that the wing's response is dominated by principal axis behavior. This justifies using the simplified, decoupled formulation proposed by Elsayed, in which bending and torsional stiffnesses are obtained directly from the load–rotation relationship. Accordingly, the stiffness values are computed as

$$EI_x = \frac{M_x \mathsf{L}}{\theta_x}, \qquad EI_z = \frac{M_z \mathsf{L}}{\theta_z}, \qquad GJ = \frac{M_y \mathsf{L}}{\theta_y}. \tag{4.6}$$

where EI_x and EI_z denote the bending stiffnesses about the X- and Z-axes, respectively, GJ is the torsional stiffness, M_x, M_y, and M_z are the applied unit bending and torsional moments, L is the total span length of the beam, and θ_x, θ_y, and θ_z are the corresponding rotations measured at the tip. This formulation provides the effective stiffness values required for the equivalent beam representation.

4.4.2. Load Case Setup

To extract the 3D wing structure's bending and torsional stiffnesses using the Elsayed methodology, unit moment loads were applied at the tip, and the resulting angular deformations were recorded. The simulation setup was identical to that described in Section 4.2.

To apply the directional moments and to capture the corresponding rotations, a `Remote Point` was created at the centroid of the spar tip face at coordinates $(0, 0.75, 0)$ m. Depending on the load case, this `Remote Point` was coupled either to the spar tip face alone or to both the spar and chassis tip faces through the (`MPC`) formulation, with all six DOFs activated and the behavior set to `Deformable`. A unit moment of 1 Nm was then applied about the axis of interest, and the resulting angular rotation was measured using a `Flexible Rotation Probe` at the `Remote Point`. For each load case, the global deformation field was visualized by extracting the corresponding translational displacement of the wing tip using `Directional Deformation`.

Load Case M_x [Out-of-plane Bending]
A unit moment about the X-axis produces upward or downward bending in the Z-direction. The spar is the primary vertical load-bearing structure, while the chassis contributes minor out-of-plane stiffness due to the absence of a skin. If the chassis tip face were included in the `Remote Point` coupling, its greater compliance and surface area would artificially reduce the apparent stiffness. To avoid this, the `Remote Point` was connected only to the spar tip face, which isolates flapwise bending and prevents contamination from local compliance effects.

Load Case M_y [Torsion]
A unit moment about the Y-axis induces twist along the spanwise axis. In this open structure, torsional resistance arises jointly from the spar and the partially enclosing chassis. Since the spar and chassis tip faces are aligned and act together in resisting torsion, both were coupled to the `Remote Point`. This ensures that the distributed torsional compliance of the structure is captured, providing a physically representative rotational response.

Load Case M_z [In-plane Bending]
A unit moment about the Z-axis produces in-plane bending, resulting in lag displacement in the X-direction. The spar primarily carries in-plane loads, whereas the large, thin chassis walls contribute minor stiffness and may undergo excessive local deformation. To prevent underestimation of the effective in-plane bending stiffness, the `Remote Point` was connected only to the spar tip face for this load case.

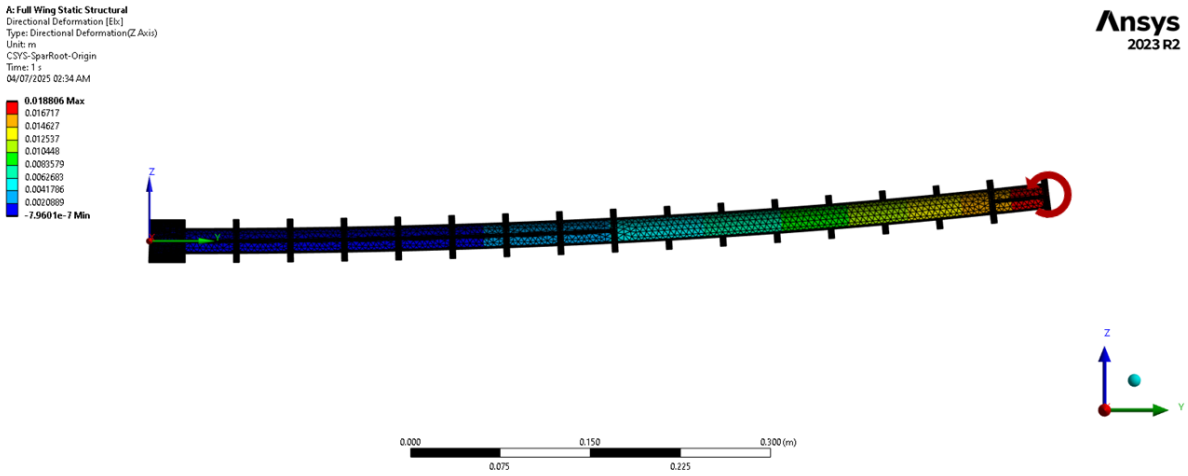

Figure 4.9: Primary translational deformation u_z due to load case M_x

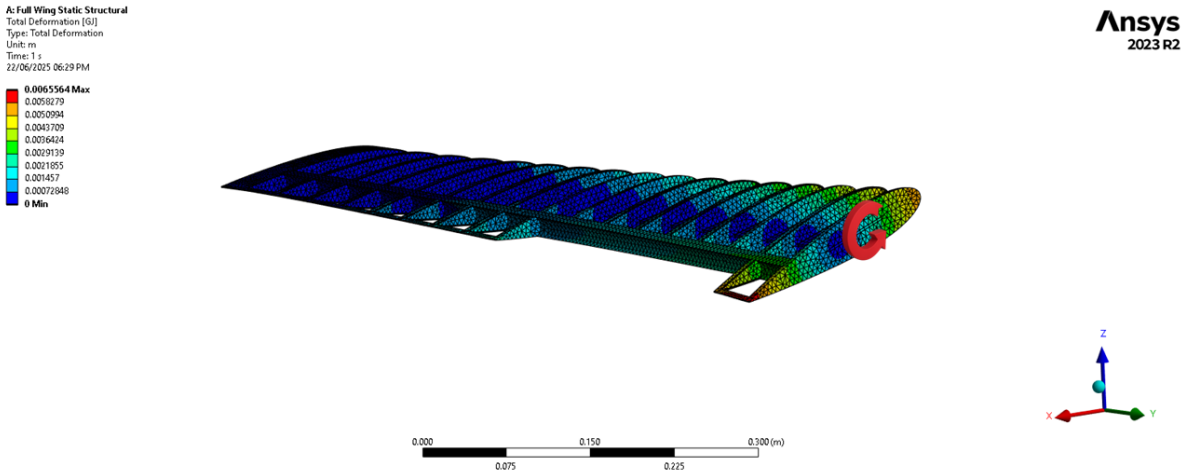

Figure 4.10: Torsion deformation due to load case M_y

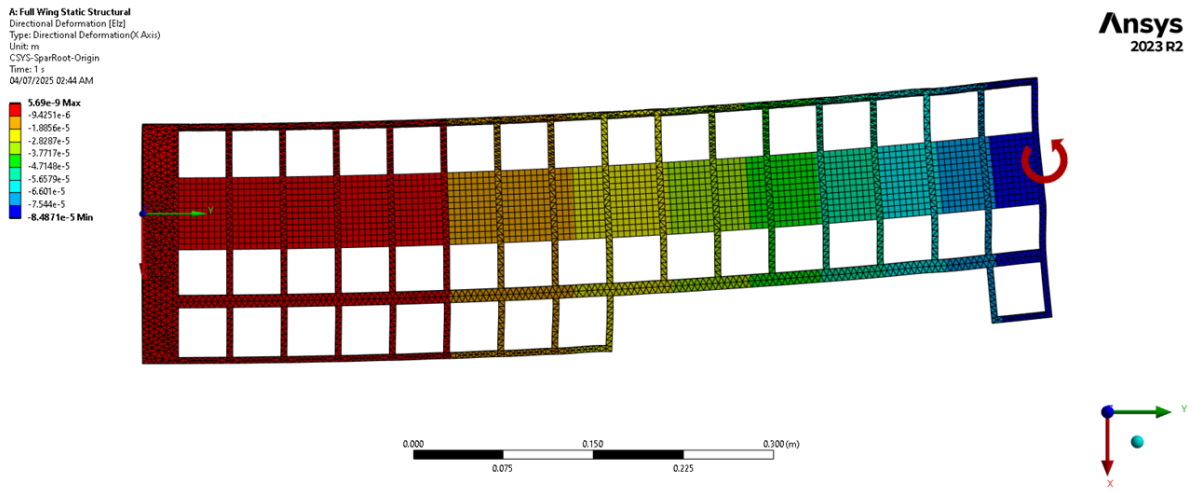

Figure 4.11: Primary translational deformation u_x due to load case M_z

4.4.3. Global Stiffness Extraction and Results

The unit moment load cases produced distinct deformation fields corresponding to each principal direction of bending and torsion, as illustrated in Figures 4.9, 4.10, and 4.11. These deformation patterns show that the applied moments generate dominant responses in the intended directions (out-of-plane, torsional, and in-plane, respectively), with only minor secondary components. This confirms that the wing deforms primarily about its principal axes, with negligible coupling, thereby validating the use of the principal-axis stiffness formulation. The global rotational and translational response of the 3D wing structure under each loading condition is summarized in Table 4.8.

Axis	Load case	Interpretation	Tip Rotation [rad]	Tip Displacement [m]
X	M_x	Out-of-plane bending	θ_x = 6.555E-02	u_z = 1.881E-02
Y	M_y	Torsion	θ_y = 6.107E-02	-
Z	M_z	In-plane bending	θ_z = 2.333E-04	u_x = -8.487E-05

Table 4.8: Linear static response of 3D wing to unit moment loads about principal axes

The corresponding global stiffness values were computed using Equation 4.6, assuming a beam length of L = 0.75 m and unit moment magnitudes. The results are as follows:

$$
\begin{aligned}
EI_x \quad \text{[Out-of-plane Bending Stiffness]} &= \frac{1 \cdot 0.75}{6.555 \times 10^{-2}} = 11.441 \text{ Nm}^2 \\
GJ \quad \text{[Torsional Stiffness]} &= \frac{1 \cdot 0.75}{6.107 \times 10^{-2}} = 12.281 \text{ Nm}^2 \\
EI_z \quad \text{[In-plane Bending Stiffness]} &= \frac{1 \cdot 0.75}{2.333 \times 10^{-4}} = 3214.745 \text{ Nm}^2
\end{aligned}
$$

In addition to tip displacements used for global stiffness extraction, the spanwise deformation fields were extracted from the 3D FEM model along the elastic axis to study the shape of structural response under unit moment loads. These deformations, illustrated in Figure 4.12, will be used to compare the equivalent beam model developed later in the chapter.

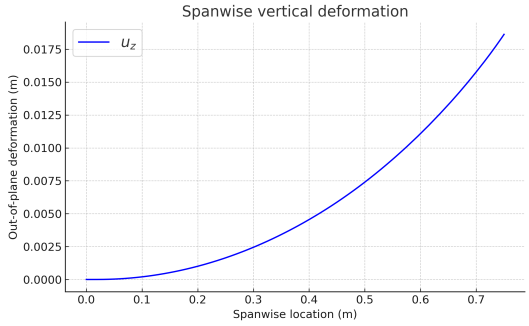

(a) Spanwise vertical displacement due to M_x moment load

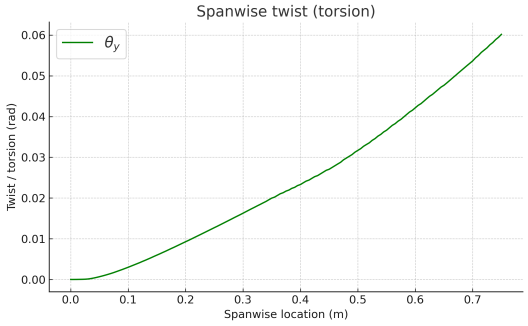

(b) Spanwise twist due to M_y moment load

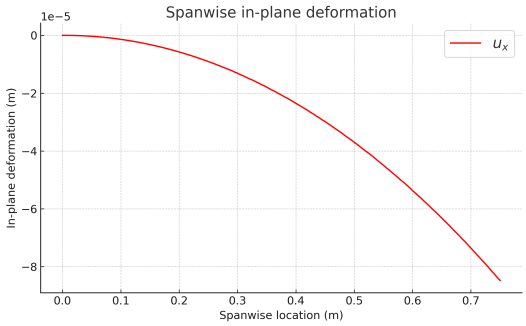

(c) Spanwise horizontal displacement due to M_z moment load

Figure 4.12: Spanwise deformations (u_z, u_x, θ_y) due to unit moment loads

Stiffness Sensitivity Analysis for 3D Wing

While the primary stiffness values reported above reflect the selected modeling configuration, the extracted results are sensitive to the definition of the tip boundary condition, specifically the combination of `Remote Point` behavior (rigid vs. deformable) and the choice of tip face selection (spar only vs. spar + chassis). A systematic sensitivity analysis was performed across all three loading cases to evaluate this. The simulation environment described in Section 4.2 and the clamped-free boundary condition were retained for all simulations, while only the `Remote Point` settings were varied. Four configurations were tested for each unit moment load case (M_x, M_y, and M_z): a rigid `Remote Point` coupled to the spar tip face only, a rigid `Remote Point` coupled to both the spar and chassis tip faces, a deformable `Remote Point` coupled to the spar tip face only, and a deformable `Remote Point` coupled to both the spar and chassis tip faces. Table 4.9 summarizes the resulting stiffness values, where the final configuration adopted for each load case is highlighted in **bold**.

Stiffness	Remote Point	Spar Only	Spar + Chassis
EI_x [Nm^2]	Rigid	12.23	31.28
	Deformable	**11.44**	9.95
GJ [Nm^2]	Rigid	12.97	23.86
	Deformable	12.48	**12.28**
EI_z [Nm^2]	Rigid	3216.81	3561.93
	Deformable	**3214.74**	788.74

Table 4.9: Sensitivity of extracted stiffness values to remote point behavior and face selection

Representative deformation visualizations for each load case and `Remote Point` configuration are provided in Figures 4.13 4.13, and 4.15.

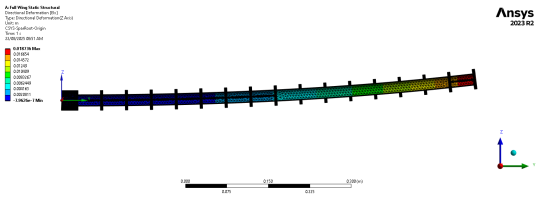

(a) Rigid, Spar Only

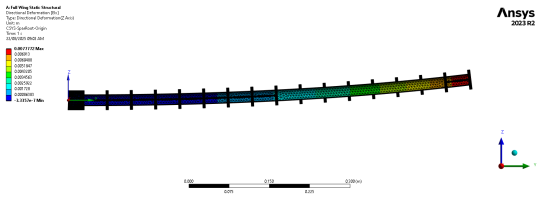

(b) Rigid, Spar + Chassis

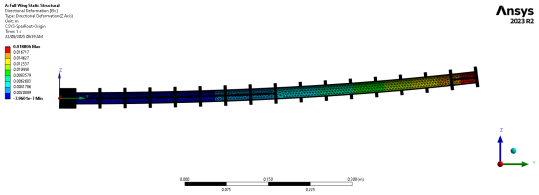

(c) Deformable, Spar Only

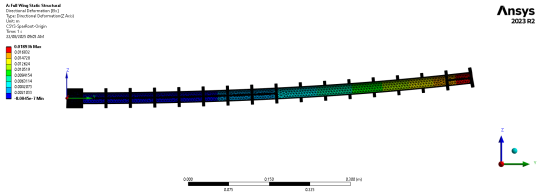

(d) Deformable, Spar + Chassis

Figure 4.13: Wing deformation under unit moment M_x

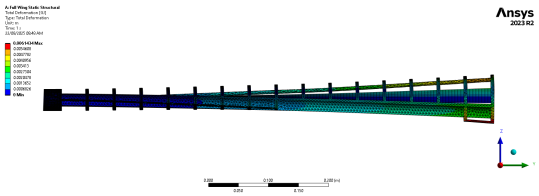

(a) Rigid, Spar Only

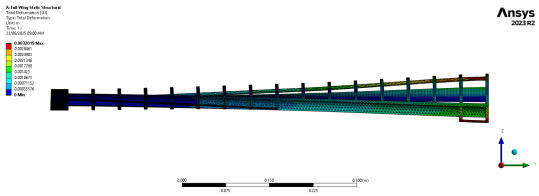

(b) Rigid, Spar + Chassis

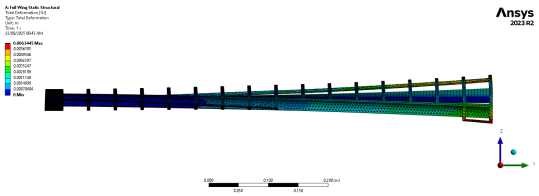

(c) Deformable, Spar Only

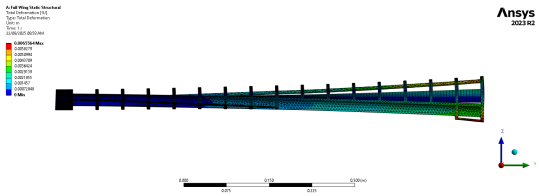

(d) Deformable, Spar + Chassis

Figure 4.14: Wing deformation under unit moment M_y

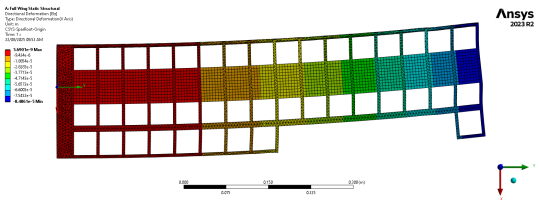

(a) Rigid, Spar Only

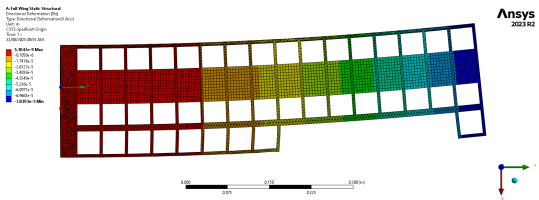

(b) Rigid, Spar + Chassis

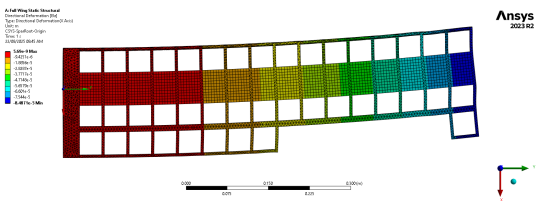

(c) Deformable, Spar Only

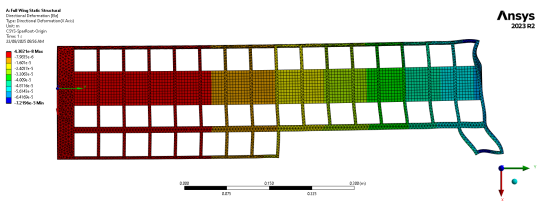

(d) Deformable, Spar + Chassis

Figure 4.15: Wing deformation under unit moment M_z

The stiffness values remained relatively stable when the `Remote Point` was coupled only to the spar tip face, regardless of whether a rigid or deformable formulation was used. This consistency indicates that the spar dominates the structural response in all three loading directions.

When the chassis tip face was also included, significant variation in the extracted stiffness values appeared, particularly with the `Deformable Remote Point`. The larger surface area and lower chassis stiffness introduced excessive compliance, which was most pronounced in the in-plane bending case. In this configuration, the effective stiffness dropped by more than 75%, highlighting the sensitivity of the results to the choice of selection.

For the M_x load case (out-of-plane bending), both rigid and deformable `Remote Points` coupled to the spar tip face produced nearly identical deformation fields and stiffness values (12.23 Nm^2 vs. 11.44 Nm^2). This similarity suggests that uniform section rotation occurs naturally, independent of the coupling type. Nevertheless, the deformable formulation was selected for consistency across all load cases and to better reflect physical compliance.

In the torsional M_y load case, the final configuration included both the spar and chassis tip faces. The extracted stiffness of 12.28 Nm^2 confirmed that both surfaces contribute to torsional resistance. This approach provides a more physically representative description of load transfer at the flush wing tip interface.

For the in-plane bending M_z case, the stiffness values were again nearly identical between rigid and deformable `Remote Points` when only the spar tip face was selected (3216.81 Nm^2 vs. 3214.74 Nm^2). However, including the chassis tip face led to extreme underestimation due to dominant local warping effects and was therefore excluded from the final setup.

Based on physical reasoning and the observed numerical trends, the following final configuration was adopted. For M_x, a `Deformable Remote Point` coupled only to the spar tip face was used. In M_y, the `Remote Point` was coupled to both the spar and chassis tip faces, since both contribute to resisting twist. For M_z, the configuration again employed a `Deformable Remote Point` linked solely to the spar tip face. This setup was found to be best for capturing the global structural behavior of the wing while minimizing the influence of local compliance artifacts.

4.5. Section-Wise Structural Analysis

To better capture the spanwise variation in stiffness properties, the 3D FEM wing model was decomposed into four discrete structural segments referred to as sections. The root region spans 0–0.05 m, the mid-section spans 0.05–0.365 m, the aileron region spans 0.365–0.725 m, and the tip region spans 0.725–0.750 m. This division was chosen based on changes in structural cross-sectional properties visible in the 3D geometry. Each section corresponds to a portion of the wing where material distribution, internal geometry, or mass features differ. This segmentation allows for deriving non-uniform stiffness properties that reflect the actual structural behavior along the span, rather than assuming a uniform beam. Figure 4.16 illustrates the segmentation overlaid on the simplified wing model.

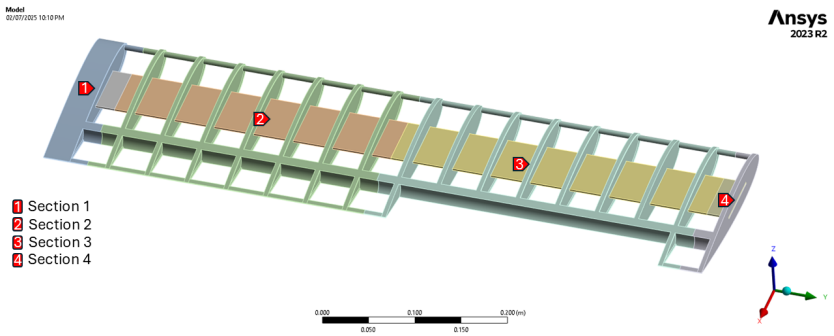

Figure 4.16: Spanwise segmentation of the simplified wing model into four structural sections

4.5.1. Section Modeling Assumptions

The section-wise stiffness extraction was performed under a set of simplifying assumptions. Each section was analyzed independently, assuming negligible interaction across section interfaces, which allowed structural decoupling and simplified parameter extraction. Within a section, material properties, cross-sectional geometry, and stiffness were treated uniformly so that each segment could be characterized by a single representative EI and GJ value. Tip loading was applied as unit moments at the free end of each section, rather than distributed forces, to maintain consistency with the global wing stiffness extraction and with Elsayed's methodology. All sections were assumed to share the same coordinate orientation as the global wing, enabling stiffness estimation to be decoupled into EI_x, GJ, and EI_z. The boundary condition for each section was defined by fixing the root face, thereby emulating a clamped cantilever constraint. Linear elastic material behavior was assumed throughout, with no geometric or material nonlinearity included.

4.5.2. Section-wise Linear Static Analysis

Each section was meshed and analyzed in ANSYS using the same modeling approach described for the whole wing in Section 4.2. The material assignments, contact definitions, and point mass treatments were retained identically. The mesh resolution varied across sections due to size and internal detail differences. Figure 4.17 shows the FEM models for all four sections. Mesh statistics are summarized in Table 4.10.

Section	Node Count	Element Count
Section 1	18795	9124
Section 2	52049	22749
Section 3	49383	21874
Section 4	5292	2255

Table 4.10: Node and element counts for each FEM section model

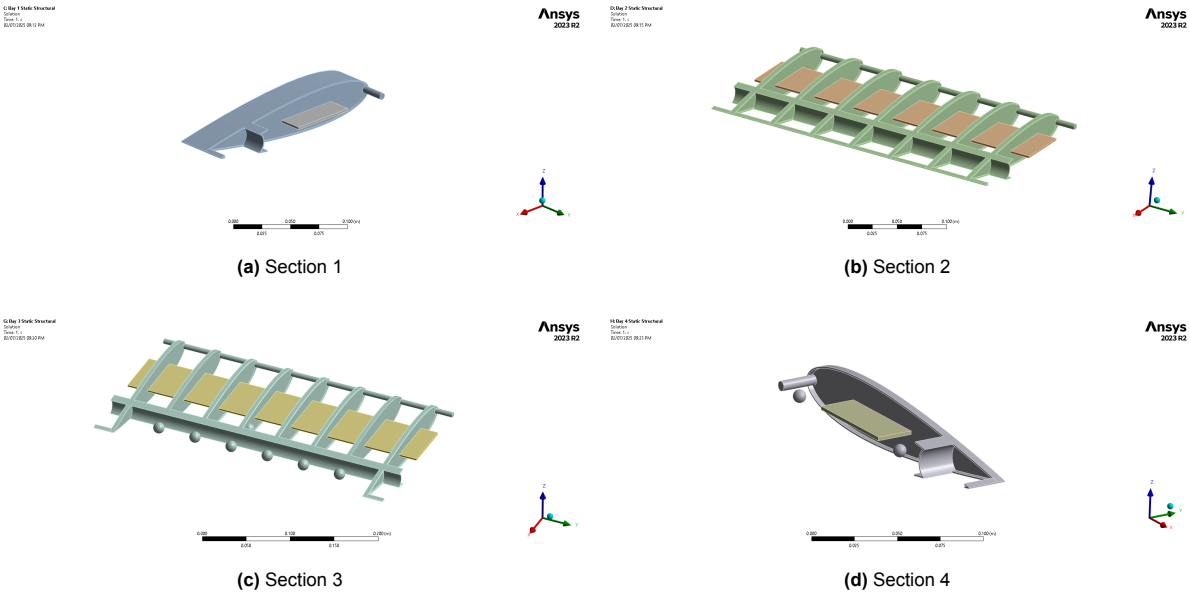

(a) Section 1 **(b)** Section 2

(c) Section 3 **(d)** Section 4

Figure 4.17: Spanwise divided 3D FEM wing as four sections 1 through 4

4.5.3. Boundary Conditions and Remote Point Setup

Each section was modeled as a cantilevered beam segment using the same tip-loading methodology applied to the whole wing, following Elsayed. The inboard faces of each section were assigned a `Fixed Support`. A `Remote Point` was defined at the centroid of each section's outboard spar tip face, scoped to a dedicated `Named Selection` encompassing the relevant tip geometry. While all sections

followed a cantilever boundary definition, the `Remote Point` behavior and face selecting strategy varied depending on the structural context, as outlined below.

Sections 1–3

For Sections 1–3, the structures were modeled as idealized beams with rigid cross-sectional rotation. The `Remote Point` behavior was set to `Rigid`, and all available tip faces, including the spar, web, and chassis, were included in the coupling. Although these sections are not closed cross-sections, enforcing rigid rotation of all tip faces forces them to behave as if they were nearly enclosed. This approach ensures that the applied moment produces uniform section rotation, consistent with an equivalent beam representation, and avoids spurious local twisting of individual faces.

Section 4

Section 4 terminates at the wing tip; therefore, its structural behavior differs from the inner sections. Unlike Sections 1–3, which are bounded by internal ribs and webs that provide restraint, Section 4 has no continuation of structure beyond its free end. As a result, the local compliance of the tip region plays a more significant role, particularly due to the greater flexibility of the chassis compared to the spar. To capture this behavior, a targeted sensitivity analysis was performed in which the `Remote Point` was varied. Both rigid and deformable behaviors were considered, and the coupling was applied either to the spar tip face alone or to both the spar and chassis tip faces. This procedure mirrors the approach used for the full wing and allowed the most representative configuration for Section 4 to be identified. The resulting stiffness values for EI_x, GJ, and EI_z are summarized in Table 4.11. The final configuration used for section 4 stiffness extraction is highlighted in **bold**.

Stiffness Type	Remote Point	Spar Only	Spar + Chassis
EI_x [Nm^2]	Rigid	4.98	9.57
	Deformable	**2.85**	1.39
GJ [Nm^2]	Rigid	48.22	102.04
	Deformable	24.11	**41.33**
EI_z [Nm^2]	Rigid	3002.71	3893.17
	Deformable	**2943.29**	83.68

Table 4.11: Sensitivity of section 4 stiffness to remote point behavior and face selection

To complement the stiffness sensitivity data, Figures 4.18, 4.19, and 4.20 show the deformation fields observed for section 4 under the unit moment load cases M_x, M_y, and M_z, respectively. Each figure compares the four tested remote point configurations.

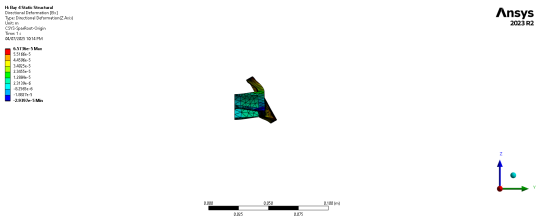

(a) Rigid, Spar Only

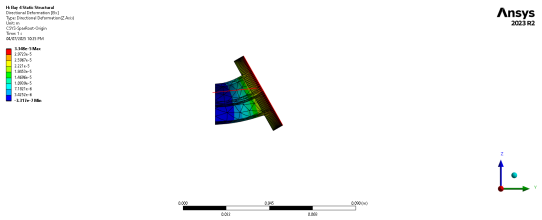

(b) Rigid, Spar + Chassis

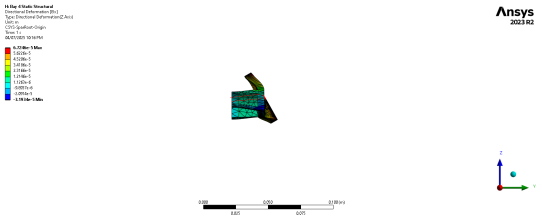

(c) Deformable, Spar Only

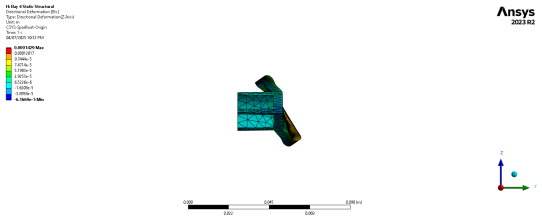

(d) Deformable, Spar + Chassis

Figure 4.18: Bay 4 deformation under unit moment M_x

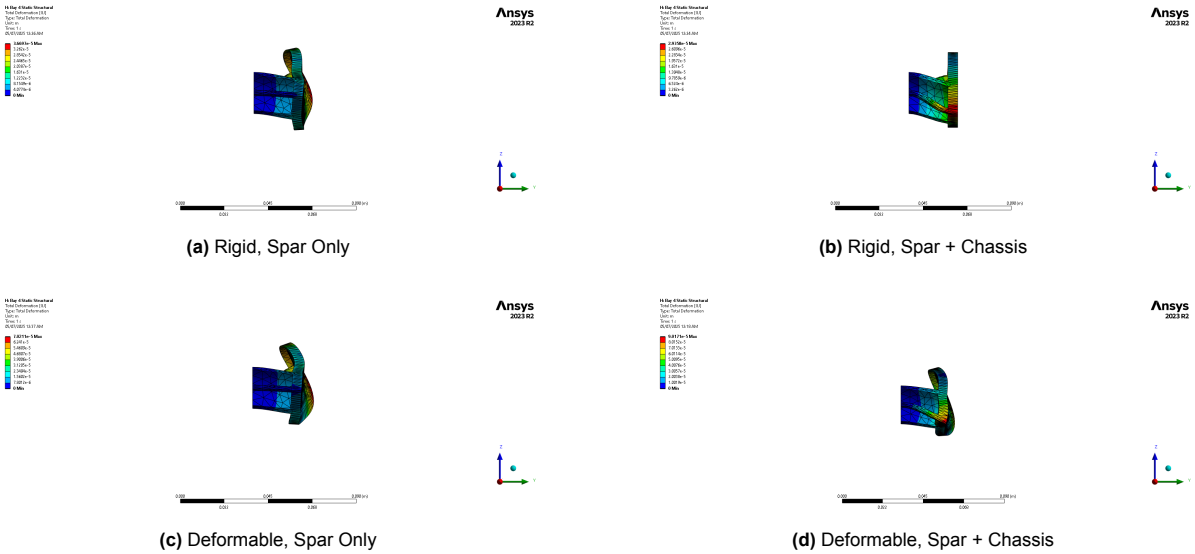

(a) Rigid, Spar Only

(b) Rigid, Spar + Chassis

(c) Deformable, Spar Only

(d) Deformable, Spar + Chassis

Figure 4.19: Bay 4 deformation under unit moment M_y

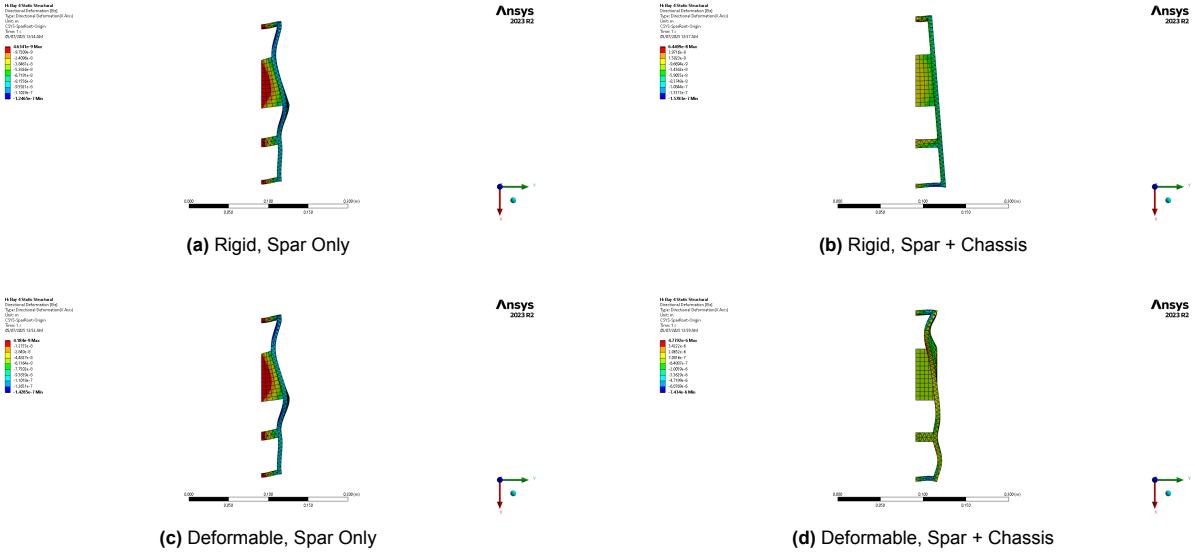

(a) Rigid, Spar Only

(b) Rigid, Spar + Chassis

(c) Deformable, Spar Only

(d) Deformable, Spar + Chassis

Figure 4.20: Bay 4 deformation under unit moment M_z

The sensitivity analysis for Section 4 highlights how strongly the extracted stiffness values depend on the `Remote Point` definition and the choice of coupled faces. In out-of-plane bending, the spar-only selection with a `Deformable Remote Point` gave the lowest and most stable value (2.85 Nm^2). Including the chassis face reduced the stiffness even further (1.39 Nm^2) because the relatively flexible chassis dominates the tip deformation. In contrast, rigid coupling inflated the apparent stiffness, especially when both faces were included (9.57 Nm^2), by enforcing uniform rotation across all nodes.

In torsion, both spar and chassis contribute to resisting twist. This is reflected in the much higher stiffness when both faces were coupled, particularly under the `Deformable Remote Point` (41.33 Nm^2). The spar-only values were significantly lower (24.11 Nm^2 deformable, 48.22 Nm^2 rigid), showing that neglecting the chassis underestimates torsional resistance, while rigid coupling again produces an artificially stiff response.

For in-plane bending, the spar-only configuration with a `Deformable Remote Point` produced a value of 2943.29 Nm^2, consistent with the expected order of magnitude. Coupling both spar and chassis un-

der a deformable formulation caused a severe drop in stiffness (83.68 Nm^2), dominated by excessive local deformation of the chassis tip face. The rigid couplings again produced higher values (3002.71 and 3893.17 Nm^2) by suppressing local warping.

Overall, these results show that rigid formulations consistently over-predict stiffness by constraining natural deformation at the tip, while deformable couplings reveal the influence of the flexible chassis. Based on these trends, the final configurations adopted were: spar-only deformable for EI_x and EI_z, and spar+chassis deformable for GJ. This configuration provides stiffness values of the correct order of magnitude compared to the full-wing analysis, while also avoiding the artificial stiffening introduced by rigid couplings and the severe underestimation caused by chassis-dominated local deformations at the tip.

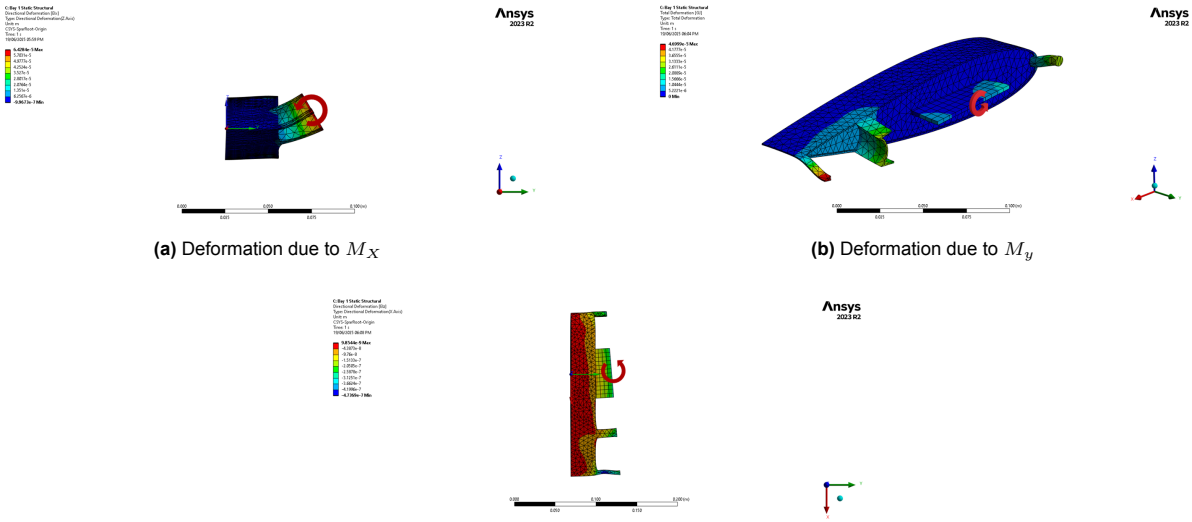

(a) Deformation due to M_X

(b) Deformation due to M_y

(c) Deformation due to M_z

Figure 4.21: Linear static structural analysis for Bay 1

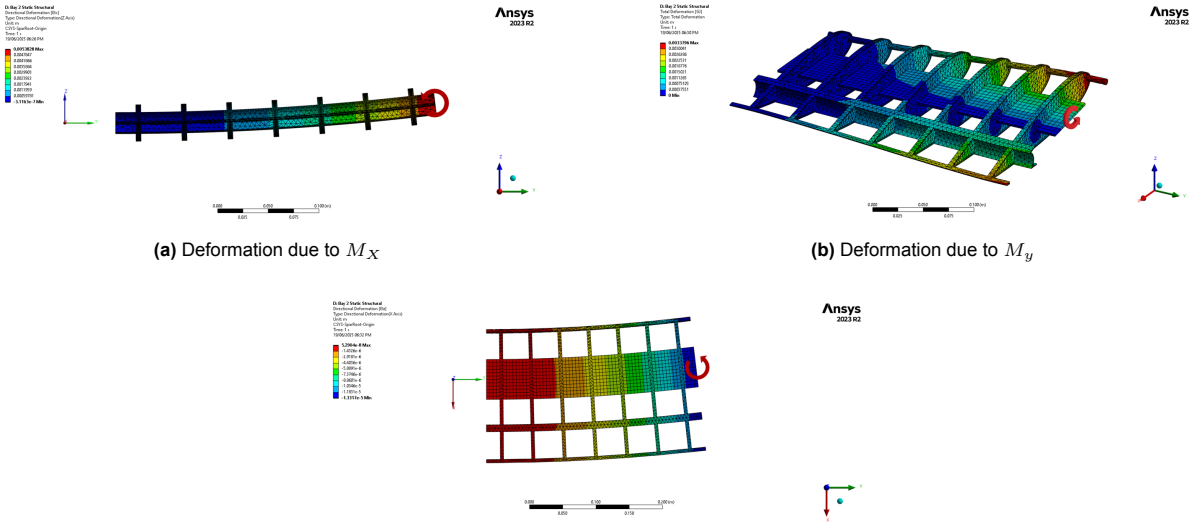

(a) Deformation due to M_X

(b) Deformation due to M_y

(c) Deformation due to M_z

Figure 4.22: Linear static structural analysis for Bay 2

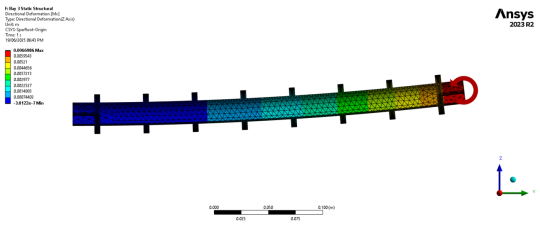

(a) Deformation due to M_X

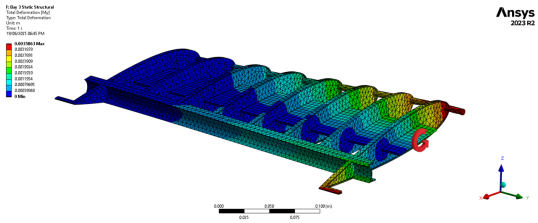

(b) Deformation due to M_y

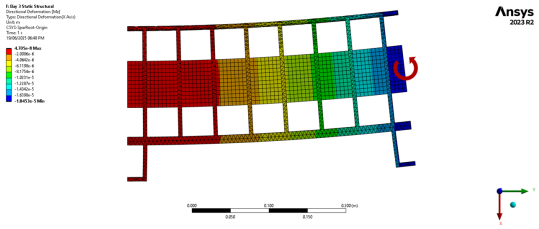

(c) Deformation due to M_z

Figure 4.23: Linear static structural analysis for Bay 3

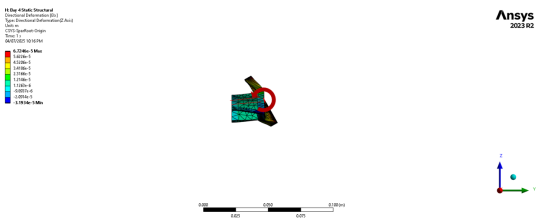

(a) Deformation due to M_X

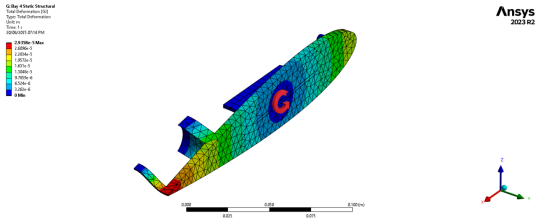

(b) Deformation due to M_y

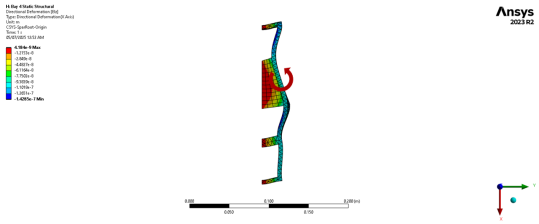

(c) Deformation due to M_z

Figure 4.24: Linear static structural analysis for Bay 4

Results and Postprocessing

The Figures 4.21, 4.22, 4.23, and 4.24 show the resulting displacement contours corresponding to each unit moment M_x, M_y, and M_z load case for each section 1 through 4, respectively. Each section's applied unit moment load cases resulted in distinct deformation fields aligned with the principal bending and torsional directions. Angular rotations about the X, Y, and Z axes were extracted at the `Remote Point` for each load case. Using the methodology of Elsayed et al. [60] and the principal stiffness expressions in Equation 4.6, the out-of-plane bending, torsional, and in-plane bending stiffnesses were tabulated in Table 4.12 for each section.

Section	Length L [m]	Tip Rotational Deformations [rad]			Static Stiffnesses [Nm^2]		
		θ_x	θ_y	θ_z	EI_x	GJ	EI_z
Section 1	0.050	3.623E-03	3.916E-04	1.153E-05	13.801	127.691	4335.385
Section 2	0.315	3.472E-02	3.230E-02	8.455E-05	9.073	9.753	3725.650
Section 3	0.360	3.823E-02	3.457E-02	1.025E-04	9.417	10.414	3510.825
Section 4	0.025	8.770E-03	6.048E-04	8.494E-06	2.851	41.333	2943.289

Table 4.12: Extracted rotations and stiffness values per section using linear static unit moment loads

These values reflect the non-uniform structural composition across the span. Sections 2 and 3, which cover most of the span, yield stiffnesses close to the wing's general behavior. Section 1 shows the largest stiffnesses at the root, consistent with material build-up and the clamped boundary condition. Section 4 deviates most from the mid□span trends due to its very short length and lower material content: EI_x is the smallest, EI_z remains of the same order as other sections, and GJ is higher than in Sections 2–3 because both the spar and chassis tip faces were included in the `Remote Point` connection for the torsional load case.

4.6. Equivalent Beam Derivation

The preceding analyses of the 3D wing structure, both global and section-wise, produced spanwise distributions of bending and torsional stiffness. The geometry must be simplified into a segmented equivalent beam to use this structural model in SHARPy's aeroelastic framework. This reduced-order representation allows efficient aeroelastic simulation while retaining the essential structural flexibility of the whole wing.

The equivalent beam was developed iteratively with validation interleaved. First, spanwise stiffnesses obtained from the section-wise FEM analyses were assigned to the beam elements to reproduce the 3D wing's static response under unit bending and torsional moments. This stiffness configuration was validated against the 3D model by comparing spanwise deflection and twist, including tip rotations. With fixed stiffness, the beam's modal properties were matched to the 3D wing by adjusting only the mass and rotational inertia distributions until the natural frequencies and mode shapes agreed. A final validation quantified using the modal assurance criteria confirmed that the updated inertias preserved the static match while delivering consistent modal behavior relative to the 3D wing.

4.6.1. 1D Beam Model Definition and FEM Setup

A one-dimensional (1D) beam model was created in ANSYS SpaceClaim 2023 R2 as a line geometry divided into four segments, each corresponding to a structural section. These line segments were converted into `Beam Bodies` with temporary cross-sections for FEM setup. The beam was aligned with the global Cartesian system identical to the 3D wing, with the span along the Y-axis, the chord along the X-axis, and the vertical direction along the Z-axis. Local beam axes follow the standard ANSYS convention. The resulting geometry and segmentation are shown in Figure 4.25.

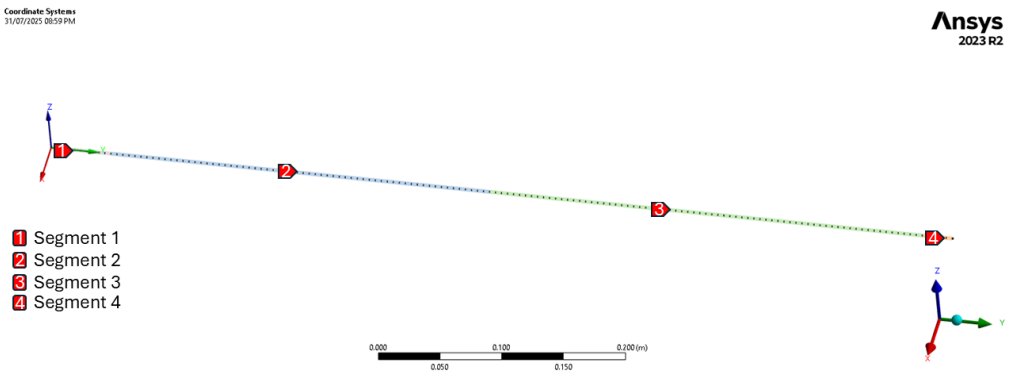

Figure 4.25: Spanwise segmentation of the 1D beam model into four sections

The FEM setup of the beam model followed two main steps. First, the interfaces between the four beam segments were connected using `Bonded Contact` to ensure structural continuity across the span. Second, a uniform mesh size of 5 mm was applied along the total beam length of 0.75 m, yielding 150 elements and 151 nodes.

4.6.2. Stiffness Matching

The first step in the derivation of the equivalent beam model is to match its structural stiffness with that of the segmented 3D FEM wing. In ANSYS Mechanical, stiffness values (EI_x, GJ, EI_z) cannot be directly assigned. Instead, user-defined beam cross-sections must be specified through geometric properties, namely, the cross-sectional area A, and the second moments of area about each axis (I_{yy}, I_{zz}) and the torsional constant J. Following classical beam theory, these geometric parameters are related to stiffness via material properties.

The flexural and torsional stiffnesses extracted from the 3D FEM static simulations of each section were used to compute the required cross-sectional properties under the assumption of aluminum material:

$$I_{yy}^{1D} = \frac{EI_x^{3D}}{E}, \quad I_{zz}^{1D} = \frac{EI_z^{3D}}{E}, \quad J^{1D} = \frac{GJ^{3D}}{G} \tag{4.7}$$

where E and G are Aluminum material properties, previously defined in Table 4.2. These computed geometric properties were assigned to a user-defined beam cross-section for each beam segment. In addition to stiffness, the cross-sectional area A was set to match the volume distribution of each 3D section:

$$A = \frac{\mathsf{V}_{\text{section}}}{\mathsf{L}_{\text{section}}} \tag{4.8}$$

where $\mathsf{V}_{\text{section}}$ is the volume of the material in the section obtained from the 3D FEM model and $\mathsf{L}_{\text{section}}$ is its spanwise length. The Table 4.13 below summarizes the spanwise cross-sectional properties of the equivalent beam model.

Segment	**Length** [m]	**Volume** [m^3]	EI_x [Nm^2]	GJ [Nm^2]	EI_z [Nm^2]	I_{yy} [m^4]	J [m^4]	I_{zz} [m^4]	A [m^2]
1	0.050	5.055E-05	13.801	127.691	4335.385	1.944E-10	4.784E-09	6.106E-08	1.011E-03
2	0.315	1.406E-04	9.073	9.753	3725.650	1.278E-10	3.654E-10	5.247E-08	4.463E-04
3	0.360	1.870E-04	9.417	10.414	3510.825	1.326E-10	3.901E-10	4.945E-08	5.194E-04
4	0.025	1.587E-05	2.851	41.333	2943.289	4.015E-11	1.549E-09	4.145E-08	6.350E-04

Table 4.13: Spanwise segmented cross-sectional properties derived from stiffness-matching of FEM results

To validate the cross-sectional properties and confirm that the segmented beam reproduces the structural response of the 3D wing, linear static analyses were performed. Each beam segment was assigned the stiffness values obtained from its corresponding section. The beam root node was fixed to emulate a clamped condition, and a `Remote Point` was defined at the tip to apply unit moments about the X, Y, and Z axes. Angular rotations at the tip and spanwise translational and rotational deformations were extracted for each load case along the beam nodes. This enabled direct evaluation of bending and torsional stiffness along the span. The segmented beam was thus expected to reproduce similar static compliance as the 3D FEM wing when subjected to equivalent tip moments.

Preliminary Results

The tip deformation results from the 1D beam model were compared directly with those of the 3D FEM wing under identical unit moment loading and are summarized in Table 4.14. In addition to tip displacements, the spanwise deformations were extracted from the 1D beam model. The Figure 4.26 visualizes the deformations along the beam for the three individual unit moment loads.

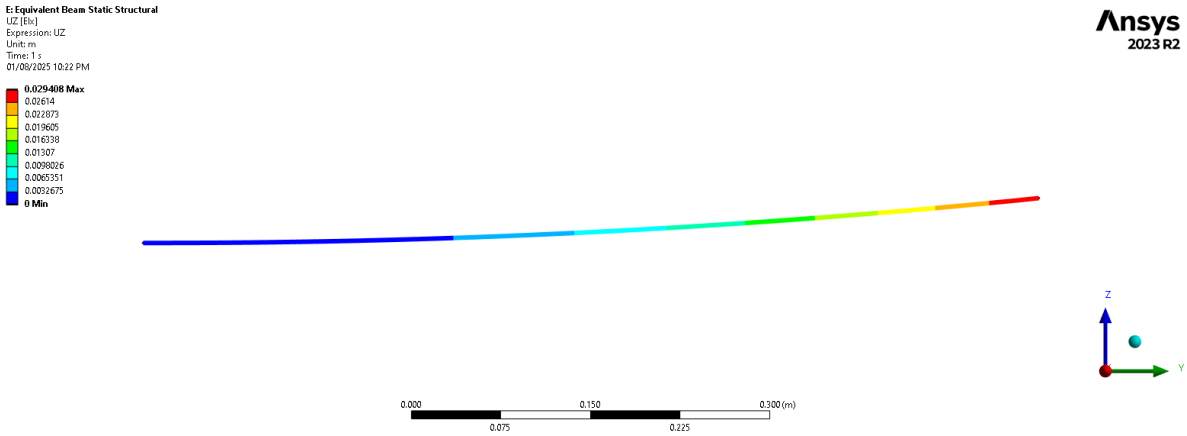

(a) Translational deformation u_z due to unit moment M_x

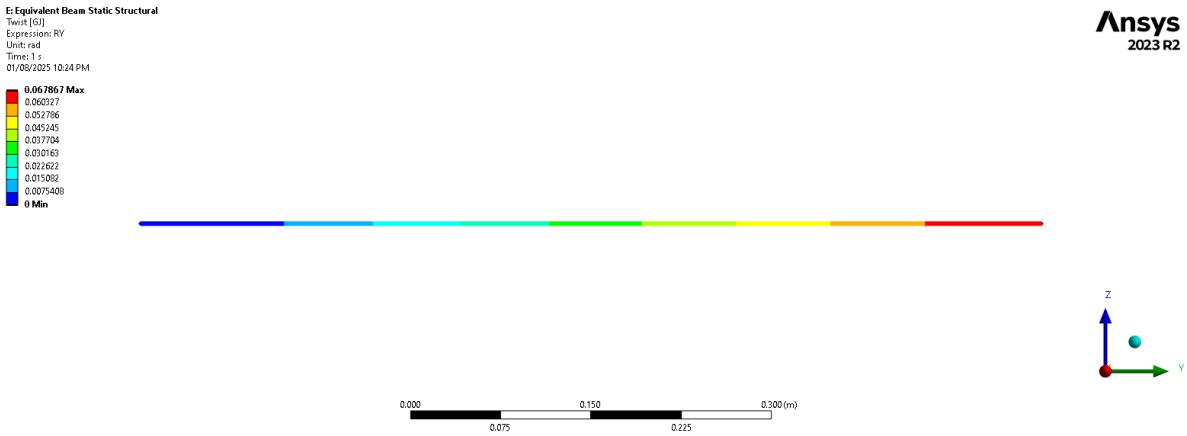

(b) Twist θ_y due to unit moment M_y

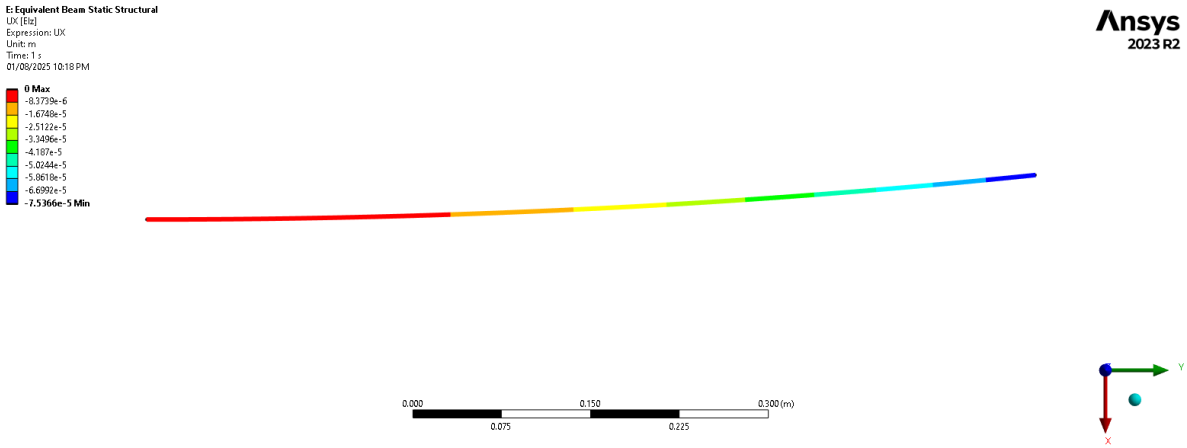

(c) Translational deformation u_x due to unit moment M_z

Figure 4.26: 1D beam spanwise deformations

Quantity	Load case	3D Wing	1D Beam	Relative Error
Tip Displacement u_z [m]	M_x	1.881×10^{-2}	2.941×10^{-2}	$+56.3\%$
Tip Rotation θ_y [rad]	M_y	6.107×10^{-2}	6.789×10^{-2}	$+11.2\%$
Tip Displacement u_x [m]	M_z	-8.487×10^{-5}	-7.536×10^{-5}	-11.2%

Table 4.14: Comparison of tip deformation results under unit moment loading: 3D FEM wing vs. segmented beam

The segmented 1D beam shows notable deviation from the 3D FEM wing, especially in out-of-plane bending. The tip displacement u_z under M_x is overestimated by about 56%. This is because bending loads concentrate at the clamped root, making the response highly sensitive to the local EI_x. This arises because the applied bending moment is largest at the clamped root, making the tip displacement highly sensitive to the effective EI_x in that region.

In the 3D wing, multiple structural members such as the spar, ribs, and chassis share this load to resist bending. At the same time, the 1D beam reduces it to a simplified line element, underestimating root stiffness and increasing compliance. By comparison, since fewer dominant members govern these responses, torsional rotation and in-plane bending displacement deviate more moderately at $+11\%$ and -11%. As a result, while the current beam formulation reflects the main structural trends, it does not directly reproduce the static compliance of the 3D wing.

To address this, the following subsection introduces stiffness scaling, where the sectional stiffness values obtained using Elsayed's method are used as a starting point and then adjusted with per-section or global scaling factors to improve the match between the beam's static response and that of the 3D wing.

Stiffness Scaling

Their cross-sectional stiffness properties govern the deformation of slender beams under applied loads such that bending behavior is controlled by the product EI, while torsional response is dictated by GJ. In bending, the applied moment is related to the beam's curvature according to:

$$M = EI \cdot \frac{d^2w}{dy^2} \tag{4.9}$$

where $\frac{d^2w}{dy^2}$ is the second derivative of the displacement field. The corresponding displacements are obtained by integrating this relation along the span. Similarly, in torsion, the applied torque is related to the twist gradient through:

$$M = GJ \cdot \frac{d\theta}{dy} \tag{4.10}$$

with the total twist angle $\theta(y)$ obtained by integration. These relations highlight that adjusting the values of EI and GJ directly modifies the compliance of the equivalent beam under bending and torsional moments, providing a straightforward way to scale stiffness properties to better match the 3D wing response.

In practice, scaling the bending stiffness EI uniformly rescales the deflection amplitudes while preserving the deformation shape. Simple scalar factors were applied only to the bending stiffness components to exploit this. For each bending case, a global scaling factor γ_i was computed as the ratio of 1D beam to 3D FEM tip responses:

$$\gamma_i = \frac{u_i^{\text{beam}}}{u_i^{\text{FEM}}}, \quad i \in \{x, z\}, \tag{4.11}$$

and used to scale the second moments of area I_{yy} and I_{zz} across all sections.

For torsion, GJ affects the twist distribution more directly, and its accuracy depends on how the spanwise variation of J is defined. Hence, a single scaling factor proved insufficient. Although it corrected the tip twist amplitude, the distribution remained linear and overestimated the 3D wing's J distribution. This stepwise behavior originates from assigning constant J values per section, which coarsely reflects

the smoother stiffness variation of the real wing. To bring the torsion distribution of the beam closer to that of the wing, a quadratic fit was constructed through the original FEM-derived J values and evaluated at 5 mm resolution along the span. The fitted values were then averaged per section, reducing abrupt jumps while retaining the four-segment beam representation. Finally, a global scaling factor was applied to the beam to match the total tip twist:

$$\gamma_y = \frac{\theta_y^{\text{beam,fitted}}}{\theta_y^{\text{FEM}}}. \tag{4.12}$$

Figure 4.27 shows the fitted $J(y)$ curve and the per-section averages, while the resulting global scaling factors are summarized in Table 4.15. Table 4.16 reports the final optimized sectional properties.

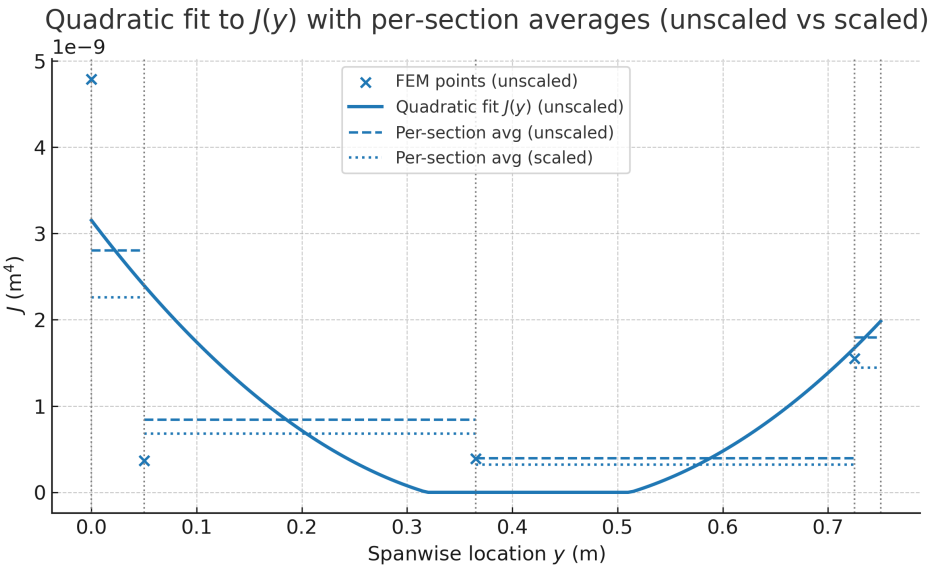

Figure 4.27: Quadratic fit to FEM-derived torsional constant $J(y)$

Load Case	Property	Global Scaling Factor γ
M_x	I_{yy}	1.564
M_y	J	0.805
M_z	I_{zz}	0.888

Table 4.15: Global scaling factors applied to sectional properties

$$I_{yy}^{(j)} = \gamma_x \cdot I_{yy}^{(j)}, \tag{4.13}$$
$$J^{(j)} = \gamma_y \cdot J^{(j)}, \quad j = 1, 2, 3, 4, \tag{4.14}$$
$$I_{zz}^{(j)} = \gamma_z \cdot I_{zz}^{(j)}. \tag{4.15}$$

Section	I_{yy} [m^4]	J [m^4]	I_{zz} [m^4]
1	3.040E-10	2.254E-09	5.422E-08
2	1.999E-10	6.787E-10	4.660E-08
3	2.074E-10	3.196E-10	4.391E-08
4	6.280E-11	1.441E-09	3.681E-08

Table 4.16: Optimized cross-sectional properties for each beam segment

It is essential to note that the stiffness tuning was performed by scaling the second moments of area (I_{yy}, I_{zz}) and the torsional constant (J), rather than directly adjusting the material moduli (E, G). This decision was made because ANSYS requires physically valid material definitions for simulation accuracy and numerical stability. Moreover, scaling geometric cross-sectional properties offers more localized control over stiffness distribution across sections without altering the material model.

After calibration, the scaled properties were reassigned to the beam model, and static analyses were repeated. The optimized tip results are summarized in Table 4.17.

Quantity	Load case	3D Wing	1D Beam	Relative Error
Tip Displacement u_z [m]	M_x	1.881×10^{-2}	1.880×10^{-2}	$\approx 0\%$
Tip Rotation θ_y [rad]	M_y	6.107×10^{-2}	6.107×10^{-2}	$\approx 0\%$
Tip Displacement u_x [m]	M_z	-8.487×10^{-5}	-8.486×10^{-5}	$\approx 0\%$

Table 4.17: Comparison of tip deformation results using optimized cross-sectional properties

To assess the fidelity of the stiffness-optimized 1D beam model, its deformation response was compared against the original 1D beam and the high-fidelity 3D wing model in terms of u_z, u_x, and θ_y.

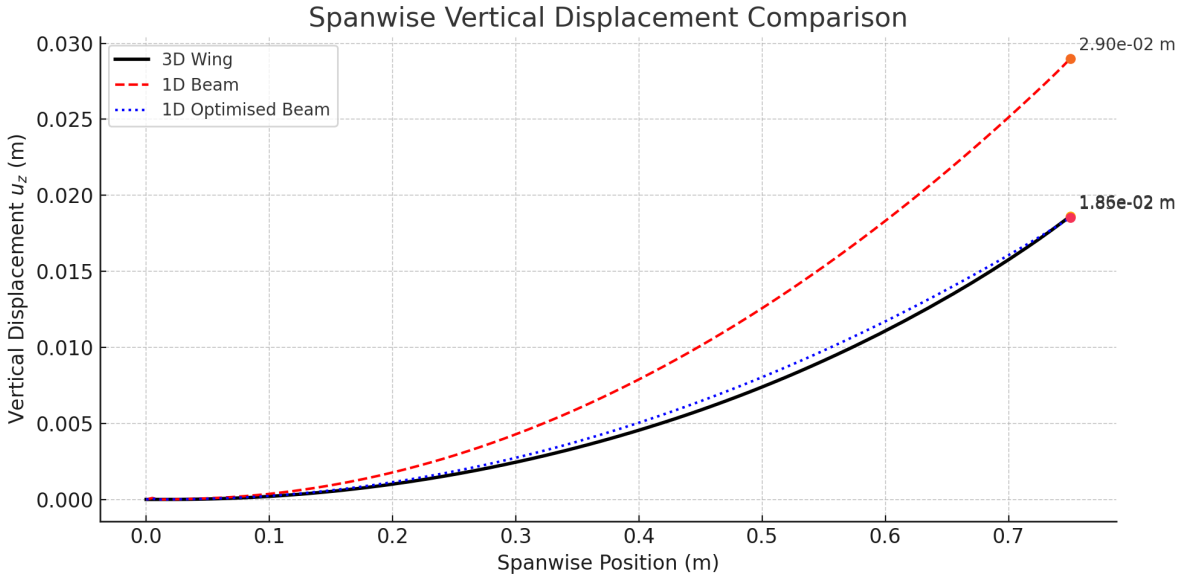

Figure 4.28: Spanwise vertical displacement comparison

From Figure 4.28, the optimized 1D beam and the 3D wing exhibit closely matched vertical deflections with identical deflection amplitudes and similar curvature, with only minor spanwise deviations. The maximum absolute deviation from the 3D wing occurs at $y \approx 0.55\,\text{m}$ (73% span) with $|\Delta u_z| \approx 6.6 \times 10^{-4}\,\text{m}$, corresponding to a local error of 7.4%. At the tip, the optimized beam agrees closely ($9.8 \times 10^{-5}\,\text{m}$, 0.53%). By contrast, the baseline beam shows its most significant error at the tip, overpredicting deflection by $1.0 \times 10^{-2}\,\text{m}$ (55.6%). The deviation of the beams is attributed to residual differences in the spanwise out-of-plane stiffness distribution $EI_x(y)$. Whereas the 3D wing exhibits a continuous stiffness from spar–rib–chassis interactions and local MPC constraints, the 1D beam employs bay-averaged sectional values, which match tip amplitude but not the exact curvature shape.

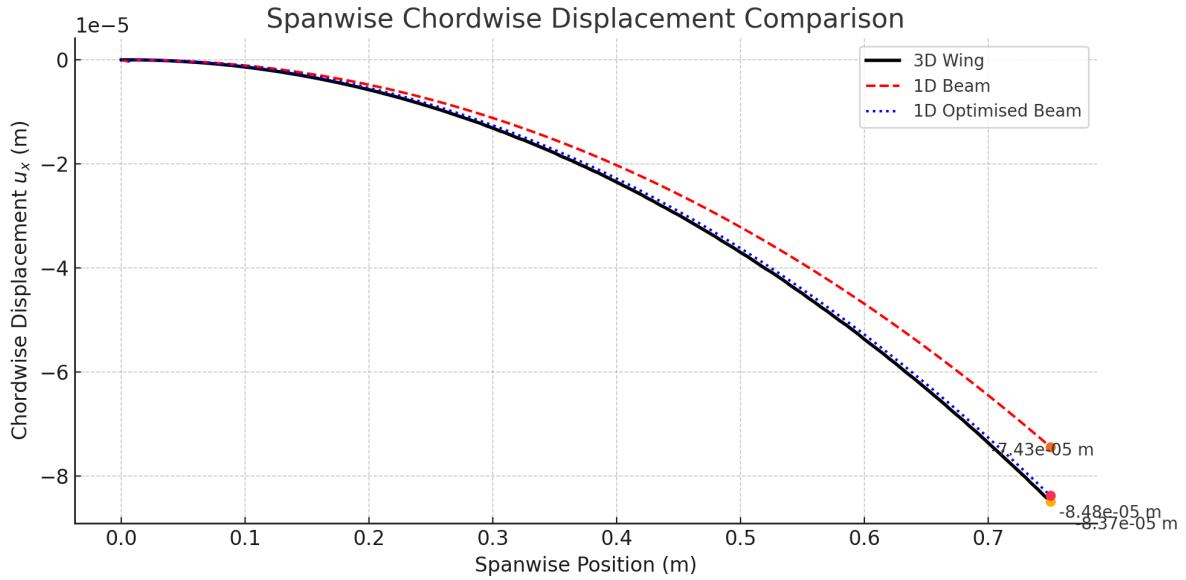

Figure 4.29: Spanwise horizontal displacement comparison

For chordwise displacement from Figure 4.29, the optimized beam again exhibits close agreement with the 3D model. The curvature of the deformation is better preserved compared to the baseline beam, which appears slightly stiffer. The optimized beam shows a maximum deviation of 1.15×10^{-6} m at the tip ($y \approx 0.75$ m), corresponding to $\sim 1.4\%$. The baseline beam exhibits a larger tip error of 1.05×10^{-5} m ($\sim 12.3\%$). Residual differences are attributed to bay-averaged EI_z values and the omission of local rib–chassis interactions, which slightly alter tip compliance in the FEM wing relative to the equivalent beam.

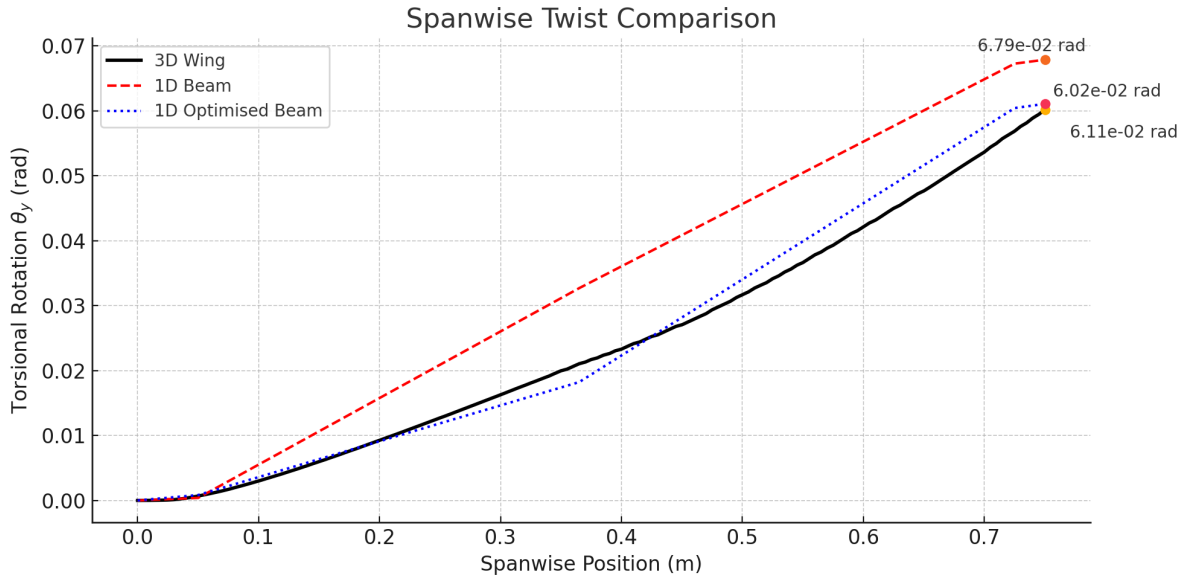

Figure 4.30: Spanwise twist comparison

The most notable improvement appears in the torsional response (θ_y) as seen in Figure 4.30. The original 1D beam significantly overestimates twist, producing a piecewise linear shape indicative of section-wise stiffness discontinuities. In contrast, the optimized model closes the mismatch between the twist amplitude and the smooth curvature observed in the 3D wing. This improvement was achieved by fitting a quadratic spanwise profile to the 3D-extracted torsional stiffness values and scaling it to match the total tip twist. Quantitatively, the optimized beam's maximum deviation is 3.96×10^{-3} rad at

$y \approx 0.66\,\text{m}$ ($\sim 8.2\%$), whereas the baseline beam deviates by 1.40×10^{-2} rad at $y \approx 0.49\,\text{m}$ ($\sim 45.7\%$). The residual difference arises from condensing the smoothly varying torsional stiffness into a quadratic fit, which reduces tip error but cannot fully capture local spanwise variations.

4.6.3. Modal Matching

While static stiffness matching ensures that the 1D segmented beam replicates the 3D FEM wing structure's load–deflection behavior under static conditions, modal matching is equally important for capturing dynamic response in aeroelastic simulations. This subsection outlines the approach used to match the natural frequencies and mode shapes of the equivalent beam to those of the 3D FEM model.

The goal of modal matching is to verify whether the 1D segmented beam, constructed with optimized stiffness and mass properties, reproduces the dominant vibration modes of the 3D FEM wing. Ensuring this agreement in natural frequencies and mode shapes is essential for the beam to capture the structure's dynamic response accurately.

Modal matching builds upon the stiffness-optimized 1D beam constructed in ANSYS. In static analysis, only stiffness governs the deformation response, so density does not play a role. By contrast, mass and inertia directly influence the natural frequencies and mode shapes in modal analysis, making them essential inputs. Each of the four beam segments was assigned optimized cross-sectional stiffnesses and corresponding mass per unit length (μ). In ANSYS Mechanical, cross-sectional definitions via `SECTYPE` inputs do not explicitly support assigning mass or rotational inertia properties. Instead, ANSYS implicitly computed these from the cross-sectional area A and the mass density ρ defined in the material properties. To reflect the varying density of each 3D FEM section, four different materials were created, all assigned a constant E and G, but different densities ρ_i. The density for each segment was calculated using:

$$\rho_i = \frac{m_{\text{section},i}}{\text{V}_{\text{section},i}} \tag{4.16}$$

where $m_{\text{section},i}$ is the total mass and $\text{V}_{\text{section},i}$ is the volume of the material comprising the section i, both extracted from the full 3D FEM model. ANSYS then uses these values to internally compute the total mass and the inertia tensor using the relations:

$$I_{xx} = \int_A \rho z^2\, dA, \quad I_{yy} = \int_A \rho x^2\, dA, \quad I_{zz} = \int_A \rho y^2\, dA \tag{4.17}$$

and similarly for the products of inertia. These are integrated over the assigned cross-section and scaled by density. Table 4.18 summarizes the resulting segment-wise mass properties.

Segment	**Length** [m]	**Mass** [Kg]	**Volume** [m^3]	**Density** [Kg/m^3]	μ [Kg/m]	**A** [m^2]
1	0.050	0.0596	5.055E-05	1178.685	1.192	1.011E-03
2	0.315	0.2099	1.406E-04	1493.172	0.666	4.463E-04
3	0.360	0.2944	1.870E-04	1574.492	0.818	5.194E-04
4	0.025	0.0247	1.587E-05	1556.067	0.988	6.350E-04

Table 4.18: Mass properties of the 1D beam model

To validate the assigned mass properties, modal analysis was performed on the segmented beam. Each segment was defined with its optimized cross-sectional stiffness and density-based mass properties, and the root was fixed to reproduce the wing's clamped–free boundary condition. The first five natural frequencies were extracted, along with the corresponding displacement and torsional mode shapes required for MAC comparisons.

As a preliminary validation step, the modal response of the segmented 1D beam was computed, and the first five natural frequencies were compared to those of the 3D FEM wing model in Table 4.19.

Mode Number	Wing Mode Type	3D Wing [Hz]	1D Beam [Hz]	Beam Mode Type
1	1^{st} Bending	4.24	4.29	1^{st} Bending
2	2^{nd} Bending	21.98	27.91	2^{nd} Bending
3	Torsion	35.84	63.58	Lag Bending
4	3^{rd} Bending	59.59	79.00	3^{rd} Bending
5	Lag Bending	63.14	153.14	4^{th} Bending

Table 4.19: Initial 1D beam modal frequencies

The comparison revealed three main discrepancies. First, the mode order was incorrect: the lag mode appeared as the third mode in the beam instead of the fifth, as observed in the 3D wing. Second, the natural frequencies of the flap modes were consistently higher in the beam model. Finally, the torsional mode was not captured within the extracted range, indicating that it had shifted to higher frequencies. To address these, the following subsection introduces optimization-based modal tuning. The goal is to align the beam's inertia properties with those of the 3D wing structure to better reflect its dynamic response.

Modal Optimization

Observation of the mass properties reported in the `Solution Information` of ANSYS showed that the total mass and the principal inertias I_{xx} and I_{zz} of the 1D beam closely matched those of the 3D wing. However, the polar moment of inertia I_{yy} was significantly underestimated in the beam model, as summarized in Table 4.20.

Inertia [Kg m^2]	3D Wing	1D Beam	Difference	Error %
I_{xx}	0.0294830	0.0298570	-0.00037400	-1.26
I_{yy}	0.0010613	0.0000517	0.00100963	95.13
I_{zz}	0.0305030	0.0299080	0.00059500	1.95

Table 4.20: Comparison of inertia tensor of 3D wing and 1D beam

To address this discrepancy, a correction strategy based on `Point Masses` was introduced. These were positioned at the spanwise center of each of the four beam sections and assigned negligible translational mass. Instead, each point mass was given a rotational inertia I_{yy} equal to one quarter of the missing polar moment, namely

$$I_{yy,each} = \frac{0.00100963}{4} = 0.000252408 \quad \text{Kg m}^2 \tag{4.18}$$

and directly attached to the corresponding beam node. The point masses were placed at the spanwise midpoints of each beam segment to distribute the additional torsional inertia evenly along the span and avoid artificial concentration at the tip. This placement reflects a standard lumped-parameter modeling practice intended to adjust torsional dynamic properties with minimal side effects on bending, rather than the outcome of a dedicated sensitivity study. Figure 4.31 illustrates the placement of these point masses along the 1D beam.

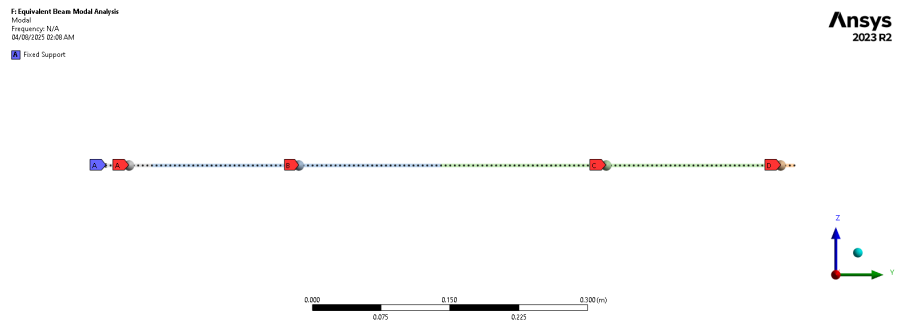

Figure 4.31: Point masses along the 1D beam span

With the difference in I_{yy} added, the modal analysis was rerun, and the updated mass properties of the 1D beam model were as follows:

`Total Mass` $= 0.58861$ Kg

`The mass principal axes coincide with the global Cartesian axes`

`Center of Mass (X,Y,Z)` $= \quad (0.0000, \quad 0.38008, \quad 0.0000)$

`Total Inertia about Center of Mass :`

$$\begin{matrix} 0.29864E-01 & 0.0000 & 0.0000 \\ 0.0000 & 0.10616E-02 & 0.0000 \\ 0.0000 & 0.0000 & 0.29915E-01 \end{matrix}$$

This correction of I_{yy} inertia lowered the torsion frequency to 32.21 Hz. The relation governs the torsional natural frequency f of a beam:

$$f = \sqrt{\frac{GJ}{I_{\text{yy}}}} \tag{4.19}$$

With I_{yy} now matched to the 3D FEM wing via point masses, the torsional frequency can be controlled using an optimization factor. To shift the torsional frequency from its current value f_{current} to a desired target value f_{target}, the necessary scaling factor for I_{yy} is computed from:

$$\frac{I_{\text{yy,current}}}{I_{\text{Iyy,new}}} = \left(\frac{f_{\text{target}}}{f_{\text{current}}}\right)^2 \tag{4.20}$$

Thus, the updated I_{yy} inertia is:

$$I_{\text{Iyy,new}} = I_{\text{yy,current}} \left(\frac{f_{\text{current}}}{f_{\text{target}}}\right)^2 \tag{4.21}$$

Thus for:

$$f_{\text{target,wing}} = 35.84 \text{ Hz}$$
$$f_{\text{current,beam}} = 32.21 \text{ Hz}$$

$$\Rightarrow \quad \text{Scaling Factor} = \left(\frac{32.21}{35.84}\right)^2 \approx 0.808 \tag{4.22}$$

The torsional mass moment of inertia I_{yy} for all four beam segments was therefore multiplied by this factor to raise the torsional frequency to the desired value as follows:

$$I_{\text{yy}}^{(j)} = 0.808 \cdot I_{\text{yy}}^{(j)} \quad \text{for sections } j = 1, 2, 3, 4 \tag{4.23}$$
$$\therefore 0.000252408 \times 0.808 = 0.000203957 \quad \text{Kg m}^2 \tag{4.24}$$

With torsional mass moment of inertia I_{yy} scaled, the attention shifts to aligning out-of-plane bending frequencies. While mode shapes for these bending modes were qualitatively correct, their frequencies remained high, especially for higher-order flap modes. To achieve a modal match between the 1D segmented beam model and the full 3D wing structure, an iterative refinement of the out-of-plane inertia I_{xx} per segment was adjusted using a global scaling approach. Starting from a base model with optimized section-wise stiffness but no rotational inertia, the inertias were incrementally added to each `Point Mass` located at the beam segment centers.

Through iterative tuning, a uniform value of I_{xx} per segment was identified that brought the first, second, and third flap bending frequencies within ±10% of the corresponding 3D wing modes. This process was guided by the general inverse square frequency–inertia relationship:

$$f \propto \frac{1}{\sqrt{I_{\text{xx}}}} \tag{4.25}$$
$$I_{xx,each} = 0.0007 \quad \text{Kg m}^2 \tag{4.26}$$

which ensured that frequency reductions were achieved by increasing out-of-plane rotational inertia uniformly. This global tuning approach allowed frequency matching while preserving mode shapes. This approach resulted in excellent agreement between the beam and wing modal responses as presented in Table 4.21, with all five target modes appearing in correct order and frequency deviations under 9%.

Mode Number	**3D Wing** [Hz]	**1D Beam** [Hz]	Error [%]
1	4.24	4.21	−0.58
2	21.98	23.63	+7.48
3	35.84	35.67	0
4	59.59	55.79	–6.37
5	63.14	63.57	1

Table 4.21: Initial 1D beam modal frequencies

The final, tuned inertia properties of the 1D beam are obtained from ANSYS as follows:

`Total Mass` $= 0.58861$ Kg

`The mass principal axes coincide with the global Cartesian axes`

`Center of Mass (X,Y,Z)` $= (0.0000, \quad 0.38008, \quad 0.0000)$

`Total Inertia about Center of Mass :`

$$\begin{matrix} 0.32657E-01 & 0.0000 & 0.0000 \\ 0.0000 & 0.86749E-03 & 0.0000 \\ 0.0000 & 0.0000 & 0.29908E-01 \end{matrix}$$

To interpret the deformation data consistently across modes, the effective modal mass participation in each X, Y, and $ROTY$ direction is computed using data obtained from `Solution Information` found in Appendix A.6. Using equation 4.2, the participation of effective modal mass in the dominant direction for each mode for both the 3D wing and 1D beam is compared and tabulated in Table 4.22 below.

Mode Number	**Dominant Direction**	**3D Wing Mass** [%]	**1D Beam Mass** [%]	**Mode Type**
1	Z	61.62	58.32	Flap Bending
2	Z	15.00	15.56	2^{nd} Flap Bending
3	ROTY	0.132	0.09	Torsion
4	Z	5.33	3	3^{rd} Flap Bending
5	X	61.24	61.04	Lag bending

Table 4.22: DOF participation for 1D beam modes

To visualize the mode shapes, the modal deformations along the span were plotted using the raw spanwise deformation datasets in Figure 4.34. The raw modal DOF deformation dataset of the 1D beam model can be found in the Appendix A.7.

Modal Assurance Criteria Validation

Following the optimization of the modal frequencies, the Modal Assurance Criterion (MAC) is employed to verify the fidelity of the 1D beam in replicating the wing's dynamic behavior and to quantify the similarity between their mode shapes. The MAC between two mode shape vectors ϕ_i and ψ_j is defined as:

$$\text{MAC}(\phi_i, \psi_j) = \frac{\left|\phi_i^T \psi_j\right|^2}{\left(\phi_i^T \phi_i\right)\left(\psi_j^T \psi_j\right)} \tag{4.27}$$

where ϕ_i is the i-th mode shape vector from the 3D FEM wing and ψ_j is the j-th mode shape vector from the 1D equivalent beam. The MAC value ranges from 0 (no correlation) to 1 (perfect correlation),

and values above 0.9 are generally considered strong matches in structural dynamics [12].

The 1D beam's and 3D wing's spanwise deformation components u_x, u_z, and θy were extracted. These raw modal displacements were multiplied by their effective modal mass ratio m_{eff}/m_w to scale the relative amplitudes of the displacement components. To ensure accurate and comparable MAC values between the two models, the DOFs were stacked into a single vector following the order: $[u_x;u_z;\theta_y]$ and normalized once using its Euclidean norm:

$$v_{\text{norm}} = \frac{v}{||v||_2} \tag{4.28}$$

where v_{norm} is the stacked, normalized vector, v is the modal effective modal mass ratio-scaled, stacked vector for each mode of the 3D wing and the 1D beam models. The resulting MAC matrix comparing the first five modes of the two models is shown as a heat map in Figure 4.32. Additionally, the $\text{MAC}_{\text{beam-beam}}$ and $\text{MAC}_{\text{wing-wing}}$ matrix heatmaps were plotted in Figure 4.33

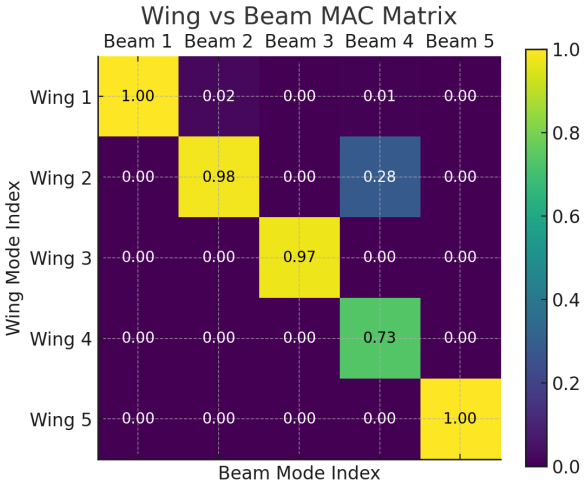

Figure 4.32: 3D wing vs 1D beam MAC matrix heatmap

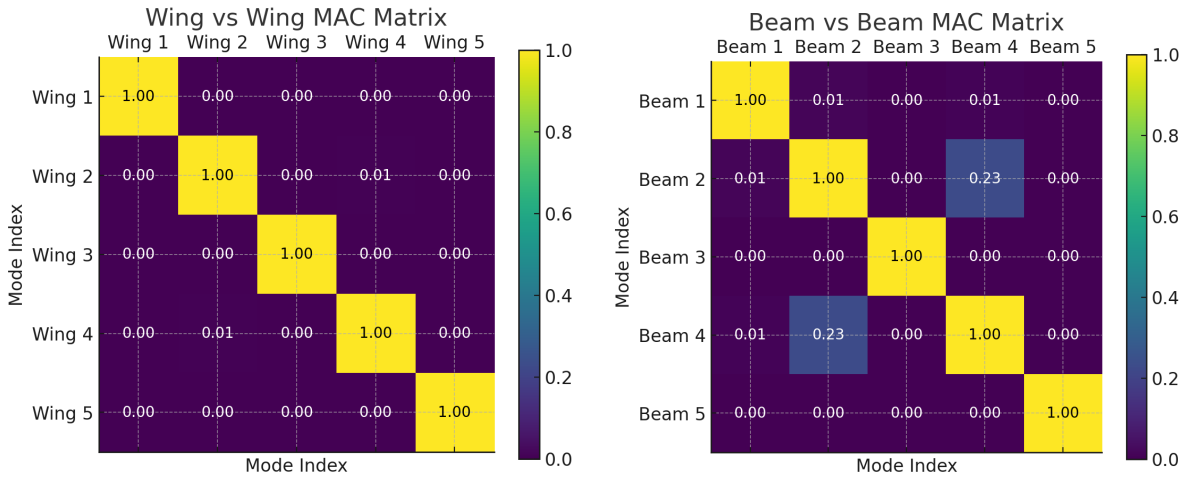

(a) 3D wing vs 3D wing MAC matrix heatmap

(b) 1D beam vs 1D beam MAC matrix heatmap

Figure 4.33: Orthogonal MAC matrices

The $\text{MAC}_{\text{wing-wing}}$ confirms perfect orthogonality of the 3D FEM reference model. In contrast, the $\text{MAC}_{\text{beam-beam}}$ shows a modest internal correlation between Modes 2 and 4 (≈ 0.23), indicating partial

overlap among the second- and third-bending modes within the beam basis. Notably, the $\text{MAC}_{\text{wing-beam}}$ exhibits strong diagonal values (> 0.97) for four of the five mode pairs, confirming excellent shape correlation of the equivalent beam with the FEM wing. The exception is Mode 4 (third bending), where the diagonal entry is reduced to **0.73**. This lower value, along with the off-diagonal term of ≈ 0.28 between Wing Mode 2 and Beam Mode 4, demonstrates that the simplified 1D beam does not separate the higher-order bending modes as cleanly as the FEM wing. This limitation is confined to higher-order dynamics and arises from the reduced structural fidelity of the beam abstraction rather than errors in stiffness or inertia extraction. The equivalent beam reproduces the primary modal content well, with only a notable but acceptable degradation in the third-bending correspondence.

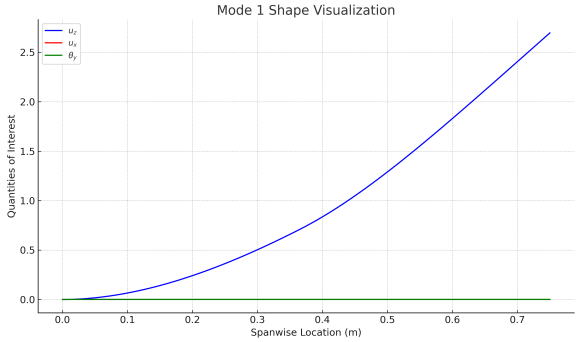

(a) Mode 1 shape

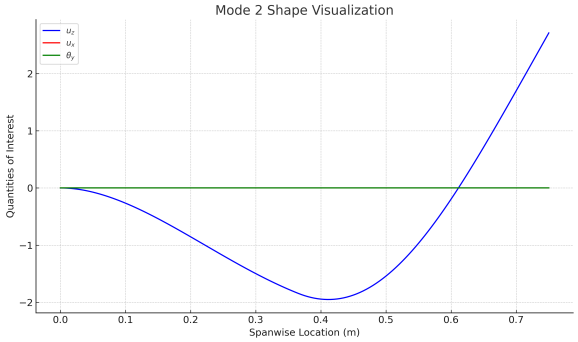

(b) Mode 2 shape

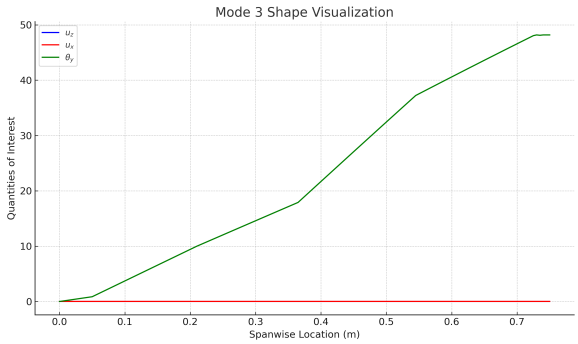

(c) Mode 3 shape

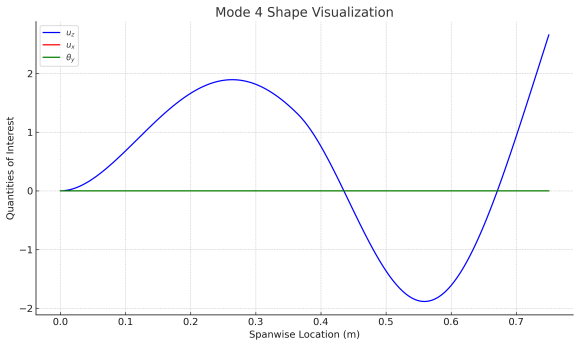

(d) Mode 4 shape

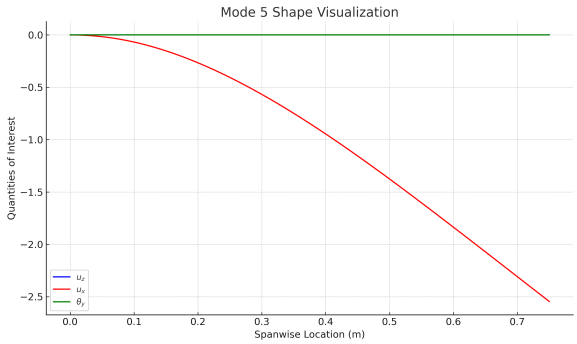

(e) Mode 5 shape

Figure 4.34: 1D beam modal spanwise deformation profile visualization for each mode

5

Conclusion

This thesis aimed to design a flexible aircraft model for wind tunnel free-flight testing and to develop its equivalent beam representation as a validated numerical model for increased-fidelity aeroelastic analysis. Three sub-questions guided the research, each answered below.

What level of fidelity is required for a flexible aircraft model to exhibit aeroelastic effects while being suitable for free-flight wind tunnel testing?
The design study resulted in a 0.75 m span rectangular wing configuration tailored for TU Delft's Open Jet Facility. Literature-driven insights, combined with wind tunnel constraints, guided the selection of geometry, material properties, and internal layout to ensure structural compliance and experimental feasibility. The chosen geometry balances structural simplicity with sufficient flexibility to exhibit measurable gust-induced deformations. This ensures that the wing is experimentally feasible and can display representative aeroelastic effects. The outcome confirms that a relatively simple structural layout can provide the required fidelity for free-flight gust testing while remaining compatible with fabrication and facility constraints. The resulting design also served as the basis for the finite element model used to extract structural properties in the subsequent phase.

How can the structural dynamic properties of the aircraft be represented by an equivalent beam model that reflects its main stiffness and inertia properties?
A finite element model of the wing was developed in ANSYS to extract stiffness and inertia characteristics. Sectional variation in bending stiffness, torsional stiffness, and mass properties was quantified by partitioning the wing into four bays. These sectional properties formed the basis for an equivalent four-segment one-dimensional beam. The beam was parameterized by assigning sectional stiffnesses and mass distributions, enabling the construction of a reduced-order representation that directly reflects the wing's spanwise structural characteristics.

How can the equivalent beam model be validated to ensure it reproduces the main structural characteristics of the aircraft?
Validation was achieved through comparative static and modal analyses. Initially, the beam underestimated bending and torsional responses, but tuning of stiffness parameters improved agreement with the finite element wing's spanwise deformation. Modal analysis revealed frequency mismatches, which were corrected by refining distributed rotational inertias. The final tuned beam accurately reproduced the finite element wing's natural frequencies and deformation patterns. This was confirmed through a Modal Assurance Criterion analysis, which yielded a near-diagonal matrix and demonstrated strong correlation between mode shapes of the two models. This indicates that the simplified beam reproduces the dominant modal content well, with only minor limitations in separating higher-order bending modes. The simplified beam retains the essential dynamic content of the detailed wing model, providing a reliable foundation for its use in aeroelastic simulations.

The main conclusion of this thesis is that the combined design of a feasible flexible aircraft and the numerical validation of its equivalent beam representation establishes a practical and reliable base

for increased-fidelity aeroelastic testing. The design phase ensured that the plane can exhibit meaningful aeroelastic effects while remaining compatible with wind tunnel free-flight constraints, and the reduced-order beam model provides a computationally efficient representation that accurately reflects its structural dynamics. Together, these outcomes bridge detailed finite element modeling and the requirements of real-time aeroelastic simulations, enabling future gust response analyses and supporting the development of hybrid wind tunnel methodologies at TU Delft.

Limitations

While the equivalent beam model successfully replicated the static and dynamic behavior of the finite element wing, several limitations remain. First, the validation process relied on stiffness tuning and inertia adjustments to match modal frequencies, introducing dependence on calibration rather than a purely predictive model. Second, the structural representation was restricted to four spanwise segments, which captures overall trends but may smooth out finer variations in stiffness distribution. Third, the aerodynamic environment has not yet been coupled to the structural model; as a result, aeroelastic effects under gust excitation were not directly simulated within this work. Finally, the study was limited to numerical modeling, and no physical prototype was manufactured or tested, meaning that practical considerations such as fabrication tolerances and material nonlinearities remain unverified.

Future Work

The next step is implementing the validated beam model in SHARPy to conduct gust response simulations. This will allow the flexible aircraft to be analyzed in a coupled aeroelastic framework and provide numerical motion profiles that can be prescribed in hybrid wind tunnel tests. Beyond this, several directions exist for extending the research. Increasing the resolution of the beam segmentation could capture local stiffness variations more accurately. Experimental validation, fabrication, and free-flight testing of the designed wing in the Open Jet Facility are essential to confirm the numerical findings. Incorporating unsteady aerodynamics and nonlinear structural effects within the SHARPy framework would further enhance the fidelity of the simulations. Ultimately, combining the validated beam with hybrid testing methods offers a pathway toward more reliable gust load prediction and improved aeroelastic investigation strategies for future flexible aircraft.

References

[1] T. E. Noll *et al.*, "Technical findings, lessons learned, and recommendations resulting from the helios prototype vehicle mishap," in *NATO/RTO AVT-145 Workshop on Design Concepts, Processes and Criteria for UAV Structural Integrity*, 2007.

[2] J. Sodja and R. D. Breuker, "Design of an increased-fidelity aeroelastic experiment for wing response to gust excitation," in *AIAA SCITECH 2022 Forum*, American Institute of Aeronautics and Astronautics, Jan. 2022, ISBN: 978-1-62410-631-6. DOI: 10.2514/6.2022-2418.

[3] Z. Wu, Y. Cao, and M. Ismail, "Gust loads on aircraft," *The Aeronautical Journal*, vol. 123, no. 1266, pp. 1216–1274, 2019. DOI: 10.1017/aer.2019.48.

[4] EASA, *Cs-25: Certification specifications for large aeroplanes*, Dec. 2009. [Online]. Available: https://www.easa.europa.eu/en/document-library/certification-specifications/cs-25-amendment-8#group-easa-related-content.

[5] F. A. Admininstration, *25.341 airworthiness standards: Transport category airplanes - dynamic gust loads*, Dec. 2014. [Online]. Available: https://www.faa.gov/documentLibrary/media/Advisory_Circular/AC_25_341-1.pdf.

[6] F. M. Hoblit, *Gust Loads on Aircraft: Concepts and Applications*. American Institute of Aeronautics and Astronautics, Jan. 1988, ISBN: 978-0-930403-45-4. DOI: 10.2514/4.861888. [Online]. Available: https://arc.aiaa.org/doi/book/10.2514/4.861888.

[7] M. J. Patil and D. H. Hodges, "Flight dynamics of highly flexible flying wings," *Journal of Aircraft*, vol. 43, no. 6, pp. 1790–1799, 2006. DOI: 10.2514/1.17640.

[8] D. McLean, *Aircraft Flight Dynamics and Control*. American Institute of Aeronautics and Astronautics, 1990.

[9] MATLAB, *Dryden wind turbulence model (continuous)*. [Online]. Available: https://nl.mathworks.com/help/aeroblks/drydenwindturbulencemodelcontinuous.html.

[10] MATLAB, *Von karman wind turbulence model (continuous)*. [Online]. Available: https://nl.mathworks.com/help/aeroblks/vonkarmanwindturbulencemodelcontinuous.html.

[11] J. Fuller, "Evolution of airplane gust loads design requirements," *Journal of Aircraft*, vol. 32, no. 2, pp. 235–246, 1995.

[12] C. Howcroft *et al.*, "Aeroelastic modelling of highly flexible wings," American Institute of Aeronautics and Astronautics, Jan. 2016, ISBN: 978-1-62410-398-8. DOI: 10.2514/6.2016-1798.

[13] A. del Carre, A. Muñoz-Simón, N. Goizueta, and R. Palacios, "Sharpy: A dynamic aeroelastic simulation toolbox for very flexible aircraft and wind turbines," *Journal of Open Source Software*, vol. 4, no. 44, p. 1885, 2019. DOI: 10.21105/joss.01885. [Online]. Available: https://doi.org/10.21105/joss.01885.

[14] A. Del Carre De La Portilla, "Aeroelasticity of very flexible aircraft at low altitudes," 2020. DOI: 10.25560/88269. [Online]. Available: http://spiral.imperial.ac.uk/handle/10044/1/88269.

[15] J. Murua, M. B. Giles, and R. Palacios, "Time-domain aeroelastic modeling and simulation of complete aircraft configurations for control applications," *AIAA Journal*, vol. 50, no. 12, pp. 2739–2751, 2012. DOI: 10.2514/1.J051642.

[16] J. Murua, "'flexible aircraft dynamics with a geometrically-nonlinear description of the unsteady aerodynamics'," Ph.D. dissertation, Imperial College London, 2012.

[17] R. J. S. Simpson, R. Palacios, and J. Murua, "Induced-drag calculations in the unsteady vortex lattice method," *AIAA Journal*, vol. 51, no. 7, pp. 1775–1779, 2013. DOI: 10.2514/1.J052136. eprint: https://doi.org/10.2514/1.J052136. [Online]. Available: https://doi.org/10.2514/1.J052136.

[18] H. Hesse and R. Palacios, “Reduced-order aeroelastic models for dynamics of maneuvering flexible aircraft,” *AIAA Journal*, vol. 52, no. 8, pp. 1717–1732, 2014. DOI: 10.2514/1.J052684. eprint: https://doi.org/10.2514/1.J052684. [Online]. Available: https://doi.org/10.2514/1.J052684.

[19] I. C. London, *Sharpy user manual – case file structure*, https://ic-sharpy.readthedocs.io, Imperial College London Aeroelasticity Lab, 2024.

[20] F. Palacios, J. J. Alonso, J. E. Hicken, and C. Farhat, “State-of-the-art and challenges in high-fidelity aeroelastic simulations,” *Computers & Fluids*, vol. 158, pp. 279–298, 2017.

[21] F. Huvelin, S. Dequand, A. Lepage, and C. Liauzun, “On the validation and use of high-fidelity numerical simulations for gust response analysis,” *AerospaceLab Journal*, vol. Issue 14, September 2018, ISSN: 2107–6596, 2018. DOI: 10.12762/2018.AL14-06. [Online]. Available: https://aerospacelab.onera.fr/sites/www.aerospacelab-journal.org/files/AL14-06_0.pdf.

[22] Y. Liu, J. J. Alonso, and H. van der Ven, “Hybrid rbf–ale framework for time-accurate aeroelastic gust response using su2 and abaqus,” in *AIAA SciTech Forum*, American Institute of Aeronautics and Astronautics, 2015, AIAA 2015–1234.

[23] W. Krüger, “Multibody dynamics for the coupling of aeroelasticity and flight mechanics of highly flexible structures,” Jan. 2007.

[24] Z. Zhao and G. Ren, “Multibody dynamic approach of flight dynamics and nonlinear aeroelasticity of flexible aircraft,” *AIAA Journal*, vol. 49, pp. 41–54, Jan. 2011. DOI: 10.2514/1.45334.

[25] J. D. Connelly and R. L. Huston, “The dynamics of flexible multibody systems: A finite segment approach i: Theoretical aspects.,” *Computers & Structures*, vol. 50, pp. 225–258, 1994. [Online]. Available: https://www.academia.edu/26637139/The_dynamics_of_flexible_multibody_systems_A_finite_segment_approach_I_Theoretical_aspects.

[26] C. W. Gear, “Numerical initial value problems in ordinary differential equations,” *Prentice-Hall series in automatic computation*, 1971.

[27] P. Gonzalez, G. Starvorinus, F. J. Silvestre, A. Voß, Y. M. Meddaikar, and W. Krueger, “Tu-flex: A very-flexible flying demonstrator with a generic transport aircraft configuration,” American Institute of Aeronautics and Astronautics, Jan. 2023, ISBN: 978-1-62410-699-6. DOI: 10.2514/6.2023-1312. [Online]. Available: https://arc.aiaa.org/doi/10.2514/6.2023-1312.

[28] M. Bras, S. Warwick, and A. Suleman, “Aeroelastic evaluation of a flexible high aspect ratio wing uav: Numerical simulation and experimental flight validation,” *Aerospace Science and Technology*, vol. 122, p. 107 400, Mar. 2022, ISSN: 12709638. DOI: 10.1016/j.ast.2022.107400. [Online]. Available: https://linkinghub.elsevier.com/retrieve/pii/S1270963822000748.

[29] H. H. Khodaparast, “Efficient worst case 1-cosine gust loads prediction,” 2012. [Online]. Available: https://api.semanticscholar.org/CorpusID:58902894.

[30] W. Jianfeng, L. Shiguang, F. Shuai, and W. Minghui, *Free flight test in horizontal wind tunnel with powered aircraft - icas*, 2022. [Online]. Available: https://icas.org/ICAS_ARCHIVE/ICAS2022/data/papers/ICAS2022_0423_paper.pdf.

[31] L. Q. Cen F., L. Z.-T. Nie B.-W., and S. H.-S., “Wind tunnel free-flight test for flight dynamics and control system experiments,” 2016. [Online]. Available: https://icas.org/ICAS_ARCHIVE/ICAS2016/data/papers/2016_0091_paper.pdf.

[32] D. Kubo, “Gust response evaluation of small uas via free-flight in gust wind tunnel,” in *2018 AIAA Atmospheric Flight Mechanics Conference*, 2018, p. 0297.

[33] B. Gjerek, R. Drazumeric, and F. Kosel, “A novel experimental setup for multiparameter aeroelastic wind tunnel tests,” *Experimental Techniques*, vol. 38, no. 6, pp. 30–43, 2014. DOI: https://doi.org/10.1111/j.1747-1567.2012.00839.x. eprint: https://onlinelibrary.wiley.com/doi/pdf/10.1111/j.1747-1567.2012.00839.x. [Online]. Available: https://onlinelibrary.wiley.com/doi/abs/10.1111/j.1747-1567.2012.00839.x.

[34] Y. MENG, Z. WAN, C. XIE, and C. AN, “Time-domain nonlinear aeroelastic analysis and wind tunnel test of a flexible wing using strain-based beam formulation,” *Chinese Journal of Aeronautics*, vol. 34, pp. 380–396, 1 Jan. 2021, ISSN: 10009361. DOI: 10.1016/j.cja.2020.07.027.

[35] O. Avin, D. E. Raveh, A. Drachinsky, Y. Ben-Shmuel, and M. Tur, “Experimental aeroelastic benchmark of a very flexible wing,” *AIAA Journal*, vol. 60, pp. 1745–1768, 3 Mar. 2022, ISSN: 0001-1452. DOI: 10.2514/1.J060621.

[36] C. Mertens, J. Sodja, A. Sciacchitano, and B. van Oudheusden, “Experimental aeroelastic characterization of a very flexible wing in steady and unsteady inflow,” American Institute of Aeronautics and Astronautics, Jan. 2022, ISBN: 978-1-62410-631-6. DOI: 10.2514/6.2022-1344.

[37] J. Ballmann, “Experimental analysis of high reynolds number structural dynamics in etw,” in *46th AIAA Aerospace Sciences Meeting and Exhibit*. DOI: 10.2514/6.2008-841. eprint: https://arc.aiaa.org/doi/pdf/10.2514/6.2008-841. [Online]. Available: https://arc.aiaa.org/doi/abs/10.2514/6.2008-841.

[38] W. Vink and J. de Jonge, *A matlab program to study gust loading on a simple aircraft model*, Jan. 1997. [Online]. Available: http://resolver.tudelft.nl/uuid:1ab422a0-23f9-4886-824d-a9a84eef4184.

[39] D. Tang, A. Grasch, and E. H. Dowell, “Gust response for flexibly suspended high-aspect ratio wings,” *AIAA Journal*, vol. 48, pp. 2430–2444, 10 Oct. 2010, ISSN: 0001-1452. DOI: 10.2514/1.J050309.

[40] M. Patil and D. Taylor, “Gust response of highly flexible aircraft,” in *47th AIAA/ASME/ASCE/AHS/ASC Structures, Structural Dynamics, and Materials Conference 14th AIAA/ASME/AHS Adaptive Structures Conference 7th*, 2006, p. 1638.

[41] “Open jet facility.” (2025), [Online]. Available: https://www.tudelft.nl/lr/organisatie/afdelingen/flow-physics-and-technology/facilities/low-speed-wind-tunnels/open-jet-facility.

[42] P. M. Lancelot, J. Sodja, N. P. Werter, and R. D. Breuker, “Design and testing of a low subsonic wind tunnel gust generator,” *Advances in aircraft and spacecraft science*, vol. 4, no. 2, pp. 125–144, 2017. DOI: 10.12989/aas.2017.4.2.125.

[43] S. D, *Aircraft Design*. Hamburg University of Applied Sciences, 2015. [Online]. Available: http://LectureNotes.AircraftDesign.org..

[44] D. P. Raymer, *Aircraft design : a conceptual approach*. AIAA, 2018, ISBN: 9781624104909. DOI: 10.2514/4.104909.

[45] C. P. Fagley, J. Seidel, and T. E. McLaughlin, “Experimental investigation of the aeroelastic behavior a naca0018 cyber-physical flexiblewing,” *33rd AIAA Applied Aerodynamics Conference*, 2015. DOI: 10.2514/6.2015-2251.

[46] C. P. Fagley, J. Seidel, and T. E. McLaughlin, “Aeroelastic response of a finite span naca 0018 wing part 2: Computational simulations,” *53rd AIAA Aerospace Sciences Meeting*, 2015. DOI: 10.2514/6.2015-0250.

[47] T. E, “Aerodynamic performance of wing-body configurations and the flying wing,” 1991, pp. 158–163. [Online]. Available: https://www.jstor.org/stable/44547589.

[48] R. Martínez-Val and E. Schoep. “Flying wing versus conventional transport airplane: The 300 seat case - icas.” (2000), [Online]. Available: http://icas.org/ICAS_ARCHIVE/ICAS2000/PAPERS/ICA0113.PDF.

[49] T. E, *From Tube and Wing to Flying Wing*. Wiley, Jun. 2013, pp. 121–155. DOI: 10.1002/9781118568101.ch5.

[50] P. Mahamuni, A. Kulkarni, and Y. Parikh, “Aerodynamic study of blended wing body,” vol. 9, pp. 29 247–29 255, Jan. 2014.

[51] D. J. Peery and J. Azar, “Aircraft structures,” *The Aeronautical Journal*, vol. 86, no. 860, 2016. DOI: 10.1017/S0001924000019308.

[52] D. Schmidt, “Equations of motion of the rigid vehicle,” in *Modern Flight Dynamics*. 2023, ch. Chapter 2, pp. 48–58. DOI: 10.2514/5.9781624106170.0027.0086.

[53] M. J. Abzug and E. E. Larrabee, “Managing control forces,” in *Airplane Stability and Control: A History of the Technologies that Made Aviation Possible* (Cambridge Aerospace Series), 2nd ed., Cambridge Aerospace Series. Cambridge University Press, 2002, pp. 72–74. DOI: 10.1017/CBO9780511607141.007.

[54] P. C. Teixeira and C. E. S. Cesnik, “Propeller effects on the response of high-altitude long-endurance aircraft,” *AIAA Journal*, vol. 57, no. 10, pp. 4328–4342, 2019. DOI: 10.2514/1.J057575.

[55] T. Bouquet and R. Vos, “Modeling the propeller slipstream effect on lift and pitching moment,” American Institute of Aeronautics and Astronautics, Jan. 2017, ISBN: 978-1-62410-447-3. DOI: 10.2514/6.2017-0236.

[56] *Esdu 89047: In-plane forces and moments on installed inclined propellers at low forward speeds.* 2016. [Online]. Available: https://www.esdu.com/cgi-bin/ps.pl?sess=unlicensed_1231019074936zcj&t=doc&p=esdu_89047e.

[57] “7075 aluminium alloy.” (2025), [Online]. Available: https://www.fergusonperf.com/the-perforating-process/material-information/specialized-aluminum/7075-aluminium-alloy/.

[58] “3d printed nylon12.” (2025), [Online]. Available: https://www.xometry.com/capabilities/3d-printing-service/3d-printing-nylon/.

[59] “Introduction to contact.” (2020), [Online]. Available: https://innovationspace.ansys.com/courses/wp-content/uploads/sites/5/2019/05/2.5.1-Introduction-on-contact_New_Template_Master.pdf.

[60] M. S. A. Elsayed, R. Sedaghati, and M. Abdo, “Accurate stick model development for static analysis of complex aircraft wing-box structures,” *AIAA Journal*, vol. 47, no. 9, pp. 2063–2075, 2009. DOI: 10.2514/1.38447. [Online]. Available: https://doi.org/10.2514/1.38447.

[61] “Bluebird model micro servo.” (2025), [Online]. Available: https://www.blue-bird-model.com/products_detail/74.htm.

A

Appendix A

A.1. PSD Model Comparison Plot

This Python script generates a comparison plot of Power Spectral Density (PSD) curves for the longitudinal and vertical turbulence components of the Dryden and von Kármán stochastic gust models.

Assumptions and Settings

- Airspeed: $V = 50$ m/s (moderate flight speed).
- Scale lengths, $L_u^{\text{(longitudinal)}}$ = 200 m, $L_w^{\text{(vertical)}}$ = 100 m.
- Turbulence intensities, $\sigma_u^{\text{(longitudinal)}}$ = 1.0, $\sigma_w^{\text{(vertical)}}$ = 1.0.
- Frequency range, $\omega = 0.01 - 10$ rad/s

```python
import numpy as np
import matplotlib.pyplot as plt

# === Model parameters ===
omega = np.linspace(0.01, 10, 1000)  # Frequency range [rad/s]
V = 50       # Airspeed [m/s]
Lu = 200     # Longitudinal scale length [m]
Lw = 100     # Vertical scale length [m]
sigma_u = 1.0  # Longitudinal turbulence intensity
sigma_w = 1.0  # Vertical turbulence intensity

# === Dryden PSD equations ===
Phi_u_dryden = (2 * sigma_u**2 * Lu / (np.pi * V)) * (1 / (1 + (Lu * omega / V)**2))
Phi_w_dryden = (2 * sigma_w**2 * Lw / (np.pi * V)) * ((1 + 3 * (Lw * omega / V)**2) / (1 + (
    Lw * omega / V)**2)**2)

# === von Kármán PSD equations ===
Phi_u_vk = (2 * sigma_u**2 * Lu / (np.pi * V)) * ((1 + (1.339 * Lu * omega / V)**2)**(-5/6))
Phi_w_vk = (2 * sigma_w**2 * Lw / (np.pi * V)) * ((1 + (1.339 * Lw * omega / V)**2)**(-11/6))

# === Plotting ===
plt.figure(figsize=(10, 6))
plt.plot(omega, Phi_u_dryden, label='Dryden Longitudinal', linestyle='--')
plt.plot(omega, Phi_w_dryden, label='Dryden Vertical', linestyle='--')
plt.plot(omega, Phi_u_vk, label='von Kármán Longitudinal', linestyle='-')
plt.plot(omega, Phi_w_vk, label='von Kármán Vertical', linestyle='-')
plt.xlabel('Frequency  [rad/s]')
plt.ylabel('PSD Φ () [arbitrary units]')
plt.title('Comparison of Dryden and von Kármán PSD Models')
plt.legend()
plt.grid(True)
plt.tight_layout()
plt.show()
```

A.2. Point Mass Calculations

The calculations are detailed to determine the mass distribution and global CG of the point masses. The X, Y, Z coordinates for the point masses and the volumes of the structures were determined using the 3D Wing assembly in Ansys SpaceClaim 2023 R2 using the `Measure` tool.

Servo

Mass of servo = 7.4 ± 0.5 g [61] (8 g considered for analysis)
Centre of Volume = (48.8, 524.3, 0) mm

Aileron

Total volume of aileron = 23734 mm^3
Centre of Volume = (94, 544.7, 0) mm
Density of Nylon 12 = 930 kg/m3
$\therefore$ Mass of aileron $\approx$ 22 g

Since the aileron spans over six ribs, the mass will be equally distributed along the same.
$\Rightarrow$ each point mass of aileron = 22/6 = 3.67 g

The y-coordinate of each rib's trailing face centroid was found using the `Node Selection` filter in Ansys Mechanical. Since the aileron spans along the Y axis, the X and Z coordinates of the point masses will remain constant.

- Aileron1 = (94, 432.5, 0) mm
- Aileron1 = (94, 477.5, 0) mm
- Aileron1 = (94, 522.5, 0) mm
- Aileron1 = (94, 567.5, 0) mm
- Aileron1 = (94, 612.5, 0) mm
- Aileron1 = (94, 657.5, 0) mm

Sensor Plates

CG of leading bars+plate = (-52.5, 725, 0) mm
CG of trailing bars+plate = (52.5, 725, 0) mm

Volume of plate = 900.06 mm^3
Volume of horizontal bar = 44.5*6*2 = 534 mm^3

For a total of 4 bars and 2 plates:
$\therefore$ Total volume = (4*534) + (2*900.06) = 3,936.12 mm^3
Density of Nylon12 = 930 kg/m3 $\Rightarrow$ Total mass = 3.93612e-6*930 = 0.00366 Kg = 3.66 g

Therefore, Plate1 (leading) = 3.66/2 = 1.83 g
Plate2 (trailing) = 1.83 g

A.3. Node Selection Criteria for Spanwise Deformation Extraction

To enable spanwise deformation analysis across both static and modal simulations, a set of node-based `Named Selections` was carefully defined. These nodes were selected using ANSYS's *Worksheet* filtering with the following criteria, applied in order:

1. Add all mesh nodes at $Z = 1.125 \times 10^{-3}$ m
2. Remove all nodes where $X \neq 0$
3. Remove all nodes with Node ID $\in$ [3900,22000]

This procedure yielded a set of nodes aligned along the global Y-axis from 0 to 0.75 m, located at $X = 0$ and $Z = 1.125 \times 10^{-3}$ m free from unwanted mid-side nodes.

For torsional analysis, two additional named selections were defined on the leading and trailing edges of the spar: `spar_LE` (negative X) and `spar_TE` (positive X). These were created using the following criteria:

1. Add all mesh nodes at $Z = 0$ m
2. Filter nodes such that $X = \pm 0.03$ m
3. Remove all nodes with Node ID > 30000

This ensured a clean spanwise set of nodes from 0 to 0.75 m located at $X = \pm 0.03$ m and $Z = 0$, free from unwanted mid-side nodes or irregular spacing.

A.4. 3D Wing Modal Raw Spanwise Deformation Data

This section contains the numerical data of the spanwise deformation fields extracted from the 3D wing modal analysis for modes 1-5. Tabulated data is available at 5 mm resolution from root to tip. The values include:

- Vertical displacement $u_z(y)$ from the `BeamNodes`
- Horizontal displacement $u_x(y)$ from the `BeamNodes`
- Vertical displacements $u_z^{LE}(y)$ and $u_z^{TE}(y)$ from `spar_LE` and `spar_TE`

The twist angle $\theta_y(y)$ was not obtained directly from the solver. Instead, it was computed post-process using the vertical displacement difference between the trailing and leading edge nodes:

$$\theta_y(y) = \frac{u_z^{TE}(y) - u_z^{LE}(y)}{0.060}$$

where 0.060 m is the known chordwise distance between the node groups.

Mode 1				
u_z	u_x	u_z^{TE}	u_z^{LE}	θy
0	0	0	0	0
2.58E-05	-2.16E-07	2.16E-05	1.02E-05	-0.00019
1.05E-04	-6.51E-07	8.72E-05	4.78E-05	-0.00066
2.53E-04	-1.54E-06	1.97E-04	1.20E-04	-0.00129
5.03E-04	-2.13E-06	3.66E-04	2.45E-04	-0.00201
9.17E-04	-3.29E-06	6.38E-04	4.64E-04	-0.00289
1.66E-03	-4.60E-06	1.14E-03	9.13E-04	-0.00381
2.91E-03	-6.09E-06	2.19E-03	1.88E-03	-0.00518
4.66E-03	-7.69E-06	3.81E-03	3.41E-03	-0.00671
6.88E-03	-9.37E-06	5.98E-03	5.48E-03	-0.00831
9.58E-03	-1.10E-05	8.69E-03	8.10E-03	-0.00989
1.27E-02	-1.26E-05	1.19E-02	1.12E-02	-0.01135
1.63E-02	-1.38E-05	1.57E-02	1.49E-02	-0.01262
2.04E-02	-1.47E-05	1.99E-02	1.91E-02	-0.01353
2.49E-02	-1.49E-05	2.46E-02	2.37E-02	-0.01397
2.99E-02	-1.45E-05	2.95E-02	2.87E-02	-0.01357
3.53E-02	-1.33E-05	3.48E-02	3.40E-02	-0.01237
4.11E-02	-1.15E-05	4.05E-02	3.98E-02	-0.01065
4.74E-02	-9.31E-06	4.66E-02	4.61E-02	-0.00858
5.40E-02	-6.73E-06	5.32E-02	5.28E-02	-0.00622
6.11E-02	-3.88E-06	6.02E-02	6.00E-02	-0.00363
6.85E-02	-8.01E-07	6.76E-02	6.76E-02	-0.00087
7.63E-02	2.483E-06	7.55E-02	7.56E-02	0.002083
8.45E-02	6.004E-06	8.37E-02	8.40E-02	0.005233
9.31E-02	9.756E-06	9.22E-02	9.27E-02	0.00855

0.10207	1.373E-05	0.10093	0.10165	0.012
0.11141	1.787E-05	0.11008	0.11102	0.015667
0.1211	2.211E-05	0.11961	0.12078	0.0195
0.13113	2.642E-05	0.12952	0.13092	0.023333
0.14149	3.077E-05	0.13981	0.14145	0.027333
0.15219	3.515E-05	0.15047	0.15234	0.031167
0.16321	3.956E-05	0.16147	0.16358	0.035167
0.17456	4.402E-05	0.1728	0.17515	0.039167
0.18624	4.850E-05	0.18435	0.18694	0.043167
0.19825	5.307E-05	0.19616	0.19899	0.047167
0.21057	5.766E-05	0.20829	0.21137	0.051333
0.2232	6.224E-05	0.22076	0.22408	0.055333
0.23611	6.681E-05	0.23356	0.23712	0.059333
0.2493	7.136E-05	0.24667	0.25047	0.063333
0.26278	7.589E-05	0.26009	0.26414	0.0675
0.27653	8.039E-05	0.27381	0.2781	0.0715
0.29055	8.488E-05	0.28779	0.29232	0.0755
0.30485	8.938E-05	0.30195	0.30672	0.0795
0.31943	9.387E-05	0.31634	0.32136	0.083667
0.33427	9.831E-05	0.33101	0.33626	0.0875
0.34936	1.027E-04	0.34597	0.35145	0.091333
0.36469	1.071E-04	0.36119	0.36691	0.095333
0.38026	1.114E-04	0.37668	0.38263	0.099167
0.39606	1.157E-04	0.39243	0.39861	0.103
0.41208	1.199E-04	0.40841	0.41482	0.106833
0.42833	1.240E-04	0.42461	0.43125	0.110667
0.44481	1.281E-04	0.44095	0.44781	0.114333
0.46151	1.322E-04	0.45749	0.46457	0.118
0.47843	1.363E-04	0.47427	0.48156	0.1215
0.49555	1.403E-04	0.49127	0.49878	0.125167
0.51287	1.442E-04	0.50849	0.51621	0.128667
0.53038	1.480E-04	0.52593	0.53386	0.132167
0.54807	1.518E-04	0.54358	0.55171	0.1355
0.56594	1.554E-04	0.56141	0.56975	0.139
0.58399	1.590E-04	0.57941	0.58795	0.142333
0.60223	1.625E-04	0.59752	0.60624	0.145333
0.62063	1.660E-04	0.61579	0.6247	0.1485
0.63921	1.694E-04	0.63425	0.64334	0.1515
0.65795	1.726E-04	0.65289	0.66216	0.1545
0.67683	1.758E-04	0.67171	0.68116	0.1575
0.69587	1.789E-04	0.69069	0.70031	0.160333
0.71504	1.819E-04	0.70983	0.71962	0.163167
0.73435	1.848E-04	0.72911	0.73906	0.165833
0.75379	1.876E-04	0.74852	0.75862	0.168333
0.77337	1.902E-04	0.76799	0.77824	0.170833
0.79307	1.903E-04	0.78759	0.79799	0.173333
0.8129	1.928E-04	0.80735	0.81788	0.1755
0.83284	1.952E-04	0.82724	0.8379	0.177667
0.85289	1.975E-04	0.84727	0.85805	0.179667
0.87305	1.996E-04	0.86741	0.87831	0.181667
0.8933	2.016E-04	0.88766	0.89867	0.1835
0.91364	2.035E-04	0.908	0.91911	0.185167
0.93408	2.050E-04	0.92842	0.9396	0.186333
0.95461	2.066E-04	0.94884	0.96011	0.187833
0.97523	2.079E-04	0.96937	0.98072	0.189167

0.99595	2.091E-04	0.99004	1.0015	0.191
1.0168	2.105E-04	1.0108	1.0223	0.191667
1.0377	2.115E-04	1.0317	1.0433	0.193333
1.0586	2.126E-04	1.0527	1.0643	0.193333
1.0797	2.137E-04	1.0737	1.0855	0.196667
1.1008	2.149E-04	1.0949	1.1067	0.196667
1.122	2.157E-04	1.116	1.1279	0.198333
1.1433	2.171E-04	1.1372	1.1491	0.198333
1.1646	2.178E-04	1.1584	1.1704	0.2
1.186	2.185E-04	1.1798	1.1918	0.2
1.2075	2.195E-04	1.2013	1.2134	0.201667
1.229	2.203E-04	1.2228	1.235	0.203333
1.2507	2.213E-04	1.2444	1.2567	0.205
1.2723	2.224E-04	1.2661	1.2784	0.205
1.2941	2.235E-04	1.2878	1.3002	0.206667
1.3158	2.246E-04	1.3095	1.322	0.208333
1.3377	2.257E-04	1.3313	1.3438	0.208333
1.3595	2.268E-04	1.3531	1.3657	0.21
1.3815	2.280E-04	1.375	1.3877	0.211667
1.4034	2.292E-04	1.3969	1.4097	0.213333
1.4254	2.304E-04	1.4189	1.4318	0.215
1.4474	2.316E-04	1.4409	1.4539	0.216667
1.4695	2.328E-04	1.4629	1.476	0.218333
1.4916	2.339E-04	1.485	1.4981	0.218333
1.5137	2.351E-04	1.5071	1.5203	0.22
1.5358	2.362E-04	1.5291	1.5424	0.221667
1.5579	2.373E-04	1.5512	1.5646	0.223333
1.5801	2.383E-04	1.5733	1.5868	0.225
1.6023	2.393E-04	1.5955	1.609	0.225
1.6245	2.403E-04	1.6176	1.6312	0.226667
1.6467	2.412E-04	1.6398	1.6535	0.228333
1.6689	2.421E-04	1.662	1.6757	0.228333
1.6911	2.429E-04	1.6842	1.698	0.23
1.7133	2.436E-04	1.7064	1.7202	0.23
1.7354	2.442E-04	1.7285	1.7424	0.231667
1.7576	2.447E-04	1.7506	1.7646	0.233333
1.7798	2.451E-04	1.7728	1.7868	0.233333
1.802	2.453E-04	1.795	1.809	0.233333
1.8242	2.455E-04	1.8172	1.8312	0.233333
1.8464	2.456E-04	1.8394	1.8534	0.233333
1.8685	2.456E-04	1.8615	1.8756	0.235
1.8907	2.455E-04	1.8837	1.8978	0.235
1.9128	2.453E-04	1.9058	1.9199	0.235
1.9349	2.450E-04	1.9278	1.9419	0.235
1.9569	2.445E-04	1.9499	1.964	0.235
1.979	2.438E-04	1.972	1.9861	0.235
2.001	2.431E-04	1.9941	2.0081	0.233333
2.0231	2.422E-04	2.0161	2.0301	0.233333
2.0451	2.412E-04	2.0381	2.0521	0.233333
2.067	2.401E-04	2.0601	2.0741	0.233333
2.089	2.389E-04	2.0821	2.096	0.231667
2.1109	2.376E-04	2.104	2.1179	0.231667
2.1327	2.359E-04	2.1258	2.1396	0.23
2.1546	2.348E-04	2.1477	2.1614	0.228333
2.1765	2.328E-04	2.1696	2.1832	0.226667

2.1983	2.309E-04	2.1915	2.2051	0.226667
2.2201	2.287E-04	2.2134	2.2269	0.225
2.2419	2.265E-04	2.2352	2.2487	0.225
2.2637	2.242E-04	2.2571	2.2704	0.221667
2.2855	2.218E-04	2.2789	2.2922	0.221667
2.3072	2.193E-04	2.3007	2.3139	0.22
2.329	2.168E-04	2.3225	2.3355	0.216667
2.3507	2.143E-04	2.3442	2.3572	0.216667
2.3724	2.116E-04	2.366	2.3788	0.213333
2.3941	2.090E-04	2.3878	2.4005	0.211667
2.4158	2.062E-04	2.4096	2.4222	0.21
2.4375	2.035E-04	2.4313	2.4438	0.208333
2.4591	2.007E-04	2.453	2.4654	0.206667
2.4807	1.980E-04	2.4747	2.487	0.205
2.5024	0.000195	2.4964	2.5085	0.201667
2.524	1.926E-04	2.518	2.53	0.2

Table A.1: Wing raw spanwise deformation dataset for mode 1

Mode 2				
u_z	u_x	u_z^{TE}	u_z^{LE}	θy
0	0	0	0	0
-0.00017	9.15E-07	-0.00012	-9.38E-05	0.000453
-0.00066	2.07E-06	-0.00049	-3.93E-04	0.001672
-0.00155	4.13E-06	-0.00111	-9.13E-04	0.003253
-0.00301	2.19E-06	-0.00203	-1.76E-03	0.004468
-0.00536	-1.4E-08	-0.00347	-3.20E-03	0.004627
-0.00947	-7E-06	-0.00606	-6.12E-03	-0.00091
-0.01632	-2E-05	-0.01138	-1.22E-02	-0.01382
-0.02578	-4E-05	-0.01951	-2.14E-02	-0.03195
-0.03769	-6.4E-05	-0.03036	-3.36E-02	-0.05407
-0.05194	-9.2E-05	-0.04382	-4.86E-02	-0.07955
-0.06842	-0.00013	-0.05975	-6.62E-02	-0.10822
-0.08704	-0.00016	-0.07802	-8.64E-02	-0.14023
-0.1077	-0.00021	-0.0984	-0.10898	-0.17628
-0.13036	-0.00025	-0.12066	-0.13369	-0.21717
-0.15495	-0.00031	-0.14401	-0.15997	-0.266
-0.18137	-0.00037	-0.16849	-0.18782	-0.32217
-0.20948	-0.00044	-0.19456	-0.21755	-0.38317
-0.23914	-0.00051	-0.22221	-0.24905	-0.44733
-0.27024	-0.00058	-0.25139	-0.28224	-0.51417
-0.30267	-0.00066	-0.28202	-0.31699	-0.58283
-0.33634	-0.00074	-0.314	-0.35318	-0.653
-0.37117	-0.00082	-0.34719	-0.39067	-0.72467
-0.40709	-0.0009	-0.38141	-0.4293	-0.79817
-0.44404	-0.00099	-0.41625	-0.46864	-0.87317
-0.48193	-0.00107	-0.45177	-0.5088	-0.9505
-0.52066	-0.00116	-0.48814	-0.54988	-1.029
-0.56013	-0.00125	-0.5253	-0.59177	-1.10783
-0.60023	-0.00134	-0.56316	-0.6344	-1.18733
-0.64089	-0.00143	-0.60163	-0.67766	-1.26717
-0.68201	-0.00152	-0.64062	-0.72143	-1.34683
-0.72351	-0.00161	-0.68002	-0.76562	-1.42667
-0.76533	-0.0017	-0.71972	-0.81007	-1.50583

-0.80739	-0.00179	-0.75952	-0.8546	-1.58467
-0.84962	-0.00188	-0.79952	-0.89933	-1.6635
-0.89194	-0.00196	-0.83967	-0.94417	-1.74167
-0.93427	-0.00205	-0.87986	-0.98901	-1.81917
-0.97654	-0.00214	-0.91999	-1.0338	-1.89683
-1.0187	-0.00222	-0.95997	-1.0783	-1.97217
-1.0606	-0.00231	-0.99973	-1.1226	-2.04783
-1.1022	-0.00239	-1.0392	-1.1666	-2.12333
-1.1434	-0.00248	-1.0783	-1.21	-2.195
-1.1842	-0.00256	-1.117	-1.2531	-2.26833
-1.2244	-0.00264	-1.1554	-1.2957	-2.33833
-1.2641	-0.00271	-1.1933	-1.3378	-2.40833
-1.3032	-0.00279	-1.2307	-1.3792	-2.475
-1.3416	-0.00287	-1.2672	-1.4198	-2.54333
-1.3792	-0.00294	-1.303	-1.4595	-2.60833
-1.416	-0.00301	-1.3379	-1.4982	-2.67167
-1.4519	-0.00308	-1.3718	-1.5359	-2.735
-1.4869	-0.00315	-1.4048	-1.5725	-2.795
-1.5208	-0.00322	-1.4371	-1.6083	-2.85333
-1.5536	-0.00328	-1.4686	-1.6432	-2.91
-1.5853	-0.00334	-1.4991	-1.677	-2.965
-1.6158	-0.0034	-1.5284	-1.7094	-3.01667
-1.6451	-0.00346	-1.5563	-1.7404	-3.06833
-1.6732	-0.00351	-1.5829	-1.77	-3.11833
-1.6999	-0.00357	-1.6081	-1.7981	-3.16667
-1.7253	-0.00362	-1.6319	-1.8247	-3.21333
-1.7493	-0.00367	-1.6542	-1.8496	-3.25667
-1.7717	-0.00372	-1.6755	-1.8733	-3.29667
-1.7926	-0.00376	-1.6957	-1.8959	-3.33667
-1.8118	-0.0038	-1.7144	-1.9168	-3.37333
-1.8295	-0.00384	-1.7314	-1.9359	-3.40833
-1.8457	-0.00387	-1.7467	-1.9531	-3.44
-1.8601	-0.00391	-1.7603	-1.9685	-3.47
-1.873	-0.00394	-1.7719	-1.9819	-3.5
-1.8841	-0.00397	-1.7818	-1.9934	-3.52667
-1.8934	-0.004	-1.79	-2.003	-3.55
-1.9008	-0.00402	-1.7967	-2.0111	-3.57333
-1.9064	-0.00404	-1.8022	-2.0177	-3.59167
-1.9101	-0.00406	-1.8059	-2.0223	-3.60667
-1.9119	-0.00408	-1.8076	-2.0248	-3.62
-1.9119	-0.00409	-1.8072	-2.0251	-3.63167
-1.9101	-0.0041	-1.8047	-2.0233	-3.64333
-1.9063	-0.00411	-1.8002	-2.0193	-3.65167
-1.9007	-0.00412	-1.7937	-2.013	-3.655
-1.893	-0.00412	-1.7852	-2.0047	-3.65833
-1.8834	-0.00412	-1.7756	-1.9951	-3.65833
-1.8717	-0.00411	-1.7647	-1.9841	-3.65667
-1.8581	-0.00411	-1.7518	-1.9709	-3.65167
-1.8425	-0.0041	-1.7368	-1.9554	-3.64333
-1.8249	-0.00409	-1.7197	-1.9377	-3.63333
-1.8054	-0.00408	-1.7004	-1.9177	-3.62167
-1.784	-0.00406	-1.6789	-1.8955	-3.61
-1.7606	-0.00404	-1.6553	-1.871	-3.595
-1.7352	-0.00402	-1.6298	-1.8444	-3.57667
-1.7078	-0.004	-1.6031	-1.8166	-3.55833

-1.6784	-0.00398	-1.5751	-1.7874	-3.53833
-1.647	-0.00395	-1.5452	-1.7559	-3.51167
-1.6136	-0.00392	-1.5131	-1.7223	-3.48667
-1.5784	-0.00389	-1.479	-1.6864	-3.45667
-1.5413	-0.00385	-1.4428	-1.6484	-3.42667
-1.5024	-0.00381	-1.4045	-1.6082	-3.395
-1.4616	-0.00378	-1.3643	-1.566	-3.36167
-1.419	-0.00374	-1.3223	-1.5218	-3.325
-1.3745	-0.00369	-1.2791	-1.4763	-3.28667
-1.3282	-0.00365	-1.2344	-1.4293	-3.24833
-1.2801	-0.0036	-1.188	-1.3803	-3.205
-1.2303	-0.00355	-1.1397	-1.3294	-3.16167
-1.1789	-0.0035	-1.0896	-1.2766	-3.11667
-1.1258	-0.00345	-1.0377	-1.222	-3.07167
-1.0712	-0.00339	-0.98415	-1.1656	-3.02417
-1.0151	-0.00334	-0.92893	-1.1075	-2.97617
-0.95737	-0.00329	-0.87223	-1.0479	-2.92783
-0.89814	-0.00323	-0.81453	-0.98719	-2.87767
-0.8374	-0.00317	-0.75563	-0.92528	-2.8275
-0.77523	-0.00311	-0.69524	-0.86181	-2.77617
-0.71171	-0.00306	-0.63338	-0.79683	-2.72417
-0.64689	-0.003	-0.57008	-0.73038	-2.67167
-0.58083	-0.00294	-0.50541	-0.66252	-2.6185
-0.51359	-0.00288	-0.43941	-0.59332	-2.56517
-0.44519	-0.00282	-0.3722	-0.52289	-2.5115
-0.37565	-0.00276	-0.30391	-0.45135	-2.45733
-0.305	-0.0027	-0.2349	-0.37916	-2.40433
-0.23327	-0.00263	-0.16495	-0.30603	-2.35133
-0.16053	-0.00257	-0.09392	-0.2318	-2.29797
-0.08686	-0.00251	-0.02186	-0.15653	-2.24452
-0.01232	-0.00245	0.051187	-8.03E-02	-2.19098
0.06304	-0.00239	0.12516	-3.10E-03	-2.13772
0.13916	-0.00233	0.19998	7.49E-02	-2.08467
0.216	-0.00228	0.27557	0.15364	-2.03217
0.29352	-0.00222	0.35181	0.23299	-1.98033
0.3717	-0.00216	0.42844	0.31259	-1.93083
0.45049	-0.00211	0.50575	0.39276	-1.88317
0.52984	-0.00206	0.58373	0.47355	-1.83633
0.60969	-0.002	0.66231	0.55489	-1.79033
0.68999	-0.00195	0.74143	0.63671	-1.74533
0.77067	-0.0019	0.82101	0.71894	-1.70117
0.85171	-0.00185	0.90099	0.80151	-1.658
0.93305	-0.00181	0.98131	0.88428	-1.61717
1.0147	-0.00177	1.0617	0.96722	-1.57467
1.0966	-0.00172	1.1423	1.0499	-1.54
1.1787	-0.00169	1.2234	1.1328	-1.51
1.2611	-0.00165	1.3047	1.2162	-1.475
1.3437	-0.00161	1.3864	1.2998	-1.44333
1.4265	-0.00158	1.4684	1.3837	-1.41167
1.5094	-0.00154	1.5506	1.4676	-1.38333
1.5925	-0.00151	1.6328	1.5517	-1.35167
1.6756	-0.00148	1.7152	1.6359	-1.32167
1.7588	-0.00145	1.7976	1.7199	-1.295
1.8421	-0.00142	1.88	1.8038	-1.27
1.9254	-0.0014	1.9626	1.8878	-1.24667

2.0087	-0.00137	2.0453	1.9718	-1.225
2.092	-0.00135	2.1281	2.0559	-1.20333
2.1753	-0.00132	2.2109	2.1399	-1.18333
2.2586	-0.0013	2.2937	2.2239	-1.16333
2.3419	-0.00128	2.3764	2.3079	-1.14167
2.4251	-0.00126	2.459	2.3917	-1.12167
2.5083	-0.00124	2.5415	2.4753	-1.10333
2.5914	-0.00122	2.6236	2.5587	-1.08167

Table A.2: Wing raw spanwise deformation dataset for mode 2

Mode 3				
u_z	u_x	u_z^{TE}	u_z^{LE}	θy
0	0	0	0	0
-5.5E-05	-2.4E-06	0.000184	-1.86E-04	-6.17E-03
-0.00022	-1.7E-05	0.00058	-6.46E-04	-2.04E-02
-0.0005	-4.7E-05	0.001079	-1.32E-03	-4.00E-02
-0.00096	-9.9E-05	0.001692	-2.31E-03	-6.67E-02
-0.00169	-0.00018	0.00258	-3.96E-03	-1.09E-01
-0.00295	-0.00031	0.004422	-7.56E-03	-2.00E-01
-0.00501	-0.0005	0.007714	-1.46E-02	-3.71E-01
-0.00782	-0.00075	0.011619	-2.39E-02	-5.93E-01
-0.0113	-0.00104	0.015791	-3.52E-02	-8.50E-01
-0.01539	-0.00137	0.020033	-4.80E-02	-1.13E+00
-0.02003	-0.00173	0.02426	-6.20E-02	-1.44E+00
-0.02515	-0.00211	0.028456	-7.71E-02	-1.76E+00
-0.0307	-0.00252	0.03268	-9.31E-02	-2.10E+00
-0.03661	-0.00295	0.037054	-0.11	-2.45E+00
-0.04284	-0.00339	0.041979	-0.12773	-2.83E+00
-0.04932	-0.00387	0.047475	-0.14633	-3.23E+00
-0.056	-0.00436	0.053193	-0.16554	-3.65E+00
-0.06282	-0.00486	0.059061	-0.18523	-4.07E+00
-0.06973	-0.00538	0.065049	-0.20525	-4.50E+00
-0.07669	-0.0059	0.071163	-0.22552	-4.94E+00
-0.08363	-0.00644	0.077435	-0.24595	-5.39E+00
-0.09054	-0.00698	0.083918	-0.2665	-5.84E+00
-0.09735	-0.00754	0.090681	-0.28708	-6.30E+00
-0.10405	-0.0081	0.097965	-0.30774	-6.76E+00
-0.1106	-0.00867	0.10574	-0.32864	-7.24E+00
-0.11697	-0.00925	0.11384	-0.34953	-7.72E+00
-0.12317	-0.00984	0.12223	-0.37034	-8.21E+00
-0.12917	-0.01043	0.13091	-0.39103	-8.70E+00
-0.13496	-0.01103	0.13988	-0.41155	-9.19E+00
-0.14052	-0.01163	0.14913	-0.43187	-9.68E+00
-0.14585	-0.01224	0.15867	-0.45195	-1.02E+01
-0.15093	-0.01284	0.16848	-0.47175	-1.07E+01
-0.15574	-0.01345	0.17868	-0.49139	-1.12E+01
-0.16029	-0.01407	0.18922	-0.51108	-1.17E+01
-0.16456	-0.01469	0.20002	-0.53052	-1.22E+01
-0.16857	-0.01531	0.2111	-0.5497	-1.27E+01
-0.17233	-0.01593	0.22245	-0.56859	-1.32E+01
-0.17583	-0.01655	0.23408	-0.58717	-1.37E+01
-0.17906	-0.01717	0.24597	-0.60543	-1.42E+01
-0.18204	-0.0178	0.25811	-0.62334	-1.47E+01

-0.18475	-0.01842	0.27042	-0.64086	-1.52E+01
-0.18719	-0.01904	0.28299	-0.65814	-1.57E+01
-0.18937	-0.01966	0.29582	-0.67541	-1.62E+01
-0.19129	-0.02028	0.30879	-0.69233	-1.67E+01
-0.19297	-0.02091	0.32196	-0.70895	-1.72E+01
-0.19442	-0.02153	0.33533	-0.72524	-1.77E+01
-0.19563	-0.02215	0.34891	-0.74121	-1.82E+01
-0.19663	-0.02276	0.36266	-0.75685	-1.87E+01
-0.1974	-0.02338	0.37656	-0.77213	-1.91E+01
-0.19796	-0.024	0.39054	-0.787	-1.96E+01
-0.1983	-0.0246	0.40471	-0.80165	-2.01E+01
-0.19843	-0.02522	0.41902	-0.81628	-2.06E+01
-0.19837	-0.02582	0.43334	-0.83055	-2.11E+01
-0.19812	-0.02643	0.44776	-0.84453	-2.15E+01
-0.19769	-0.02703	0.46228	-0.85821	-2.20E+01
-0.1971	-0.02763	0.47691	-0.87161	-2.25E+01
-0.19635	-0.02823	0.49161	-0.88471	-2.29E+01
-0.19544	-0.02882	0.50636	-0.89748	-2.34E+01
-0.19437	-0.02941	0.52105	-0.90986	-2.38E+01
-0.19316	-0.02999	0.53582	-0.92207	-2.43E+01
-0.19181	-0.03058	0.55068	-0.93431	-2.47E+01
-0.19031	-0.03115	0.56543	-0.94619	-2.52E+01
-0.18869	-0.03173	0.58017	-0.9578	-2.56E+01
-0.18694	-0.0323	0.59493	-0.96914	-2.61E+01
-0.18507	-0.03286	0.60969	-0.98021	-2.65E+01
-0.18307	-0.03342	0.62445	-0.99098	-2.69E+01
-0.18096	-0.03398	0.63917	-1.0014	-2.73E+01
-0.17874	-0.03453	0.65369	-1.0114	-2.78E+01
-0.1764	-0.03507	0.66822	-1.0212	-2.82E+01
-0.17395	-0.03561	0.68276	-1.031	-2.86E+01
-0.17139	-0.03613	0.69709	-1.0403	-2.90E+01
-0.16875	-0.03666	0.71129	-1.0493	-2.93E+01
-0.16602	-0.03717	0.72538	-1.058	-2.97E+01
-0.16323	-0.03767	0.73933	-1.0664	-3.01E+01
-0.16039	-0.03817	0.75309	-1.0745	-3.05E+01
-0.15751	-0.03865	0.76658	-1.0821	-3.08E+01
-0.15463	-0.03914	0.77958	-1.089	-3.11E+01
-0.1518	-0.03959	0.79242	-1.0954	-3.15E+01
-0.14903	-0.04005	0.80556	-1.1026	-3.18E+01
-0.14637	-0.04052	0.81827	-1.1099	-3.21E+01
-0.14384	-0.04098	0.8307	-1.1172	-3.25E+01
-0.14149	-0.04143	0.84282	-1.1247	-3.28E+01
-0.13932	-0.04188	0.85461	-1.1322	-3.31E+01
-0.13738	-0.04233	0.86599	-1.1398	-3.34E+01
-0.13568	-0.04277	0.87696	-1.1473	-3.37E+01
-0.13429	-0.04322	0.88708	-1.1546	-3.40E+01
-0.13323	-0.04364	0.89742	-1.162	-3.43E+01
-0.13253	-0.04408	0.90767	-1.1706	-3.46E+01
-0.13221	-0.04452	0.91753	-1.1795	-3.50E+01
-0.1323	-0.04497	0.92688	-1.1889	-3.53E+01
-0.13278	-0.04541	0.93576	-1.1987	-3.56E+01
-0.13367	-0.04585	0.94416	-1.2089	-3.59E+01
-0.13497	-0.0463	0.95206	-1.2195	-3.62E+01
-0.13668	-0.04674	0.95943	-1.2305	-3.65E+01
-0.13882	-0.04718	0.96618	-1.2417	-3.68E+01

-0.14141	-0.04762	0.97286	-1.2534	-3.71E+01
-0.14443	-0.04807	0.97932	-1.2658	-3.74E+01
-0.14787	-0.04851	0.98513	-1.2783	-3.77E+01
-0.15172	-0.04894	0.99038	-1.2912	-3.80E+01
-0.15597	-0.04938	0.99508	-1.3044	-3.83E+01
-0.1606	-0.04981	0.99923	-1.318	-3.86E+01
-0.16562	-0.05023	1.0028	-1.3318	-3.89E+01
-0.17103	-0.05065	1.0059	-1.3459	-3.92E+01
-0.17682	-0.05107	1.0082	-1.36	-3.95E+01
-0.18301	-0.05148	1.0103	-1.3744	-3.97E+01
-0.18957	-0.05188	1.0122	-1.3893	-4.00E+01
-0.19649	-0.05228	1.0134	-1.4043	-4.03E+01
-0.20375	-0.05268	1.014	-1.4194	-4.06E+01
-0.21132	-0.05307	1.0142	-1.4347	-4.08E+01
-0.21919	-0.05345	1.0138	-1.4502	-4.11E+01
-0.22734	-0.05383	1.013	-1.4658	-4.13E+01
-0.23576	-0.0542	1.0117	-1.4816	-4.16E+01
-0.24444	-0.05457	1.0098	-1.4972	-4.18E+01
-0.25337	-0.05493	1.0079	-1.5131	-4.20E+01
-0.26254	-0.05529	1.0058	-1.5293	-4.23E+01
-0.27193	-0.05564	1.0031	-1.5455	-4.25E+01
-0.28151	-0.05598	1	-1.5617	-4.27E+01
-0.29125	-0.05632	0.99661	-1.5778	-4.29E+01
-0.30115	-0.05666	0.99287	-1.594	-4.31E+01
-0.31117	-0.05699	0.98882	-1.6102	-4.33E+01
-0.32132	-0.05731	0.98444	-1.6262	-4.35E+01
-0.33156	-0.05762	0.9796	-1.6419	-4.37E+01
-0.3419	-0.05793	0.97475	-1.6578	-4.39E+01
-0.35231	-0.05823	0.96986	-1.6738	-4.41E+01
-0.36277	-0.05853	0.96456	-1.6896	-4.42E+01
-0.37327	-0.05881	0.95898	-1.7052	-4.44E+01
-3.84E-01	-0.05909	0.95318	-1.7206	-4.46E+01
-3.94E-01	-0.05936	0.94718	-1.7357	-4.47E+01
-4.05E-01	-0.05963	0.94098	-1.7507	-4.49E+01
-4.15E-01	-0.05988	0.93447	-1.7653	-4.50E+01
-4.26E-01	-0.06014	0.9277	-1.779	-4.51E+01
-4.36E-01	-0.06037	0.92075	-1.7932	-4.52E+01
-4.47E-01	-0.06061	0.91454	-1.8075	-4.54E+01
-4.57E-01	-0.06085	0.90771	-1.8217	-4.55E+01
-4.68E-01	-0.06108	0.90075	-1.8357	-4.56E+01
-4.78E-01	-0.0613	0.89367	-1.8495	-4.57E+01
-4.88E-01	-0.06153	0.88649	-1.8631	-4.58E+01
-4.99E-01	-0.06174	0.87921	-1.8765	-4.59E+01
-5.09E-01	-0.06196	0.87182	-1.8897	-4.60E+01
-5.19E-01	-0.06216	0.86416	-1.9025	-4.61E+01
-5.29E-01	-0.06236	0.85672	-1.9154	-4.62E+01
-5.40E-01	-0.06256	0.84943	-1.9284	-4.63E+01
-5.50E-01	-0.06276	0.84188	-1.941	-4.64E+01
-5.60E-01	-0.06295	0.83423	-1.9534	-4.65E+01
-5.70E-01	-0.06313	0.82653	-1.9656	-4.65E+01
-5.80E-01	-0.06332	0.81881	-1.9776	-4.66E+01
-5.89E-01	-0.0635	0.8111	-1.9896	-4.67E+01
-5.99E-01	-0.06368	0.80341	-2.0014	-4.67E+01
-6.09E-01	-0.06386	0.79564	-2.0131	-4.68E+01
-0.61894	-0.06403	0.78804	-2.0245	-4.69E+01

Table A.3: Wing raw spanwise deformation dataset for mode 3

Mode 4				
u_z	u_x	u_z^{TE}	u_z^{LE}	θy
0	0	0	0	0
0.000546	3.11E-07	3.85E-04	0.000342	0.000719
0.002142	-3.44E-06	1.53E-03	0.001413	0.001913
0.00493	-1.06E-05	3.41E-03	0.003177	0.003898
0.009386	-4.20E-06	6.35E-03	0.005774	0.009532
0.016415	8.39E-06	1.12E-02	0.009752	0.024162
0.028467	4.66E-05	2.10E-02	0.01662	0.07335
0.048234	1.20E-04	4.10E-02	0.03052	0.17385
0.075197	2.25E-04	7.02E-02	0.051713	0.3079
0.10875	3.56E-04	0.10783	0.079853	0.466283
0.14839	5.06E-04	0.15312	0.11453	0.643167
0.19365	6.72E-04	0.20539	0.15524	0.835833
0.24408	8.52E-04	0.26399	0.20139	1.043333
0.29924	1.05E-03	0.32823	0.2523	1.2655
0.35875	1.26E-03	0.39741	0.30709	1.505333
0.42224	1.49E-03	0.47005	0.36379	1.771
0.48925	1.73E-03	0.54598	0.42228	2.061667
0.55925	1.99E-03	0.62533	0.48337	2.366
0.63172	2.26E-03	0.70763	0.54683	2.68
7.06E-01	2.53E-03	0.79234	0.61235	2.999833
0.78225	2.80E-03	0.87893	0.67952	3.3235
0.85945	3.06E-03	0.96687	7.48E-01	3.6485
0.9374	3.33E-03	1.0556	8.17E-01	3.973167
1.0157	3.58E-03	1.1446	0.88686	4.295667
1.094	3.83E-03	1.2332	0.9564	4.613333
1.1719	4.07E-03	1.3214	1.0259	4.925
1.249	4.30E-03	1.4087	1.0948	5.231667
1.3251	4.52E-03	1.4948	1.1627	5.535
1.3998	4.73E-03	1.579	1.2292	5.83
1.4728	4.92E-03	1.6612	1.2939	6.121667
1.5437	5.11E-03	1.7408	1.3566	6.403333
1.6123	5.27E-03	1.8175	1.4169	6.676667
1.6782	5.42E-03	1.8909	1.4749	6.933333
1.7409	5.54E-03	1.9613	1.5311	7.17
1.8004	5.64E-03	2.0287	1.5857	7.383333
1.8564	5.72E-03	2.0921	1.6371	7.583333
1.9087	5.77E-03	2.1512	1.685	7.77
1.9573	5.81E-03	2.2056	1.729	7.943333
2.0019	5.83E-03	2.2551	1.7688	8.105
2.0422	5.83E-03	2.2995	1.8042	8.255
2.0782	5.81E-03	2.3386	1.8353	8.388333
2.1094	5.76E-03	2.3722	1.8621	8.501667
2.1357	5.68E-03	2.4013	1.8862	8.585
2.157	5.57E-03	2.4259	1.9075	8.64
2.1732	5.43E-03	2.4446	1.9243	8.671667
2.1844	5.27E-03	2.4573	1.9361	8.686667
2.1906	5.09E-03	2.464	1.9427	8.688333
2.1917	4.88E-03	2.4645	1.9439	8.676667
2.1877	4.65E-03	2.4588	1.9398	8.65

2.1785	4.40E-03	2.4469	1.9305	8.606667
2.164	4.13E-03	2.4289	1.9165	8.54
2.144	3.82E-03	2.4061	1.8993	8.446667
2.1186	3.48E-03	2.3783	1.879	8.321667
2.088	3.12E-03	2.3445	1.854	8.175
2.0523	2.73E-03	2.3047	1.8239	8.013333
2.0116	2.32E-03	2.259	1.7887	7.838333
1.9662	1.90E-03	2.2074	1.7484	7.65
1.9161	1.45E-03	2.1501	1.7031	7.45
1.8613	9.89E-04	2.0873	1.6532	7.235
1.8019	5.01E-04	2.0193	1.5992	7.001667
1.7379	-8.36E-06	1.9475	1.5426	6.748333
1.6696	-5.43E-04	1.8715	1.4833	6.47
1.5971	-1.10E-03	1.7907	1.4203	6.173333
1.5208	-1.67E-03	1.7054	1.3534	5.866667
1.4409	-2.26E-03	1.6158	1.2828	5.55
1.3577	-2.85E-03	1.5222	1.2086	5.226667
1.2714	-3.46E-03	1.4249	1.1312	4.895
1.1823	-4.08E-03	1.3242	1.0508	4.556667
1.0905	-4.72E-03	1.2206	0.96799	4.210167
0.99613	-5.36E-03	1.1151	0.88381	3.854833
0.89958	-6.01E-03	1.0075	0.7981	3.49
0.80112	-6.67E-03	0.89763	0.71054	3.118167
7.01E-01	-7.34E-03	0.78593	6.21E-01	2.742833
6.00E-01	-8.01E-03	0.67274	5.31E-01	2.365833
0.49753	-8.68E-03	0.55845	0.43914	1.9885
0.39459	-9.36E-03	0.44349	0.34671	1.613
0.29125	-1.00E-02	0.32832	0.25387	1.240833
0.18778	-1.07E-02	0.2136	0.161	0.876667
0.084418	-1.14E-02	9.98E-02	0.068447	0.52205
-0.01858	-1.20E-02	-1.45E-02	-0.0241	0.159967
-0.12096	-1.27E-02	-0.12863	-0.1162	-0.20717
-0.22247	-1.34E-02	-0.24196	-0.20737	-0.5765
-0.32284	-1.41E-02	-0.35402	-0.29727	-0.94583
-0.42178	-1.47E-02	-0.46438	-0.38558	-1.31333
-0.51899	-1.54E-02	-0.57261	-0.472	-1.67683
-0.61416	-1.61E-02	-0.67833	-0.55625	-2.03467
-0.70698	-1.67E-02	-0.78101	-0.63819	-2.38033
-0.79725	-1.74E-02	-0.88109	-0.71846	-2.7105
-0.88476	-1.80E-02	-0.98007	-0.79718	-3.04817
-0.96922	-1.87E-02	-1.0762	-0.87321	-3.38317
-1.0505	-1.93E-02	-1.169	-0.94587	-3.71883
-1.1284	-2.00E-02	-1.2579	-1.0148	-4.05167
-1.2028	-2.06E-02	-1.3427	-1.0798	-4.38167
-1.2733	-2.13E-02	-1.423	-1.1406	-4.70667
-1.3398	-2.19E-02	-1.4986	-1.1971	-5.025
-1.4019	-2.25E-02	-1.5694	-1.2493	-5.335
-1.4593	-2.31E-02	-1.6361	-1.2983	-5.63
-1.5118	-2.37E-02	-1.699	-1.3441	-5.915
-1.5593	-2.43E-02	-1.7565	-1.3853	-6.18667
-1.6019	-2.49E-02	-1.8083	-1.4212	-6.45167
-1.6394	-2.55E-02	-1.8542	-1.4517	-6.70833
-1.6716	-2.60E-02	-1.8939	-1.4764	-6.95833
-1.6986	-2.66E-02	-1.9273	-1.4954	-7.19833
-1.72	-2.71E-02	-1.9544	-1.5087	-7.42833

-1.7356	-2.76E-02	-1.9751	-1.5165	-7.64333
-1.7452	-2.81E-02	-1.9908	-1.5203	-7.84167
-1.7488	-2.86E-02	-2.0015	-1.5202	-8.02167
-1.7465	-2.91E-02	-2.0057	-1.5144	-8.18833
-1.7383	-2.96E-02	-2.0032	-1.5026	-8.34333
-1.7244	-3.00E-02	-1.994	-1.4847	-8.48833
-1.7048	-3.05E-02	-1.9781	-1.4605	-8.62667
-1.6796	-3.09E-02	-1.9554	-1.4303	-8.75167
-1.6486	-3.13E-02	-1.9262	-1.3943	-8.865
-1.6118	-3.17E-02	-1.8906	-1.3528	-8.96333
-1.5692	-3.21E-02	-1.8502	-1.3076	-9.04333
-1.5208	-3.25E-02	-1.8049	-1.2588	-9.10167
-1.4668	-3.28E-02	-1.7534	-1.2047	-9.145
-1.4076	-3.31E-02	-1.6957	-1.1451	-9.17667
-1.3432	-3.34E-02	-1.6321	-1.0801	-9.2
-1.2739	-3.38E-02	-1.5625	-1.0098	-9.21167
-1.1998	-3.41E-02	-1.4873	-0.93421	-9.21817
-1.1209	-3.43E-02	-1.4067	-0.85382	-9.21467
-1.0374	-3.46E-02	-1.321	-0.76905	-9.19917
-0.94928	-3.49E-02	-1.2317	-0.68141	-9.1715
-0.85676	-3.51E-02	-1.1385	-0.59067	-9.1305
-0.7601	-3.54E-02	-1.0407	-0.49592	-9.07967
-0.6596	-3.56E-02	-0.93849	-0.39717	-9.022
-0.5555	-3.58E-02	-0.83198	-0.29453	-8.9575
-0.44804	-3.60E-02	-0.72149	-0.18821	-8.888
-0.33739	-3.62E-02	-0.60727	-0.07848	-8.81313
-0.22373	-3.64E-02	-0.48975	0.03431	-8.73433
-0.10716	-3.66E-02	-0.36917	0.14946	-8.64383
0.012064	-3.68E-02	-0.24745	0.26593	-8.55633
0.1338	-3.70E-02	-0.12363	0.38432	-8.46583
0.2579	-3.72E-02	3.14E-03	0.50492	-8.36296
0.38411	-3.74E-02	0.1324	0.62783	-8.25717
0.5122	-3.75E-02	0.26391	0.75278	-8.14783
0.64194	-3.77E-02	0.39738	0.87958	-8.03667
0.77313	-3.79E-02	0.53252	1.008	-7.92467
0.90559	-3.81E-02	0.66903	1.1377	-7.81117
1.0392	-3.82E-02	0.80656	1.2684	-7.69733
1.1737	-3.84E-02	0.94445	1.3998	-7.58917
1.309	-3.86E-02	1.083	1.53E+00	-7.48333
1.45E+00	-3.87E-02	1.2223	1.67E+00	-7.37833
1.58E+00	-3.89E-02	1.3621	1.80E+00	-7.275
1.72E+00	-3.91E-02	1.5023	1.93E+00	-7.17167
1.86E+00	-3.93E-02	1.6429	2.07E+00	-7.065
1.99E+00	-3.95E-02	1.7835	2.20E+00	-6.96167
2.13E+00	-3.96E-02	1.9241	2.34E+00	-6.85833
2.27E+00	-3.98E-02	2.0645	2.47E+00	-6.755
2.40E+00	-0.04002	2.2044	2.60E+00	-6.65167

Table A.4: Wing raw spanwise deformation dataset for mode 4

Mode 5				
u_z	u_x	u_z^{TE}	u_z^{LE}	θy
0	0	0	0	0
-7.51E-06	0.000149	-5.22E-05	3.70E-05	-0.00149

-2.85E-05	-0.00022	-8.52E-05	4.55E-05	-0.00218
-7.10E-05	-0.00104	-1.08E-04	1.76E-05	-0.0021
-1.34E-04	-0.00227	-1.38E-04	-3.21E-05	-0.00177
-2.30E-04	-0.0039	-1.91E-04	-1.16E-04	-0.00125
-3.92E-04	-0.00593	-2.75E-04	-2.91E-04	0.00027
-6.56E-04	-0.00836	-4.32E-04	-5.74E-04	0.002366
-1.02E-03	-0.0112	-6.84E-04	-9.90E-04	0.005101
-1.46E-03	-0.01443	-1.02E-03	-1.52E-03	0.008285
-1.99E-03	-0.01805	-1.45E-03	-2.15E-03	0.011777
-2.59E-03	-0.02204	-1.95E-03	-2.88E-03	0.015508
-3.26E-03	-0.02641	-2.53E-03	-3.69E-03	0.019423
-3.99E-03	-0.03115	-3.17E-03	-4.58E-03	0.023498
-4.78E-03	-0.03625	-3.86E-03	-5.52E-03	0.027677
-5.62E-03	-0.0417	-4.58E-03	-6.51E-03	0.032193
-6.51E-03	-0.0475	-5.33E-03	-7.53E-03	0.036687
-7.43E-03	-0.05365	-6.12E-03	-8.59E-03	0.041187
-8.39E-03	-0.06015	-6.95E-03	-9.69E-03	0.04574
-9.38E-03	-0.06699	-7.80E-03	-1.08E-02	0.050353
-1.04E-02	-0.07417	-8.68E-03	-1.20E-02	0.055037
-1.14E-02	-0.08169	-9.58E-03	-1.32E-02	0.059782
-1.25E-02	-0.08953	-1.05E-02	-1.44E-02	0.0646
-1.35E-02	-0.09771	-1.14E-02	-1.56E-02	0.069533
-1.45E-02	-0.1062	-1.23E-02	-1.68E-02	0.074767
-1.56E-02	-0.115	-1.32E-02	-1.80E-02	0.080133
-1.66E-02	-0.12411	-1.41E-02	-1.92E-02	0.08565
-1.76E-02	-0.13354	-1.49E-02	-2.04E-02	0.091267
-1.86E-02	-0.14328	-1.58E-02	-2.16E-02	0.097
-1.96E-02	-0.15331	-1.66E-02	-2.27E-02	0.102817
-2.05E-02	-0.16365	-1.73E-02	-2.39E-02	0.108767
-2.15E-02	-0.17428	-1.81E-02	-2.50E-02	0.114833
-2.23E-02	-0.1852	-1.88E-02	-2.60E-02	0.121083
-2.32E-02	-0.19641	-1.94E-02	-2.71E-02	0.127633
-2.40E-02	-0.20788	-2.00E-02	-2.81E-02	0.134483
-2.47E-02	-0.21964	-2.06E-02	-2.91E-02	0.14155
-2.54E-02	-0.23168	-2.10E-02	-3.00E-02	0.148733
-2.60E-02	-0.24398	-2.15E-02	-3.08E-02	0.15605
-2.66E-02	-0.25656	-2.18E-02	-3.16E-02	0.16345
-2.71E-02	-0.26939	-2.21E-02	-3.24E-02	0.170933
-2.76E-02	-0.28249	-2.23E-02	-3.30E-02	0.178517
-2.80E-02	-0.29584	-2.25E-02	-3.36E-02	0.186167
-2.83E-02	-0.30943	-2.26E-02	-3.42E-02	0.194183
-2.85E-02	-0.32327	-2.26E-02	-3.47E-02	0.202683
-2.87E-02	-0.33735	-2.25E-02	-3.52E-02	0.211283
-2.88E-02	-0.35168	-2.24E-02	-3.56E-02	0.22
-2.88E-02	-0.36624	-2.21E-02	-3.59E-02	0.228783
-2.88E-02	-0.38103	-2.18E-02	-3.61E-02	0.237617
-2.87E-02	-0.39605	-2.14E-02	-3.62E-02	0.246483
-2.85E-02	-0.4113	-2.10E-02	-3.63E-02	0.255367
-2.82E-02	-0.42676	-2.04E-02	-3.63E-02	0.264267
-2.79E-02	-0.44244	-1.98E-02	-3.62E-02	0.273083
-2.75E-02	-0.45832	-1.92E-02	-3.61E-02	0.282167
-2.70E-02	-0.47442	-1.84E-02	-3.59E-02	0.291333
-2.64E-02	-0.49072	-1.76E-02	-3.56E-02	0.300517
-2.58E-02	-0.50723	-1.67E-02	-3.53E-02	0.309717
-2.51E-02	-0.52393	-1.57E-02	-3.48E-02	0.318917

-2.43E-02	-0.54083	-1.47E-02	-3.43E-02	0.3281
-2.35E-02	-0.55792	-1.35E-02	-3.38E-02	0.337317
-2.26E-02	-0.57519	-1.23E-02	-3.31E-02	0.3465
-2.16E-02	-0.59265	-1.11E-02	-3.25E-02	0.355917
-2.06E-02	-0.61027	-9.79E-03	-3.17E-02	0.365417
-1.95E-02	-0.62808	-8.43E-03	-3.09E-02	0.374922
-1.84E-02	-0.64606	-7.01E-03	-3.01E-02	0.38441
-1.72E-02	-0.66421	-5.53E-03	-2.92E-02	0.393857
-1.60E-02	-0.68252	-4.00E-03	-2.82E-02	0.40323
-1.47E-02	-0.701	-2.43E-03	-2.72E-02	0.412478
-1.34E-02	-0.71963	-8.27E-04	-2.61E-02	0.421595
-1.21E-02	-0.73842	8.05E-04	-2.50E-02	0.430458
-1.07E-02	-0.75735	2.46E-03	-2.39E-02	0.439223
-9.27E-03	-0.77642	4.13E-03	-2.27E-02	0.447735
-7.84E-03	-0.79564	5.81E-03	-2.15E-02	0.455942
-6.40E-03	-0.815	7.51E-03	-2.03E-02	0.463927
-4.95E-03	-0.83449	9.20E-03	-1.91E-02	0.471688
-3.49E-03	-0.85412	1.09E-02	-1.79E-02	0.479217
-2.02E-03	-0.87388	1.26E-02	-1.66E-02	0.48645
-5.66E-04	-0.89376	1.43E-02	-1.53E-02	0.493467
8.91E-04	-0.91376	1.59E-02	-1.41E-02	0.4994
2.33E-03	-0.93388	1.75E-02	-1.28E-02	0.506067
3.77E-03	-0.95411	1.91E-02	-1.16E-02	0.512383
5.18E-03	-0.97446	2.07E-02	-1.03E-02	0.518133
6.58E-03	-0.99493	2.23E-02	-9.10E-03	0.52381
7.96E-03	-1.0155	2.39E-02	-7.88E-03	0.52932
9.32E-03	-1.0362	2.54E-02	-6.68E-03	0.534692
1.06E-02	-1.057	2.69E-02	-5.51E-03	0.539968
1.19E-02	-1.0779	2.83E-02	-4.37E-03	0.545103
1.32E-02	-1.0989	2.98E-02	-3.25E-03	0.550178
1.44E-02	-1.12	3.11E-02	-2.18E-03	0.555208
1.57E-02	-1.1412	3.25E-02	-1.13E-03	0.560625
1.68E-02	-1.1625	3.39E-02	-1.05E-04	0.565978
1.79E-02	-1.1838	3.52E-02	8.79E-04	0.571209
1.90E-02	-1.2053	3.64E-02	1.82E-03	0.576365
2.00E-02	-1.2269	3.76E-02	2.70E-03	0.581432
2.10E-02	-1.2485	3.87E-02	3.53E-03	0.586388
2.19E-02	-1.2702	3.98E-02	4.31E-03	0.591193
2.28E-02	-1.292	4.08E-02	5.03E-03	0.595765
2.36E-02	-1.3139	4.17E-02	5.70E-03	0.600303
2.43E-02	-1.3359	4.26E-02	6.33E-03	0.604687
2.50E-02	-1.3579	4.34E-02	6.89E-03	0.608825
2.56E-02	-1.38	4.42E-02	7.39E-03	0.612755
2.61E-02	-1.4022	4.48E-02	7.81E-03	0.61652
2.65E-02	-1.4244	4.54E-02	8.16E-03	0.620147
2.69E-02	-1.4467	4.59E-02	8.44E-03	0.623595
2.72E-02	-1.469	4.62E-02	8.63E-03	0.626875
2.75E-02	-1.4914	4.66E-02	8.76E-03	0.62991
2.76E-02	-1.5138	4.68E-02	8.82E-03	0.632932
2.77E-02	-1.5363	4.70E-02	8.82E-03	0.635907
2.77E-02	-1.5589	4.71E-02	8.75E-03	0.638663
2.76E-02	-1.5814	4.71E-02	8.60E-03	0.641288
2.74E-02	-1.6041	4.70E-02	8.37E-03	0.643773
2.72E-02	-1.6267	4.68E-02	8.06E-03	0.646167
2.69E-02	-1.6494	4.66E-02	7.66E-03	0.648442

2.65E-02	-1.6722	4.62E-02	7.19E-03	0.650633
2.60E-02	-1.695	4.58E-02	6.64E-03	0.652697
2.55E-02	-1.7178	4.53E-02	6.04E-03	0.654922
2.49E-02	-1.7406	4.48E-02	5.37E-03	0.657203
2.42E-02	-1.7635	4.42E-02	4.63E-03	0.659335
2.35E-02	-1.7863	4.35E-02	3.83E-03	0.661393
2.26E-02	-1.8093	4.27E-02	2.95E-03	0.663345
2.17E-02	-1.8322	4.19E-02	2.00E-03	0.665205
2.08E-02	-1.8552	4.10E-02	9.79E-04	0.666984
1.98E-02	-1.8781	4.00E-02	-1.01E-04	0.668643
1.87E-02	-1.9011	3.90E-02	-1.24E-03	0.670167
1.76E-02	-1.9241	3.79E-02	-2.42E-03	0.67183
1.64E-02	-1.9472	3.68E-02	-3.66E-03	0.673625
1.52E-02	-1.9702	3.56E-02	-4.95E-03	0.675245
1.39E-02	-1.9932	3.43E-02	-6.29E-03	0.67678
1.25E-02	-2.02E+00	3.30E-02	-7.68E-03	0.678227
1.11E-02	-2.04E+00	3.17E-02	-9.13E-03	0.679625
9.71E-03	-2.06E+00	3.02E-02	-1.06E-02	0.680983
8.24E-03	-2.09E+00	2.88E-02	-1.21E-02	0.682333
6.74E-03	-2.11E+00	2.73E-02	-1.37E-02	0.683583
5.21E-03	-2.13E+00	2.58E-02	-1.53E-02	0.685083
3.64E-03	-2.15E+00	2.43E-02	-1.69E-02	0.686933
2.04E-03	-2.18E+00	2.28E-02	-1.86E-02	0.688683
4.11E-04	-2.20E+00	2.12E-02	-2.02E-02	0.6904
-1.24E-03	-2.22E+00	1.96E-02	-2.19E-02	0.6921
-2.92E-03	-2.25E+00	1.80E-02	-2.37E-02	0.693717
-4.61E-03	-2.27E+00	1.63E-02	-2.54E-02	0.695283
-6.33E-03	-2.29E+00	1.46E-02	-2.72E-02	0.69675
-8.06E-03	-2.32E+00	1.29E-02	-2.90E-02	0.698033
-9.81E-03	-2.34E+00	1.12E-02	-3.07E-02	0.699367
-1.16E-02	-2.36E+00	9.50E-03	-3.26E-02	0.700753
-1.33E-02	-2.39E+00	7.75E-03	-3.44E-02	0.70196
-1.51E-02	-2.41E+00	5.99E-03	-3.62E-02	0.703055
-1.69E-02	-2.43E+00	4.22E-03	-3.80E-02	0.70406
-1.87E-02	-2.45E+00	2.44E-03	-3.99E-02	0.704992
-2.05E-02	-2.48E+00	6.52E-04	-4.17E-02	0.705878
-2.23E-02	-2.50E+00	-1.14E-03	-4.35E-02	0.706713
-2.42E-02	-2.52E+00	-2.93E-03	-4.54E-02	0.70753
-0.02597	-2.5472	-4.73E-03	-0.04723	0.708262

Table A.5: Wing raw spanwise deformation dataset for mode 5

A.5. 3D Wing Effective Modal Mass Data

***** PARTICIPATION FACTOR CALCULATION ***** X DIRECTION

MODE	FREQUENCY	PERIOD	PARTIC.FACTOR	RATIO	EFFECTIVE MASS	CUMULATIVE MASS FRACTION	RATIO EFF.MASS TO TOTAL MASS
1	4.23917	0.23590	0.27076E-04	0.000045	0.733106E-09	0.203280E-08	0.124529E-08
2	21.9840	0.45488E-01	-0.33629E-03	0.000560	0.113093E-06	0.315624E-06	0.192106E-06
3	35.8397	0.27902E-01	-0.83029E-02	0.013829	0.689374E-04	0.191469E-03	0.117101E-03
4	59.5881	0.16782E-01	-0.86151E-02	0.014349	0.742194E-04	0.397270E-03	0.126073E-03
5	63.1429	0.15837E-01	-0.60041	1.000000	0.360492	0.999992	0.612351

***** PARTICIPATION FACTOR CALCULATION ***** Y DIRECTION

MODE	FREQUENCY	PERIOD	PARTIC.FACTOR	RATIO	EFFECTIVE MASS	CUMULATIVE MASS FRACTION	RATIO EFF.MASS TO TOTAL MASS
1	4.23917	0.23590	-0.58002E-03	0.086277	0.336424E-06	0.607784E-02	0.571467E-06
2	21.9840	0.45488E-01	-0.15096E-02	0.224549	0.227886E-05	0.472479E-01	0.387100E-05
3	35.8397	0.27902E-01	-0.77681E-04	0.011555	0.603431E-08	0.473569E-01	0.102502E-07
4	59.5881	0.16782E-01	-0.61311E-03	0.091199	0.375904E-06	0.541480E-01	0.638531E-06
5	63.1429	0.15837E-01	0.67228E-02	1.000000	0.451954E-04	0.870650	0.767714E-04

***** PARTICIPATION FACTOR CALCULATION ***** Z DIRECTION

MODE	FREQUENCY	PERIOD	PARTIC.FACTOR	RATIO	EFFECTIVE MASS	CUMULATIVE MASS FRACTION	RATIO EFF.MASS TO TOTAL MASS
1	4.23917	0.23590	0.60230	1.000000	0.362771	0.749706	0.616222
2	21.9840	0.45488E-01	-0.29722	0.493476	0.883415E-01	0.932274	0.150062
3	35.8397	0.27902E-01	0.63347E-02	0.010517	0.401289E-04	0.932356	0.681651E-04
4	59.5881	0.16782E-01	0.17705	0.293951	0.313460E-01	0.997136	0.532460E-01
5	63.1429	0.15837E-01	-0.25732E-02	0.004272	0.662125E-05	0.997150	0.112472E-04

***** PARTICIPATION FACTOR CALCULATION *****ROTX DIRECTION

MODE	FREQUENCY	PERIOD	PARTIC.FACTOR	RATIO	EFFECTIVE MASS	CUMULATIVE MASS FRACTION	RATIO EFF.MASS TO TOTAL MASS
1	4.23917	0.23590	0.33159	1.000000	0.109955	0.977301	0.975078
2	21.9840	0.45488E-01	-0.45974E-01	0.138646	0.211362E-02	0.996087	0.187436E-01
3	35.8397	0.27902E-01	0.28744E-02	0.008668	0.826215E-05	0.996160	0.732687E-04
4	59.5881	0.16782E-01	0.20222E-01	0.060984	0.408924E-03	0.999795	0.362633E-02
5	63.1429	0.15837E-01	-0.29297E-03	0.000884	0.858314E-07	0.999796	0.761152E-06

***** PARTICIPATION FACTOR CALCULATION *****ROTY DIRECTION

MODE	FREQUENCY	PERIOD	PARTIC.FACTOR	RATIO	EFFECTIVE MASS	CUMULATIVE MASS FRACTION	RATIO EFF.MASS TO TOTAL MASS
1	4.23917	0.23590	-0.50193E-01	1.000000	0.251933E-02	0.608582	0.487830
2	21.9840	0.45488E-01	0.22784E-01	0.453925	0.519103E-03	0.733980	0.100517
3	35.8397	0.27902E-01	-0.27868E-01	0.555223	0.776639E-03	0.921589	0.150384
4	59.5881	0.16782E-01	-0.14132E-01	0.281549	0.199707E-03	0.969831	0.386702E-01
5	63.1429	0.15837E-01	0.48918E-03	0.009746	0.239298E-06	0.969889	0.463364E-04

***** PARTICIPATION FACTOR CALCULATION *****ROTZ DIRECTION

MODE	FREQUENCY	PERIOD	PARTIC.FACTOR	RATIO	EFFECTIVE MASS	CUMULATIVE MASS FRACTION	RATIO EFF.MASS TO TOTAL MASS
1	4.23917	0.23590	-0.10783E-03	0.000324	0.116272E-07	0.104828E-06	0.986293E-07
2	21.9840	0.45488E-01	-0.65920E-04	0.000198	0.434543E-08	0.144005E-06	0.368607E-07
3	35.8397	0.27902E-01	0.46025E-02	0.013822	0.211827E-04	0.191122E-03	0.179685E-03
4	59.5881	0.16782E-01	0.46910E-02	0.014088	0.220058E-04	0.389521E-03	0.186667E-03
5	63.1429	0.15837E-01	0.33298	1.000000	0.110873	0.999990	0.940493

Figure A.1: ANSYS-obtained effective modal mass data for modes 1-5 for all six DOFs

Note:
The value reported in the ”RATIO EFF. MASS TO TOTAL MASS” column may be internally scaled or transformed depending on the participation factor normalization. In some modal configurations, this column shows relative effective mass for the specific direction, not the actual ratio to the full model mass. Specifically, the ”RATIO EFF. MASS TO TOTAL MASS” column does not always mean “divided by total model mass.” Instead, it sometimes reports the maximum modal contribution in that direction as 1.0, and scales all other modes relative to it. Therefore, the ratio $m_{\text{eff}}/m_{\text{total}}$ is manually calculated.

A.6. 1D Beam Effective Modal Mass Data

***** PARTICIPATION FACTOR CALCULATION ***** X DIRECTION

MODE	FREQUENCY	PERIOD	PARTIC.FACTOR	RATIO	EFFECTIVE MASS	CUMULATIVE MASS FRACTION	RATIO EFF.MASS TO TOTAL MASS
1	4.21544	0.23722	0.0000	0.000000	0.00000	0.00000	0.00000
2	23.6276	0.42323E-01	0.0000	0.000000	0.00000	0.00000	0.00000
3	35.6758	0.28030E-01	0.0000	0.000000	0.00000	0.00000	0.00000
4	55.7954	0.17923E-01	0.0000	0.000000	0.00000	0.00000	0.00000
5	63.5773	0.15729E-01	-0.59944	1.000000	0.359327	1.00000	0.610470

***** PARTICIPATION FACTOR CALCULATION ***** Y DIRECTION

MODE	FREQUENCY	PERIOD	PARTIC.FACTOR	RATIO	EFFECTIVE MASS	CUMULATIVE MASS FRACTION	RATIO EFF.MASS TO TOTAL MASS
1	4.21544	0.23722	0.0000	0.000000	0.00000	0.00000	0.00000
2	23.6276	0.42323E-01	0.0000	0.000000	0.00000	0.00000	0.00000
3	35.6758	0.28030E-01	0.0000	0.000000	0.00000	0.00000	0.00000
4	55.7954	0.17923E-01	0.0000	0.000000	0.00000	0.00000	0.00000
5	63.5773	0.15729E-01	0.0000	0.000000	0.00000	0.00000	0.00000

***** PARTICIPATION FACTOR CALCULATION ***** Z DIRECTION

MODE	FREQUENCY	PERIOD	PARTIC.FACTOR	RATIO	EFFECTIVE MASS	CUMULATIVE MASS FRACTION	RATIO EFF.MASS TO TOTAL MASS
1	4.21544	0.23722	0.58593	1.000000	0.343316	0.717004	0.583268
2	23.6276	0.42323E-01	-0.30261	0.516466	0.915749E-01	0.908255	0.155579
3	35.6758	0.28030E-01	0.0000	0.000000	0.00000	0.908255	0.00000
4	55.7954	0.17923E-01	0.13297	0.226943	0.176819E-01	0.945183	0.300402E-01
5	63.5773	0.15729E-01	0.0000	0.000000	0.00000	0.945183	0.00000

***** PARTICIPATION FACTOR CALCULATION *****ROTX DIRECTION

MODE	FREQUENCY	PERIOD	PARTIC.FACTOR	RATIO	EFFECTIVE MASS	CUMULATIVE MASS FRACTION	RATIO EFF.MASS TO TOTAL MASS
1	4.21544	0.23722	0.33626	1.000000	0.113071	0.965482	0.960786
2	23.6276	0.42323E-01	-0.57182E-01	0.170053	0.326978E-02	0.993401	0.277839E-01
3	35.6758	0.28030E-01	0.0000	0.000000	0.00000	0.993401	0.00000
4	55.7954	0.17923E-01	0.19139E-01	0.056917	0.366294E-03	0.996529	0.311246E-02
5	63.5773	0.15729E-01	0.0000	0.000000	0.00000	0.996529	0.00000

***** PARTICIPATION FACTOR CALCULATION *****ROTY DIRECTION

MODE	FREQUENCY	PERIOD	PARTIC.FACTOR	RATIO	EFFECTIVE MASS	CUMULATIVE MASS FRACTION	RATIO EFF.MASS TO TOTAL MASS
1	4.21544	0.23722	0.0000	0.000000	0.00000	0.00000	0.00000
2	23.6276	0.42323E-01	0.0000	0.000000	0.00000	0.00000	0.00000
3	35.6758	0.28030E-01	0.22937E-01	1.000000	0.526118E-03	1.00000	0.606479
4	55.7954	0.17923E-01	0.0000	0.000000	0.00000	1.00000	0.00000
5	63.5773	0.15729E-01	0.0000	0.000000	0.00000	1.00000	0.00000

***** PARTICIPATION FACTOR CALCULATION *****ROTZ DIRECTION

MODE	FREQUENCY	PERIOD	PARTIC.FACTOR	RATIO	EFFECTIVE MASS	CUMULATIVE MASS FRACTION	RATIO EFF.MASS TO TOTAL MASS
1	4.21544	0.23722	0.0000	0.000000	0.00000	0.00000	0.00000
2	23.6276	0.42323E-01	0.0000	0.000000	0.00000	0.00000	0.00000
3	35.6758	0.28030E-01	0.0000	0.000000	0.00000	0.00000	0.00000
4	55.7954	0.17923E-01	0.0000	0.000000	0.00000	0.00000	0.00000
5	63.5773	0.15729E-01	0.33418	1.000000	0.111677	1.00000	0.971635

Figure A.2: ANSYS-obtained effective modal mass data of 1D beam for modes 1-5 for all six DOFs

Note:
The value reported in the ”RATIO EFF. MASS TO TOTAL MASS” column may be internally scaled or transformed depending on the participation factor normalization. In some modal configurations, this column shows relative effective mass for the specific direction, not the actual ratio to the full model mass. Specifically, the ”RATIO EFF. MASS TO TOTAL MASS” column does not always mean “divided by total model mass.” Instead, it sometimes reports the maximum modal contribution in that direction as 1.0, and scales all other modes relative to it. Therefore, the ratio $m_{\text{eff}}/m_{\text{total}}$ is manually calculated.

A.7. 1D Beam Spanwise Modal Deformation Data

This section contains the numerical data of the spanwise deformation fields extracted from the 1D modal analysis. Tabulated data is available at 5 mm resolution from root to tip. The values include:

- Vertical displacement $u_z(y)$ from the `BeamNodes`
- Horizontal displacement $u_x(y)$ from the `BeamNodes`
- Angular displacements $\theta(y)$ from `BeamNodes`

Mode 1		
u_z	u_x	θ_y
0	0	0
1.762E-04	8.233E-18	2.214E-15
7.027E-04	1.851E-17	4.449E-15
1.576E-03	3.194E-17	6.671E-15
2.794E-03	4.824E-17	8.875E-15
4.352E-03	6.335E-17	1.104E-14
6.248E-03	7.525E-17	1.088E-14
8.479E-03	8.534E-17	1.067E-14
1.104E-02	9.332E-17	1.043E-14
1.393E-02	1.011E-16	1.018E-14
1.715E-02	1.091E-16	9.942E-15
2.068E-02	1.183E-16	9.136E-15
2.450E-02	1.280E-16	8.203E-15
2.863E-02	1.358E-16	7.225E-15
3.304E-02	1.411E-16	6.320E-15
3.775E-02	1.427E-16	5.571E-15
4.275E-02	1.399E-16	4.923E-15
4.803E-02	1.343E-16	4.304E-15
5.359E-02	1.249E-16	3.645E-15
5.943E-02	1.139E-16	2.935E-15
6.554E-02	1.020E-16	2.137E-15
7.193E-02	9.166E-17	1.457E-15
7.859E-02	8.284E-17	9.040E-16
8.552E-02	7.337E-17	2.541E-16
9.271E-02	6.328E-17	-2.307E-16
1.002E-01	5.355E-17	-5.280E-16
1.079E-01	4.551E-17	-7.722E-16
1.158E-01	4.043E-17	-9.726E-16
1.241E-01	3.839E-17	-1.051E-15
1.325E-01	3.750E-17	-9.414E-16
1.412E-01	3.788E-17	-7.917E-16
1.502E-01	4.095E-17	-6.569E-16
1.594E-01	4.469E-17	-4.423E-16
1.688E-01	4.975E-17	-1.167E-16
1.785E-01	5.813E-17	3.160E-16
1.884E-01	6.898E-17	8.169E-16
1.985E-01	8.311E-17	1.297E-15
2.089E-01	1.019E-16	1.668E-15
2.195E-01	1.217E-16	1.967E-15
2.303E-01	1.425E-16	2.338E-15
2.413E-01	1.644E-16	2.686E-15
2.526E-01	1.892E-16	2.943E-15
2.640E-01	2.176E-16	3.216E-15
2.757E-01	2.480E-16	3.269E-15

2.875E-01	2.806E-16	3.290E-15
2.996E-01	3.126E-16	3.290E-15
3.119E-01	3.412E-16	3.264E-15
3.243E-01	3.668E-16	3.162E-15
3.370E-01	3.861E-16	3.091E-15
3.498E-01	3.988E-16	2.980E-15
3.629E-01	4.115E-16	2.993E-15
3.761E-01	4.221E-16	2.937E-15
3.895E-01	4.289E-16	2.995E-15
4.031E-01	4.331E-16	3.123E-15
4.169E-01	4.389E-16	3.165E-15
4.308E-01	4.401E-16	3.221E-15
4.450E-01	4.395E-16	3.262E-15
4.592E-01	4.372E-16	3.488E-15
4.737E-01	4.317E-16	3.783E-15
4.883E-01	4.216E-16	4.019E-15
5.031E-01	4.084E-16	4.249E-15
5.180E-01	3.941E-16	4.533E-15
5.331E-01	3.775E-16	4.875E-15
5.484E-01	3.620E-16	5.435E-15
5.638E-01	3.443E-16	5.984E-15
5.793E-01	3.289E-16	6.433E-15
5.950E-01	3.139E-16	6.943E-15
6.108E-01	2.978E-16	7.366E-15
6.268E-01	2.808E-16	7.699E-15
6.429E-01	2.644E-16	8.115E-15
6.592E-01	2.454E-16	8.570E-15
6.755E-01	2.287E-16	8.950E-15
6.920E-01	2.148E-16	9.432E-15
7.087E-01	2.051E-16	1.000E-14
7.256E-01	1.994E-16	1.133E-14
7.429E-01	1.955E-16	1.278E-14
7.607E-01	1.950E-16	1.440E-14
7.788E-01	1.954E-16	1.610E-14
7.974E-01	1.906E-16	1.762E-14
8.164E-01	1.860E-16	1.926E-14
8.357E-01	1.808E-16	2.073E-14
8.554E-01	1.751E-16	2.206E-14
8.755E-01	1.682E-16	2.324E-14
8.960E-01	1.637E-16	2.462E-14
9.168E-01	1.563E-16	2.603E-14
9.379E-01	1.520E-16	2.736E-14
9.594E-01	1.457E-16	2.849E-14
9.812E-01	1.382E-16	2.931E-14
1.003E+00	1.312E-16	2.979E-14
1.026E+00	1.214E-16	3.002E-14
1.048E+00	1.144E-16	3.028E-14
1.071E+00	1.052E-16	3.031E-14
1.095E+00	9.878E-17	3.005E-14
1.118E+00	8.817E-17	2.945E-14
1.142E+00	7.690E-17	2.846E-14
1.166E+00	6.370E-17	2.719E-14
1.190E+00	4.954E-17	2.532E-14
1.215E+00	3.426E-17	2.350E-14
1.240E+00	1.595E-17	2.175E-14

1.265E+00	-3.695E-18	1.983E-14
1.290E+00	-2.172E-17	1.778E-14
1.315E+00	-3.692E-17	1.588E-14
1.341E+00	-5.534E-17	1.371E-14
1.367E+00	-7.114E-17	1.146E-14
1.393E+00	-8.724E-17	8.872E-15
1.419E+00	-1.049E-16	6.152E-15
1.446E+00	-1.180E-16	3.583E-15
1.472E+00	-1.261E-16	1.180E-15
1.499E+00	-1.311E-16	-1.167E-15
1.526E+00	-1.300E-16	-3.564E-15
1.553E+00	-1.260E-16	-4.807E-15
1.580E+00	-1.192E-16	-5.776E-15
1.607E+00	-1.106E-16	-6.295E-15
1.635E+00	-9.999E-17	-6.514E-15
1.662E+00	-9.049E-17	-6.489E-15
1.690E+00	-7.364E-17	-6.628E-15
1.718E+00	-5.418E-17	-6.815E-15
1.746E+00	-3.257E-17	-7.116E-15
1.774E+00	-5.749E-18	-7.521E-15
1.802E+00	2.057E-17	-7.780E-15
1.830E+00	4.530E-17	-7.883E-15
1.858E+00	7.150E-17	-7.881E-15
1.886E+00	9.990E-17	-7.993E-15
1.915E+00	1.241E-16	-8.033E-15
1.943E+00	1.516E-16	-8.244E-15
1.972E+00	1.806E-16	-8.544E-15
2.000E+00	2.102E-16	-8.686E-15
2.029E+00	2.406E-16	-8.714E-15
2.058E+00	2.721E-16	-8.952E-15
2.087E+00	3.060E-16	-9.058E-15
2.115E+00	3.358E-16	-8.812E-15
2.144E+00	3.629E-16	-8.414E-15
2.173E+00	3.840E-16	-7.862E-15
2.202E+00	4.049E-16	-7.212E-15
2.231E+00	4.203E-16	-6.805E-15
2.260E+00	4.350E-16	-6.471E-15
2.289E+00	4.479E-16	-6.203E-15
2.318E+00	4.612E-16	-5.860E-15
2.347E+00	4.764E-16	-5.446E-15
2.376E+00	4.877E-16	-5.196E-15
2.405E+00	5.034E-16	-4.683E-15
2.434E+00	5.152E-16	-3.956E-15
2.463E+00	5.238E-16	-3.323E-15
2.492E+00	5.365E-16	-2.475E-15
2.521E+00	5.465E-16	-1.642E-15
2.550E+00	5.564E-16	-7.010E-16
2.580E+00	5.700E-16	-3.200E-16
2.609E+00	5.784E-16	8.870E-17
2.638E+00	5.902E-16	6.988E-17
2.667E+00	6.006E-16	6.255E-17
2.696E+00	6.110E-16	8.490E-17

Table A.6: Beam raw spanwise modal deformation dataset for mode 1

Mode 2		
u_z	u_x	θ_y
0	0	0
-7.95E-04	-1.34E-19	2.60E-17
-3.15E-03	-8.66E-19	5.17E-17
-7.03E-03	-2.17E-18	9.48E-17
-1.24E-02	-4.08E-18	1.40E-16
-1.92E-02	-6.22E-18	1.86E-16
-2.74E-02	-8.32E-18	7.15E-17
-3.70E-02	-1.05E-17	-4.49E-17
-4.80E-02	-1.30E-17	-1.53E-16
-6.02E-02	-1.58E-17	-2.69E-16
-7.37E-02	-1.90E-17	-3.70E-16
-8.83E-02	-2.27E-17	-6.97E-16
-1.04E-01	-2.73E-17	-9.78E-16
-1.21E-01	-3.19E-17	-1.26E-15
-1.39E-01	-3.61E-17	-1.53E-15
-1.58E-01	-3.94E-17	-1.91E-15
-1.78E-01	-4.24E-17	-2.15E-15
-1.98E-01	-4.55E-17	-2.42E-15
-2.20E-01	-4.81E-17	-2.73E-15
-2.43E-01	-5.04E-17	-2.93E-15
-2.66E-01	-5.11E-17	-3.21E-15
-2.90E-01	-5.09E-17	-3.45E-15
-3.15E-01	-5.17E-17	-3.86E-15
-3.41E-01	-5.05E-17	-4.13E-15
-3.67E-01	-5.00E-17	-4.33E-15
-3.94E-01	-4.76E-17	-4.63E-15
-4.22E-01	-4.47E-17	-4.78E-15
-4.50E-01	-4.12E-17	-5.24E-15
-4.79E-01	-3.63E-17	-5.53E-15
-5.08E-01	-3.14E-17	-5.91E-15
-5.38E-01	-2.56E-17	-6.28E-15
-5.68E-01	-1.91E-17	-6.59E-15
-5.99E-01	-1.34E-17	-6.84E-15
-6.30E-01	-5.76E-18	-7.27E-15
-6.61E-01	1.43E-18	-7.50E-15
-6.93E-01	9.21E-18	-7.64E-15
-7.24E-01	1.63E-17	-8.08E-15
-7.57E-01	2.32E-17	-8.42E-15
-7.89E-01	3.23E-17	-8.75E-15
-8.22E-01	3.89E-17	-9.04E-15
-8.54E-01	4.78E-17	-9.51E-15
-8.87E-01	5.74E-17	-9.85E-15
-9.20E-01	6.69E-17	-1.03E-14
-9.53E-01	7.51E-17	-1.08E-14
-9.87E-01	8.43E-17	-1.15E-14
-1.02E+00	9.68E-17	-1.23E-14
-1.05E+00	1.05E-16	-1.28E-14
-1.09E+00	1.21E-16	-1.35E-14
-1.12E+00	1.34E-16	-1.43E-14
-1.15E+00	1.48E-16	-1.48E-14
-1.18E+00	1.63E-16	-1.53E-14
-1.22E+00	1.78E-16	-1.62E-14
-1.25E+00	1.96E-16	-1.67E-14

-1.28E+00	2.09E-16	-1.74E-14
-1.31E+00	2.23E-16	-1.79E-14
-1.34E+00	2.43E-16	-1.85E-14
-1.38E+00	2.58E-16	-1.90E-14
-1.41E+00	2.79E-16	-1.97E-14
-1.44E+00	2.95E-16	-2.02E-14
-1.47E+00	3.12E-16	-2.06E-14
-1.50E+00	3.33E-16	-2.12E-14
-1.53E+00	3.53E-16	-2.16E-14
-1.56E+00	3.72E-16	-2.18E-14
-1.59E+00	3.91E-16	-2.24E-14
-1.61E+00	4.09E-16	-2.28E-14
-1.64E+00	4.26E-16	-2.30E-14
-1.67E+00	4.45E-16	-2.34E-14
-1.70E+00	4.61E-16	-2.38E-14
-1.72E+00	4.75E-16	-2.41E-14
-1.75E+00	4.93E-16	-2.42E-14
-1.77E+00	5.06E-16	-2.46E-14
-1.80E+00	5.24E-16	-2.47E-14
-1.82E+00	5.33E-16	-2.47E-14
-1.84E+00	5.46E-16	-2.49E-14
-1.86E+00	5.54E-16	-2.53E-14
-1.88E+00	5.68E-16	-2.55E-14
-1.90E+00	5.75E-16	-2.60E-14
-1.92E+00	5.83E-16	-2.62E-14
-1.93E+00	5.91E-16	-2.63E-14
-1.94E+00	6.01E-16	-2.63E-14
-1.94E+00	6.09E-16	-2.64E-14
-1.95E+00	6.14E-16	-2.64E-14
-1.95E+00	6.23E-16	-2.66E-14
-1.95E+00	6.31E-16	-2.63E-14
-1.95E+00	6.45E-16	-2.62E-14
-1.94E+00	6.48E-16	-2.62E-14
-1.93E+00	6.60E-16	-2.60E-14
-1.92E+00	6.75E-16	-2.59E-14
-1.91E+00	6.85E-16	-2.54E-14
-1.89E+00	6.98E-16	-2.49E-14
-1.87E+00	7.12E-16	-2.46E-14
-1.85E+00	7.26E-16	-2.43E-14
-1.83E+00	7.36E-16	-2.37E-14
-1.80E+00	7.56E-16	-2.34E-14
-1.77E+00	7.69E-16	-2.26E-14
-1.74E+00	7.84E-16	-2.22E-14
-1.71E+00	8.04E-16	-2.16E-14
-1.67E+00	8.16E-16	-2.10E-14
-1.63E+00	8.37E-16	-2.06E-14
-1.59E+00	8.50E-16	-2.01E-14
-1.54E+00	8.80E-16	-1.95E-14
-1.49E+00	9.00E-16	-1.91E-14
-1.44E+00	9.19E-16	-1.86E-14
-1.39E+00	9.39E-16	-1.82E-14
-1.34E+00	9.53E-16	-1.76E-14
-1.28E+00	9.80E-16	-1.69E-14
-1.22E+00	9.97E-16	-1.63E-14
-1.16E+00	1.01E-15	-1.52E-14

-1.10E+00	1.04E-15	-1.46E-14
-1.03E+00	1.06E-15	-1.39E-14
-9.67E-01	1.07E-15	-1.32E-14
-8.98E-01	1.09E-15	-1.28E-14
-8.26E-01	1.10E-15	-1.21E-14
-7.53E-01	1.12E-15	-1.11E-14
-6.79E-01	1.14E-15	-1.04E-14
-6.02E-01	1.15E-15	-9.67E-15
-5.24E-01	1.17E-15	-9.20E-15
-4.44E-01	1.19E-15	-8.62E-15
-3.62E-01	1.21E-15	-8.02E-15
-2.79E-01	1.21E-15	-7.45E-15
-1.95E-01	1.23E-15	-7.23E-15
-1.09E-01	1.25E-15	-6.72E-15
-2.16E-02	1.26E-15	-6.43E-15
6.69E-02	1.28E-15	-5.96E-15
1.56E-01	1.29E-15	-5.50E-15
2.47E-01	1.30E-15	-5.32E-15
3.39E-01	1.32E-15	-5.17E-15
4.32E-01	1.33E-15	-5.03E-15
5.26E-01	1.35E-15	-4.69E-15
6.20E-01	1.35E-15	-4.97E-15
7.16E-01	1.37E-15	-4.66E-15
8.12E-01	1.38E-15	-4.61E-15
9.09E-01	1.39E-15	-4.59E-15
1.01E+00	1.39E-15	-4.82E-15
1.10E+00	1.39E-15	-4.93E-15
1.20E+00	1.41E-15	-5.09E-15
1.30E+00	1.41E-15	-5.15E-15
1.40E+00	1.43E-15	-5.91E-15
1.50E+00	1.43E-15	-6.02E-15
1.60E+00	1.45E-15	-6.66E-15
1.70E+00	1.46E-15	-6.76E-15
1.80E+00	1.46E-15	-7.50E-15
1.90E+00	1.46E-15	-8.02E-15
2.00E+00	1.47E-15	-8.27E-15
2.10E+00	1.48E-15	-8.85E-15
2.21E+00	1.49E-15	-9.15E-15
2.31E+00	1.49E-15	-9.15E-15
2.41E+00	1.50E-15	-9.24E-15
2.51E+00	1.50E-15	-9.40E-15
2.61E+00	1.50E-15	-9.61E-15
2.71E+00	1.50E-15	-9.92E-15

Table A.7: Beam raw spanwise modal deformation dataset for mode 2

Mode 3		
u_z	u_x	θ_y
0	0	0
-4.335E-15	-7.756E-16	8.631E-02
-1.159E-14	-1.928E-15	1.726E-01
-1.703E-14	-3.282E-15	2.589E-01
-1.887E-14	-4.769E-15	3.452E-01
-1.714E-14	-6.540E-15	4.315E-01

-1.150E-14	-8.624E-15	5.175E-01
-2.698E-15	-1.083E-14	6.034E-01
6.847E-15	-1.308E-14	6.893E-01
1.350E-14	-1.518E-14	7.753E-01
1.349E-14	-1.711E-14	8.612E-01
5.957E-15	-1.744E-14	1.147E+00
-4.297E-15	-1.900E-14	1.432E+00
-1.163E-14	-2.059E-14	1.718E+00
-1.296E-14	-2.202E-14	2.003E+00
-7.506E-15	-2.338E-14	2.288E+00
2.897E-15	-2.467E-14	2.574E+00
1.504E-14	-2.577E-14	2.859E+00
2.623E-14	-2.655E-14	3.145E+00
3.409E-14	-2.714E-14	3.430E+00
3.753E-14	-2.754E-14	3.715E+00
3.614E-14	-2.784E-14	4.001E+00
3.012E-14	-2.784E-14	4.286E+00
2.204E-14	-2.753E-14	4.571E+00
1.623E-14	-2.697E-14	4.857E+00
1.391E-14	-2.635E-14	5.142E+00
1.441E-14	-2.579E-14	5.427E+00
1.624E-14	-2.500E-14	5.712E+00
1.849E-14	-2.404E-14	5.998E+00
2.150E-14	-2.263E-14	6.283E+00
2.515E-14	-2.111E-14	6.568E+00
2.784E-14	-1.937E-14	6.853E+00
2.924E-14	-1.742E-14	7.138E+00
2.977E-14	-1.539E-14	7.423E+00
2.911E-14	-1.311E-14	7.708E+00
2.627E-14	-1.065E-14	7.993E+00
2.295E-14	-8.065E-15	8.278E+00
2.052E-14	-5.433E-15	8.563E+00
1.890E-14	-2.693E-15	8.848E+00
1.879E-14	-7.834E-17	9.133E+00
2.021E-14	2.732E-15	9.418E+00
2.183E-14	5.374E-15	9.703E+00
2.135E-14	7.878E-15	9.988E+00
1.921E-14	1.025E-14	1.024E+01
1.725E-14	1.260E-14	1.050E+01
1.620E-14	1.490E-14	1.076E+01
1.655E-14	1.702E-14	1.101E+01
1.892E-14	1.879E-14	1.127E+01
2.257E-14	2.012E-14	1.152E+01
2.527E-14	2.090E-14	1.178E+01
2.603E-14	2.129E-14	1.204E+01
2.476E-14	2.170E-14	1.229E+01
2.014E-14	2.187E-14	1.255E+01
1.344E-14	2.185E-14	1.280E+01
6.361E-15	2.162E-14	1.306E+01
3.949E-16	2.141E-14	1.332E+01
-2.928E-15	2.068E-14	1.357E+01
-1.768E-15	1.997E-14	1.383E+01
3.270E-15	1.886E-14	1.408E+01
1.097E-14	1.773E-14	1.434E+01
2.017E-14	1.629E-14	1.459E+01

2.850E-14	1.464E-14	1.485E+01
3.485E-14	1.302E-14	1.510E+01
3.789E-14	1.097E-14	1.536E+01
3.725E-14	8.890E-15	1.561E+01
3.272E-14	6.645E-15	1.587E+01
2.460E-14	4.390E-15	1.612E+01
1.494E-14	2.088E-15	1.638E+01
5.709E-15	-5.947E-16	1.663E+01
-2.691E-15	-3.398E-15	1.689E+01
-1.044E-14	-6.298E-15	1.714E+01
-1.694E-14	-9.179E-15	1.740E+01
-2.124E-14	-1.217E-14	1.765E+01
-2.316E-14	-1.501E-14	1.791E+01
-1.972E-14	-1.751E-14	1.845E+01
-5.732E-15	-1.940E-14	1.899E+01
1.779E-14	-2.099E-14	1.953E+01
4.269E-14	-2.231E-14	2.007E+01
5.735E-14	-2.333E-14	2.061E+01
5.414E-14	-2.468E-14	2.115E+01
3.558E-14	-2.565E-14	2.169E+01
1.515E-14	-2.607E-14	2.223E+01
3.909E-15	-2.631E-14	2.277E+01
8.182E-16	-2.604E-14	2.330E+01
2.103E-15	-2.559E-14	2.384E+01
4.519E-15	-2.501E-14	2.438E+01
6.517E-15	-2.406E-14	2.492E+01
7.353E-15	-2.318E-14	2.546E+01
9.667E-15	-2.228E-14	2.600E+01
1.232E-14	-2.117E-14	2.653E+01
1.145E-14	-2.023E-14	2.707E+01
7.539E-15	-1.915E-14	2.761E+01
1.865E-15	-1.797E-14	2.815E+01
-2.299E-15	-1.686E-14	2.868E+01
-3.255E-15	-1.572E-14	2.922E+01
-4.647E-17	-1.470E-14	2.975E+01
7.364E-15	-1.321E-14	3.029E+01
1.989E-14	-1.187E-14	3.083E+01
3.486E-14	-1.064E-14	3.136E+01
4.859E-14	-9.358E-15	3.190E+01
5.339E-14	-8.345E-15	3.243E+01
4.795E-14	-7.199E-15	3.297E+01
3.574E-14	-6.022E-15	3.350E+01
2.090E-14	-4.808E-15	3.404E+01
3.520E-15	-3.393E-15	3.457E+01
-1.761E-14	-1.887E-15	3.510E+01
-3.697E-14	-8.907E-16	3.564E+01
-4.800E-14	4.607E-16	3.617E+01
-4.880E-14	1.790E-15	3.670E+01
-4.276E-14	3.554E-15	3.723E+01
-3.342E-14	4.932E-15	3.754E+01
-2.259E-14	6.590E-15	3.785E+01
-1.484E-14	8.177E-15	3.815E+01
-8.503E-15	9.762E-15	3.846E+01
-1.837E-15	1.103E-14	3.876E+01
3.424E-15	1.233E-14	3.907E+01

4.477E-15	1.355E-14	3.937E+01
-1.153E-15	1.471E-14	3.968E+01
-1.205E-14	1.578E-14	3.998E+01
-2.272E-14	1.685E-14	4.028E+01
-2.867E-14	1.765E-14	4.059E+01
-3.078E-14	1.813E-14	4.089E+01
-3.553E-14	1.861E-14	4.119E+01
-4.473E-14	1.917E-14	4.149E+01
-5.718E-14	1.946E-14	4.180E+01
-6.631E-14	1.934E-14	4.210E+01
-6.878E-14	1.942E-14	4.240E+01
-6.847E-14	1.907E-14	4.270E+01
-7.362E-14	1.858E-14	4.300E+01
-8.478E-14	1.794E-14	4.330E+01
-9.294E-14	1.709E-14	4.360E+01
-9.054E-14	1.559E-14	4.390E+01
-7.993E-14	1.413E-14	4.420E+01
-6.749E-14	1.237E-14	4.450E+01
-6.041E-14	1.027E-14	4.479E+01
-6.053E-14	7.875E-15	4.509E+01
-6.838E-14	5.115E-15	4.539E+01
-8.467E-14	2.358E-15	4.569E+01
-1.057E-13	-7.949E-16	4.598E+01
-1.269E-13	-3.405E-15	4.628E+01
-1.435E-13	-6.383E-15	4.658E+01
-1.552E-13	-9.069E-15	4.687E+01
-1.639E-13	-1.176E-14	4.717E+01
-1.703E-13	-1.431E-14	4.746E+01
-1.730E-13	-1.684E-14	4.775E+01
-1.739E-13	-1.975E-14	4.805E+01
-1.809E-13	-2.211E-14	4.818E+01
-1.609E-13	-2.480E-14	4.811E+01
-1.588E-13	-2.698E-14	4.818E+01
-1.652E-13	-2.906E-14	4.818E+01
-1.686E-13	-3.119E-14	4.818E+01

Table A.8: Beam raw spanwise modal deformation dataset for mode 3

Mode 4		
u_z	u_x	θ_y
0	0	0
2.395E-03	1.234E-14	6.572E-13
9.426E-03	2.884E-14	1.345E-12
2.088E-02	5.415E-14	1.916E-12
3.654E-02	8.618E-14	2.374E-12
5.619E-02	1.103E-13	2.538E-12
7.963E-02	1.177E-13	8.778E-14
1.066E-01	1.179E-13	-2.652E-12
1.370E-01	1.107E-13	-5.493E-12
1.705E-01	1.074E-13	-8.400E-12
2.069E-01	1.090E-13	-1.127E-11
2.460E-01	1.170E-13	-2.081E-11
2.874E-01	1.300E-13	-3.076E-11
3.310E-01	1.398E-13	-4.057E-11

3.765E-01	1.380E-13	-4.935E-11
4.239E-01	1.247E-13	-5.694E-11
4.728E-01	1.068E-13	-6.383E-11
5.231E-01	8.828E-14	-7.011E-11
5.746E-01	5.783E-14	-7.566E-11
6.271E-01	2.282E-14	-8.080E-11
6.804E-01	-1.695E-14	-8.581E-11
7.344E-01	-5.138E-14	-8.978E-11
7.889E-01	-7.727E-14	-9.240E-11
8.436E-01	-9.703E-14	-9.463E-11
8.985E-01	-1.255E-13	-9.553E-11
9.533E-01	-1.621E-13	-9.529E-11
1.008E+00	-1.947E-13	-9.446E-11
1.062E+00	-2.160E-13	-9.259E-11
1.116E+00	-2.223E-13	-8.970E-11
1.169E+00	-2.270E-13	-8.538E-11
1.221E+00	-2.203E-13	-8.024E-11
1.272E+00	-2.019E-13	-7.480E-11
1.322E+00	-1.815E-13	-6.876E-11
1.370E+00	-1.482E-13	-6.239E-11
1.417E+00	-1.018E-13	-5.523E-11
1.463E+00	-4.811E-14	-4.762E-11
1.507E+00	1.525E-14	-4.008E-11
1.549E+00	9.335E-14	-3.303E-11
1.589E+00	1.767E-13	-2.612E-11
1.627E+00	2.685E-13	-1.867E-11
1.663E+00	3.591E-13	-1.138E-11
1.696E+00	4.486E-13	-4.048E-12
1.728E+00	5.458E-13	3.055E-12
1.756E+00	6.480E-13	-1.284E-12
1.783E+00	7.504E-13	-6.107E-12
1.806E+00	8.445E-13	-1.124E-11
1.827E+00	9.226E-13	-1.652E-11
1.846E+00	9.777E-13	-2.196E-11
1.861E+00	1.002E-12	-2.752E-11
1.874E+00	1.002E-12	-3.309E-11
1.883E+00	1.005E-12	-3.832E-11
1.890E+00	1.001E-12	-4.385E-11
1.894E+00	9.853E-13	-4.925E-11
1.895E+00	9.638E-13	-5.423E-11
1.893E+00	9.489E-13	-5.940E-11
1.888E+00	9.178E-13	-6.468E-11
1.879E+00	8.758E-13	-6.985E-11
1.868E+00	8.246E-13	-7.385E-11
1.854E+00	7.614E-13	-7.744E-11
1.837E+00	6.811E-13	-8.083E-11
1.817E+00	5.960E-13	-8.366E-11
1.793E+00	5.088E-13	-8.617E-11
1.767E+00	4.133E-13	-8.833E-11
1.738E+00	3.135E-13	-8.963E-11
1.707E+00	2.102E-13	-9.041E-11
1.672E+00	1.128E-13	-9.134E-11
1.635E+00	1.405E-14	-9.162E-11
1.595E+00	-9.657E-14	-9.167E-11
1.552E+00	-2.166E-13	-9.158E-11

1.507E+00	-3.329E-13	-9.118E-11
1.460E+00	-4.535E-13	-9.054E-11
1.410E+00	-5.703E-13	-8.963E-11
1.358E+00	-6.764E-13	-8.806E-11
1.304E+00	-7.609E-13	-8.577E-11
1.245E+00	-8.566E-13	-8.011E-11
1.179E+00	-8.149E-13	-7.306E-11
1.107E+00	-8.545E-13	-6.410E-11
1.028E+00	-8.780E-13	-5.469E-11
9.441E-01	-8.938E-13	-4.573E-11
8.547E-01	-9.210E-13	-3.643E-11
7.604E-01	-9.467E-13	-2.764E-11
6.619E-01	-9.561E-13	-1.841E-11
5.595E-01	-9.519E-13	-8.554E-12
4.537E-01	-9.305E-13	3.018E-12
3.451E-01	-9.001E-13	1.437E-11
2.341E-01	-8.687E-13	2.614E-11
1.214E-01	-8.242E-13	3.731E-11
7.257E-03	-7.860E-13	4.726E-11
-1.076E-01	-7.463E-13	5.637E-11
-2.228E-01	-7.072E-13	6.492E-11
-3.377E-01	-6.787E-13	7.352E-11
-4.519E-01	-6.426E-13	8.102E-11
-5.647E-01	-6.063E-13	8.728E-11
-6.759E-01	-5.663E-13	9.149E-11
-7.847E-01	-5.274E-13	9.331E-11
-8.908E-01	-4.882E-13	9.362E-11
-9.937E-01	-4.385E-13	9.164E-11
-1.093E+00	-3.854E-13	8.976E-11
-1.188E+00	-3.392E-13	8.716E-11
-1.279E+00	-2.988E-13	8.321E-11
-1.364E+00	-2.657E-13	7.841E-11
-1.444E+00	-2.352E-13	7.394E-11
-1.519E+00	-1.990E-13	6.770E-11
-1.587E+00	-1.579E-13	5.997E-11
-1.650E+00	-1.156E-13	4.986E-11
-1.705E+00	-8.154E-14	3.886E-11
-1.753E+00	-5.537E-14	2.848E-11
-1.795E+00	-2.601E-14	1.817E-11
-1.829E+00	1.529E-14	8.189E-12
-1.855E+00	6.777E-14	-2.740E-12
-1.873E+00	1.305E-13	5.578E-12
-1.884E+00	2.069E-13	1.377E-11
-1.886E+00	2.773E-13	2.285E-11
-1.881E+00	3.457E-13	3.241E-11
-1.867E+00	4.048E-13	4.211E-11
-1.845E+00	4.648E-13	5.098E-11
-1.815E+00	5.178E-13	5.919E-11
-1.776E+00	5.765E-13	6.654E-11
-1.730E+00	6.410E-13	7.236E-11
-1.676E+00	7.035E-13	7.809E-11
-1.613E+00	7.525E-13	8.350E-11
-1.543E+00	7.925E-13	8.759E-11
-1.466E+00	8.224E-13	9.039E-11
-1.381E+00	8.545E-13	9.276E-11

-1.289E+00	8.641E-13	9.452E-11
-1.189E+00	8.642E-13	9.510E-11
-1.084E+00	8.631E-13	9.541E-11
-9.713E-01	8.578E-13	9.506E-11
-8.528E-01	8.474E-13	9.288E-11
-7.285E-01	8.320E-13	8.993E-11
-5.987E-01	8.059E-13	8.787E-11
-4.636E-01	7.559E-13	8.527E-11
-3.236E-01	6.888E-13	8.231E-11
-1.791E-01	6.043E-13	7.968E-11
-3.038E-02	5.052E-13	7.579E-11
1.222E-01	3.904E-13	7.025E-11
2.783E-01	2.587E-13	6.394E-11
4.376E-01	1.268E-13	5.725E-11
5.996E-01	-4.443E-15	5.041E-11
7.642E-01	-1.292E-13	4.245E-11
9.309E-01	-2.451E-13	3.436E-11
1.100E+00	-3.562E-13	2.740E-11
1.270E+00	-4.651E-13	1.979E-11
1.441E+00	-5.695E-13	1.290E-11
1.614E+00	-6.670E-13	6.472E-12
1.787E+00	-7.670E-13	1.114E-12
1.960E+00	-8.563E-13	-4.001E-13
2.135E+00	-9.406E-13	3.983E-13
2.309E+00	-1.029E-12	9.933E-14
2.483E+00	-1.105E-12	-2.932E-13
2.658E+00	-1.171E-12	-3.936E-13

Table A.9: Beam raw spanwise modal deformation dataset for mode 4

Mode 5		
u_z	u_x	θ_y
0	0	0
1.624E-13	-1.903E-04	-1.062E-12
2.669E-13	-7.239E-04	-2.404E-12
9.160E-14	-1.597E-03	-3.381E-12
-4.002E-13	-2.808E-03	-4.096E-12
-8.908E-13	-4.352E-03	-4.381E-12
-1.212E-12	-6.228E-03	1.589E-12
-1.481E-12	-8.430E-03	8.182E-12
-1.786E-12	-1.096E-02	1.511E-11
-1.800E-12	-1.381E-02	2.210E-11
-8.446E-13	-1.697E-02	2.902E-11
4.859E-12	-2.051E-02	5.184E-11
4.027E-12	-2.440E-02	7.574E-11
5.996E-12	-2.866E-02	9.996E-11
6.695E-12	-3.327E-02	1.210E-10
5.968E-12	-3.823E-02	1.391E-10
4.014E-12	-4.354E-02	1.557E-10
1.399E-12	-4.920E-02	1.699E-10
-1.245E-12	-5.519E-02	1.819E-10
-3.528E-12	-6.153E-02	1.926E-10
-5.176E-12	-6.820E-02	2.033E-10
-5.854E-12	-7.520E-02	2.115E-10

-5.282E-12	-8.253E-02	2.166E-10
-3.825E-12	-9.018E-02	2.210E-10
-2.257E-12	-9.815E-02	2.225E-10
-9.728E-13	-1.064E-01	2.208E-10
1.666E-13	-1.150E-01	2.182E-10
1.300E-12	-1.240E-01	2.131E-10
2.329E-12	-1.332E-01	2.053E-10
2.895E-12	-1.427E-01	1.937E-10
2.658E-12	-1.525E-01	1.807E-10
1.890E-12	-1.626E-01	1.672E-10
9.240E-13	-1.730E-01	1.524E-10
-1.417E-13	-1.837E-01	1.369E-10
-1.002E-12	-1.947E-01	1.201E-10
-1.242E-12	-2.059E-01	1.021E-10
-1.022E-12	-2.175E-01	8.484E-11
-6.911E-13	-2.293E-01	6.920E-11
-1.853E-13	-2.413E-01	5.394E-11
2.271E-13	-2.537E-01	3.752E-11
3.365E-13	-2.663E-01	2.234E-11
2.681E-13	-2.791E-01	7.370E-12
4.202E-13	-2.922E-01	-7.312E-12
7.573E-13	-3.056E-01	1.255E-12
9.362E-13	-3.192E-01	1.109E-11
8.603E-13	-3.331E-01	2.189E-11
5.808E-13	-3.472E-01	3.294E-11
-2.778E-14	-3.615E-01	4.371E-11
-8.034E-13	-3.761E-01	5.544E-11
-1.394E-12	-3.909E-01	6.738E-11
-1.746E-12	-4.059E-01	7.787E-11
-1.944E-12	-4.212E-01	8.988E-11
-1.808E-12	-4.367E-01	1.016E-10
-1.443E-12	-4.524E-01	1.132E-10
-9.332E-13	-4.683E-01	1.258E-10
-2.586E-13	-4.844E-01	1.381E-10
6.357E-13	-5.007E-01	1.511E-10
1.426E-12	-5.172E-01	1.615E-10
1.943E-12	-5.340E-01	1.698E-10
1.899E-12	-5.509E-01	1.777E-10
1.159E-12	-5.680E-01	1.850E-10
1.021E-13	-5.853E-01	1.908E-10
-1.082E-12	-6.028E-01	1.948E-10
-2.244E-12	-6.205E-01	1.970E-10
-3.120E-12	-6.383E-01	1.980E-10
-3.322E-12	-6.564E-01	2.001E-10
-2.605E-12	-6.746E-01	2.008E-10
-1.280E-12	-6.929E-01	2.009E-10
2.130E-13	-7.115E-01	2.014E-10
1.603E-12	-7.302E-01	2.028E-10
2.834E-12	-7.490E-01	2.037E-10
3.840E-12	-7.681E-01	2.040E-10
4.500E-12	-7.872E-01	2.025E-10
4.860E-12	-8.066E-01	1.988E-10
3.229E-12	-8.260E-01	1.887E-10
4.106E-12	-8.457E-01	1.744E-10
1.196E-12	-8.654E-01	1.560E-10

-3.016E-12	-8.853E-01	1.367E-10
-6.479E-12	-9.054E-01	1.171E-10
-7.495E-12	-9.256E-01	9.680E-11
-5.434E-12	-9.459E-01	7.636E-11
-1.135E-12	-9.664E-01	5.489E-11
3.032E-12	-9.870E-01	3.131E-11
4.953E-12	-1.008E+00	4.418E-12
4.478E-12	-1.029E+00	-2.032E-11
2.301E-12	-1.050E+00	-4.485E-11
-4.520E-13	-1.071E+00	-6.974E-11
-2.778E-12	-1.092E+00	-9.199E-11
-3.812E-12	-1.113E+00	-1.110E-10
-3.298E-12	-1.135E+00	-1.276E-10
-1.678E-12	-1.156E+00	-1.447E-10
3.368E-13	-1.178E+00	-1.602E-10
1.845E-12	-1.199E+00	-1.717E-10
2.837E-12	-1.221E+00	-1.799E-10
3.548E-12	-1.243E+00	-1.830E-10
3.913E-12	-1.265E+00	-1.825E-10
3.791E-12	-1.287E+00	-1.767E-10
2.916E-12	-1.309E+00	-1.719E-10
9.385E-13	-1.332E+00	-1.677E-10
-1.874E-12	-1.354E+00	-1.608E-10
-4.981E-12	-1.376E+00	-1.528E-10
-6.810E-12	-1.399E+00	-1.477E-10
-6.659E-12	-1.421E+00	-1.388E-10
-4.900E-12	-1.444E+00	-1.261E-10
-2.358E-12	-1.467E+00	-1.056E-10
6.057E-13	-1.489E+00	-8.300E-11
3.758E-12	-1.512E+00	-6.155E-11
5.593E-12	-1.535E+00	-4.062E-11
5.374E-12	-1.558E+00	-1.955E-11
3.746E-12	-1.581E+00	7.646E-12
2.161E-12	-1.604E+00	-2.661E-11
9.488E-13	-1.627E+00	-5.788E-11
2.226E-13	-1.650E+00	-8.890E-11
1.841E-13	-1.673E+00	-1.202E-10
-1.162E-13	-1.696E+00	-1.517E-10
-8.161E-13	-1.720E+00	-1.797E-10
-1.721E-12	-1.743E+00	-2.057E-10
-2.586E-12	-1.766E+00	-2.299E-10
-2.715E-12	-1.790E+00	-2.511E-10
-1.907E-12	-1.813E+00	-2.716E-10
-1.090E-12	-1.836E+00	-2.925E-10
-1.375E-12	-1.860E+00	-3.106E-10
-2.023E-12	-1.883E+00	-3.228E-10
-1.532E-12	-1.907E+00	-3.331E-10
-2.372E-13	-1.930E+00	-3.424E-10
1.237E-12	-1.954E+00	-3.495E-10
2.307E-12	-1.977E+00	-3.562E-10
2.263E-12	-2.001E+00	-3.603E-10
1.854E-12	-2.025E+00	-3.589E-10
2.750E-12	-2.048E+00	-3.523E-10
4.737E-12	-2.072E+00	-3.484E-10
5.667E-12	-2.096E+00	-3.405E-10

4.238E-12	-2.119E+00	-3.308E-10
9.165E-13	-2.143E+00	-3.209E-10
-3.177E-12	-2.167E+00	-3.066E-10
-6.308E-12	-2.190E+00	-2.854E-10
-7.714E-12	-2.214E+00	-2.620E-10
-7.046E-12	-2.238E+00	-2.375E-10
-4.999E-12	-2.261E+00	-2.105E-10
-2.584E-12	-2.285E+00	-1.781E-10
-2.009E-13	-2.309E+00	-1.450E-10
1.797E-12	-2.332E+00	-1.158E-10
3.425E-12	-2.356E+00	-8.568E-11
4.537E-12	-2.380E+00	-5.609E-11
5.236E-12	-2.404E+00	-2.609E-11
5.046E-12	-2.427E+00	-1.581E-12
3.228E-12	-2.451E+00	6.044E-12
5.487E-13	-2.475E+00	2.326E-12
-1.213E-12	-2.498E+00	4.913E-12
-1.860E-12	-2.522E+00	5.903E-12
-2.754E-12	-2.546E+00	6.070E-12

Table A.10: Beam raw spanwise modal deformation dataset for mode 5